



## "Microstructural characterization of the corticospinal tract in stroke patients using advanced diffusion Magnetic Resonance Imaging techniques"

Raskin, Florent

### ABSTRACT

Stroke is the leading cause of disability worldwide. Diffusion magnetic resonance imaging (dMRI) is extensively used for performing the diagnosis and prognosis of stroke. Diffusion weighted MRI models are used to accurately characterize the microstructural alterations of brain tissues after stroke. This study aims at assessing the correlation between the structural integrity evolution of white matter brain regions and motor outcome in patients. To investigate these changes, analysis were performed on a set of 15 chronic stroke patients suffering from ischemic and hemorrhagic stroke, and divided into two populations. A total of four MRI data acquisition sessions were conducted between which patient populations followed the HABIT-ILE intensive motor rehabilitation method at different times. Diffusion parameters derived from several microstructural models (DTI, NODDI, DIAMOND, MF) were obtained using the measured MRI scans. The extraction of these diffusion parameters were used for the longitudinal assessment of the microstructural changes in the corticospinal tract (CST), cerebellar peduncles (CP), cortico-ponto cerebellar (CPC) pathway and superior longitudinal fasciculus I (SLF I). The obtained results report contrasted tendencies between both populations as the first population indicated loss of density in WM fibers, loss of myelin sheath integrity and mixing results regarding axonal degeneration whereas the second population showed signs of axonal regrowth, increased fiber density as well as improved myelin sheath integrity. Both populations displayed the majority of th...

### CITE THIS VERSION

Raskin, Florent. *Microstructural characterization of the corticospinal tract in stroke patients using advanced diffusion Magnetic Resonance Imaging techniques*. Ecole polytechnique de Louvain, Université catholique de Louvain, 2022. Prom. : Macq, Benoît ; Dricot, Laurence. <http://hdl.handle.net/2078.1/thesis:37927>

Le répertoire DIAL.mem est destiné à l'archivage et à la diffusion des mémoires rédigés par les étudiants de l'UCLouvain. Toute utilisation de ce document à des fins lucratives ou commerciales est strictement interdite. L'utilisateur s'engage à respecter les droits d'auteur liés à ce document, notamment le droit à l'intégrité de l'oeuvre et le droit à la paternité. La politique complète de droit d'auteur est disponible sur la page [Copyright policy](#)

DIAL.mem is the institutional repository for the Master theses of the UCLouvain. Usage of this document for profit or commercial purposes is strictly prohibited. User agrees to respect copyright, in particular text integrity and credit to the author. Full content of copyright policy is available at [Copyright policy](#)

**École polytechnique de Louvain**

# **Microstructural characterization of the corticospinal tract in stroke patients using advanced diffusion Magnetic Resonance Imaging techniques**

Author: **Florent RASKIN**

Supervisors: **Laurence DRICOT, Benoît MACQ**

Readers: **Nicolas DELINTE, Sébastien JODOGNE**

Academic year 2021–2022

Master [120] in Biomedical Engineering



---

## ABSTRACT

Stroke is the leading cause of disability worldwide. Diffusion magnetic resonance imaging (dMRI) is extensively used for performing the diagnosis and prognosis of stroke. Diffusion weighted MRI models are used to accurately characterize the microstructural alterations of brain tissues after stroke. This study aims at assessing the correlation between the structural integrity evolution of white matter brain regions and motor outcome in patients. To investigate these changes, analysis were performed on a set of 15 chronic stroke patients suffering from ischemic and hemorrhagic stroke, and divided into two populations. A total of four MRI data acquisition sessions were conducted between which patient populations followed the HABIT-ILE intensive motor rehabilitation method at different times. Diffusion parameters derived from several microstructural models (DTI, NODDI, DIAMOND, MF) were obtained using the measured MRI scans. The extraction of these diffusion parameters were used for the longitudinal assessment of the microstructural changes in the corticospinal tract (CST), cerebellar peduncles (CP), cortico-ponto cerebellar (CPC) pathway and superior longitudinal fasciculus I (SLF I). The obtained results report contrasted tendencies between both populations as the first population indicated loss of density in WM fibers, loss of myelin sheath integrity and mixing results regarding axonal degeneration whereas the second population showed signs of axonal regrowth, increased fiber density as well as improved myelin sheath integrity. Both populations displayed the majority of their changes in brain WM regions associated with primary motor functions but also showed some variations in secondary motor pathways. These findings reflect the potential but also the limitations of the use of dMRI models in the framework of motor stroke recovery assessment.

**Keywords:** diffusion MRI (dMRI), Diffusion Tensor Imaging (DTI), corticospinal tract (CST), motor stroke, stroke recovery



## ACKNOWLEDGMENTS

I would like to thank my supervisor, Pr Benoît Macq and Pr Laurence Dricot for giving me the opportunity to work on an interesting, cutting edge and fast developing subject.

I would also like to express my gratitude to Nicolas Delinte for the time, attention and precious advice he gave me throughout this work.

Finally, I would also like to thank Quentin Dessain for its technical advice and all of the medical staff who made this work possible.



## CONTENTS

<b>Abstract</b>	i
<b>Acknowledgments</b>	ii
<b>Introduction</b>	1
<b>1 Theoretical background</b>	2
1.1 Magnetic Resonance Imaging . . . . .	2
1.1.1 Basic magnetic properties . . . . .	2
1.1.2 Macroscopic magnetization . . . . .	3
1.1.3 Radiofrequency pulse . . . . .	5
1.1.4 Relaxation types . . . . .	7
1.1.5 Free Induction Decay . . . . .	10
1.1.6 Spin-echo sequence . . . . .	10
1.1.7 Magnetic Resonance Imaging contrast . . . . .	11
1.1.8 Magnetic Resonance Imaging acquisition . . . . .	12
1.1.9 Magnetic Resonance Imaging artifacts . . . . .	15
1.2 Diffusion Weighted Magnetic Resonance Imaging . . . . .	18
1.2.1 Pulse Gradient Spin Echo . . . . .	18
1.2.2 Diffusion Tensor Imaging . . . . .	20
1.2.3 Tractography . . . . .	24
1.3 Microstructural models . . . . .	24
1.3.1 NODDI . . . . .	25
1.3.2 DIAMOND . . . . .	28
1.3.3 Microstructure fingerprinting . . . . .	30
1.4 ElicoPy pipeline . . . . .	32
1.4.1 Preprocessing . . . . .	32
1.4.2 Motion, Eddy current and susceptibility distortion correction . .	34
1.4.3 White matter mask extraction . . . . .	34
1.4.4 Diffusion models and metrics . . . . .	35
1.4.5 Statistical analysis . . . . .	35
<b>2 Stroke Pathology</b>	36
2.1 Pathophysiology and Treatment of Stroke . . . . .	36
2.1.1 Epidemiology of Stroke . . . . .	36
2.1.2 Pathophysiology of Stroke . . . . .	37
2.1.3 Diagnosis of Stroke . . . . .	38

2.1.4	Risk Factors of Stroke . . . . .	39
2.1.5	Prevention and Treatment Strategies for Stroke . . . . .	40
2.2	Stroke induced microstructural changes . . . . .	43
2.2.1	Corticospinal Tract . . . . .	43
2.2.2	Corpus Callosum . . . . .	44
2.2.3	Cerebellar Peduncles . . . . .	45
2.2.4	Superior Longitudinal Fasciculus . . . . .	46
2.2.5	DW-MRI in Stroke studies . . . . .	46
<b>3</b>	<b>Methods</b>	<b>52</b>
3.1	Data . . . . .	52
3.1.1	Subjects . . . . .	52
3.1.2	Data acquisition . . . . .	54
3.1.3	Behavioral analysis . . . . .	55
3.2	Data preprocessing . . . . .	56
3.3	Data registration . . . . .	56
3.3.1	Atlas sets . . . . .	57
3.3.2	Registration process . . . . .	58
3.4	Microstructural analysis . . . . .	58
3.4.1	DTI metric maps . . . . .	60
3.4.2	NODDI metric maps . . . . .	61
3.4.3	DIAMOND metric maps . . . . .	61
3.4.4	MF metric maps . . . . .	62
3.5	Statistical analysis . . . . .	62
<b>4</b>	<b>Results</b>	<b>64</b>
4.1	DTI results . . . . .	64
4.1.1	Fractional Anisotropy . . . . .	64
4.1.2	Mean Diffusivity . . . . .	65
4.1.3	Axial Diffusivity . . . . .	65
4.1.4	Radial Diffusivity . . . . .	66
4.2	NODDI results . . . . .	66
4.2.1	Fiber Orientation Dispersion Index . . . . .	66
4.2.2	Extracellular Volume Fraction . . . . .	67
4.2.3	Intracellular Volume Fraction . . . . .	67
4.2.4	Free Water Volume Fraction . . . . .	68
4.3	DIAMOND results . . . . .	68
4.3.1	Weighted Fractional Anisotropy . . . . .	69
4.3.2	Weighted Mean Diffusivity . . . . .	69
4.3.3	Weighted Axial Diffusivity . . . . .	69
4.3.4	Weighted Radial Diffusivity . . . . .	70
4.4	Microstructure Fingerprinting results . . . . .	70
4.4.1	First Population Fraction . . . . .	71
4.4.2	Second Population Fraction . . . . .	71

4.4.3	Free Water Fraction . . . . .	71
4.4.4	Total Fiber Volume Fraction . . . . .	72
4.4.5	Weighted Total Fiber Volume Fraction . . . . .	72
<b>5</b>	<b>Discussion</b>	<b>74</b>
5.1	DTI analysis . . . . .	74
5.2	NODDI analysis . . . . .	75
5.3	DIAMOND analysis . . . . .	76
5.4	MF analysis . . . . .	77
5.5	Summary . . . . .	77
5.6	Limitations . . . . .	78
5.7	Future Perspectives . . . . .	81
	<b>Conclusion</b>	<b>84</b>
<b>A</b>	<b>DTI additional results</b>	<b>xiii</b>
A.1	Fractional Anisotropy . . . . .	xiii
A.2	Mean Diffusivity . . . . .	xiv
A.3	Axial Diffusivity . . . . .	xv
A.4	Radial Diffusivity . . . . .	xvi
<b>B</b>	<b>NODDI additional results</b>	<b>xvii</b>
B.1	Fiber Orientation Dispersion Index . . . . .	xvii
B.2	Extracellular Volume Fraction . . . . .	xviii
B.3	Intracellular Volume Fraction . . . . .	xix
B.4	Free Water Volume Fraction . . . . .	xx
<b>C</b>	<b>DIAMOND additional results</b>	<b>xxi</b>
C.1	Weighted Fractional Anisotropy . . . . .	xxi
C.2	Weighted Mean Diffusivity . . . . .	xxii
C.3	Weighted Axial Diffusivity . . . . .	xxiii
C.4	Weighted Radial Diffusivity . . . . .	xxiv
<b>D</b>	<b>MF additional results</b>	<b>xxv</b>
D.1	First Population Fraction . . . . .	xxv
D.2	Second Population Fraction . . . . .	xxvi
D.3	Free Water Fraction . . . . .	xxvii
D.4	Total Fiber Volume Fraction . . . . .	xxviii
D.5	Weighted Total Fiber Volume Fraction . . . . .	xxix
<b>E</b>	<b>Corpus Callosum Registration</b>	<b>xxx</b>
<b>F</b>	<b>Tract-based ROI</b>	<b>xxxi</b>
<b>G</b>	<b>Connectivity Analysis</b>	<b>xxxiii</b>

## LIST OF FIGURES

1.1	Magnetic moment of a rotating nucleus [4] . . . . .	3
1.2	Influence of the external magnetic field on net magnetization [4] . . . . .	4
1.3	Precession movement of a hydrogen nucleus [4] . . . . .	4
1.4	Precession movement in (a) the laboratory frame and in (b) the rotating frame [4] . . . . .	6
1.5	(a) resting state, (b) 90°-pulse and (c) 180°-pulse, adapted from [4] . . . . .	7
1.6	Exponential recovery of the net magnetization against $T_1$ relaxation time, adapted from [4] . . . . .	8
1.7	Spin-network relaxation for different biological media, adapted from [4]	8
1.8	Exponential recovery of the net magnetization against $T_2$ relaxation time, adapted from [4] . . . . .	9
1.9	Dephasing of the transverse magnetization and measurement of the FID, adapted from [4] . . . . .	10
1.10	Spin echo sequence, adapted from [4] . . . . .	11
1.11	$T_1$ contrast principle, adapted from [4] . . . . .	12
1.12	$T_2$ contrast principle, adapted from [4] . . . . .	12
1.13	$T_2$ contrast principle - tissues A & B have the same proton density whereas tissue C has a greater proton density resulting in different signals, adapted from [4] . . . . .	13
1.14	Bipolar slice-select gradient principle, adapted from [4] . . . . .	14
1.15	Complete chronology of RF-pulses and gradient applications for a spin-echo sequence, adapted from [4] . . . . .	15
1.16	MRI artifacts: (A) Motion artifact; (B) Chemical shift artifact; (C) Magnetic susceptibility artifact; (D) Gibbs artifact; (E) Aliasing artifact; (F) Moiré fringes; (G) Zipper artifacts, adapted from [19] . . . . .	17
1.17	Water molecular motion types, adapted from [28] . . . . .	18
1.18	PGSE sequence diagram, adapted from [28] . . . . .	19
1.19	Effects of molecular motion on phase shift with a pair of gradients. Large black arrows represent the strength of the magnetic field; small black arrows indicate phases of individual protons; proton motion in between gradient application is represented by colored boxes, adapted from [29]	19
1.20	(A) Isotropic diffusion; (B) restricted diffusion with tensor eigenvalues; (C) restricted diffusion with tensor eigenvectors, adapted from [6] . . . . .	21
1.21	Diffusion Tensor Imaging metrics maps: Mean Diffusivity (MD); Axial Diffusivity (MD); Radial Diffusivity (RD); Fractional Anisotropy (FA), Red-Green-Blue Fractional Anisotropy . . . . .	23
1.22	Whole-brain tractogram obtained from DTI metrics, adapted from [31]	24

1.23	Basic example showing the difference between deterministic and probabilistic tracking models, adapted from [35] . . . . .	25
1.24	NODDI compartments and parameters, adapted from [37] . . . . .	27
1.25	DIAMOND model: (A) Multi-compartment model with isotropic (red) and anisotropic (blue and green) compartments; (B) Multi-Tensor Model with purely homogeneous compartments; (C) DIAMOND peak-shaped distributions of multidimensional diffusivities accounting for heterogeneity in each compartment, adapted from [38] . . . . .	30
1.26	Microstructure fingerprinting model sparse dictionary matching between the acquisition $y$ and the linear combinations of signals $a_1, a_2, \dots$ stored in the dictionary, adapted from [40] . . . . .	31
1.27	Overview of the main processing steps in the ElikoPy pipeline, adapted from [41] . . . . .	33
1.28	Preprocessing steps of the ElikoPy pipeline [42] . . . . .	34
2.1	Molecular mechanisms of ischemic and hemorrhagic stroke, adapted from [53] . . . . .	38
2.2	Non-modifiable risk factors associated with stroke . . . . .	39
2.3	Modifiable risk factors associated with stroke . . . . .	40
2.4	Stroke therapy strategies, adapted from [53] . . . . .	41
2.5	Hypothetical pattern of recovery after stroke [70] . . . . .	42
2.6	Corticospinal tract [75] . . . . .	44
2.7	Motor homunculus [77] . . . . .	44
2.8	Corticospinal tract fibers isolated using tractography [77] . . . . .	44
2.9	Corpus Callosum anatomy [79] . . . . .	45
2.10	Cerebellum and Cerebellar Peduncles anatomy [81] . . . . .	45
2.11	Superior Longitudinal Fasciculus anatomy . . . . .	46
3.1	Subjects data acquisition flowchart . . . . .	53
3.2	Anatomical volume slices of subject <i>20.03.01</i> at T1 in the sagittal, frontal and axial views . . . . .	54
3.3	Raw diffusion volume slices of subject <i>20.03.01</i> at T1 for the different b-values . . . . .	54
3.4	Truncated raw diffusion volume slices of subject <i>20.03.01</i> at T0 . . . . .	55
3.5	Comparison between raw and preprocessed diffusion volume slices of subject <i>20.03.01</i> at T1 . . . . .	57
3.6	Illustration of (A) affine transformations; (B) diffeomorphic transformations, adapted from [126] . . . . .	59
3.7	Illustration of the registration corrections on the frontal lobe of patient <i>20.03.01</i> at T1 . . . . .	59
3.8	Registered corticospinal tract ROI for patient <i>20.03.01</i> at T1 . . . . .	60
3.9	Diffusion Tensor Imaging (DTI) metric maps of patient <i>20.03.01</i> at T1 . . . . .	60
3.10	NODDI metric maps of patient <i>20.03.01</i> at T1 . . . . .	61
3.11	DIAMOND metrics maps of patient <i>20.03.01</i> at T1 . . . . .	62
3.12	MF metrics maps of patient <i>20.03.01</i> at T1 . . . . .	63

4.1	Fractional Anisotropy (FA) boxplots in the Corticospinal Tract (CST) on the ipsi- and contralesional sides for both patient populations . . . . .	65
4.2	Mean Diffusivity (MD) boxplots in the Corticospinal Tract (CST) on the ipsi- and contralesional sides for both patient populations . . . . .	65
4.3	Axial Diffusivity (AD) boxplots in the Corticospinal Tract (CST) on the ipsi- and contralesional sides for both patient populations . . . . .	66
4.4	Radial Diffusivity (RD) boxplots in the Corticospinal Tract (CST) on the ipsi- and contralesional sides for both patient populations . . . . .	66
4.5	Fiber Orientation Dispersion Index (ODI) boxplots in the Corticospinal Tract (CST) on the ipsi- and contralesional sides for both patient populations . . . . .	67
4.6	Extracellular volume fraction ( $f_{\text{extra}}$ ) boxplots in the Corticospinal Tract (CST) on the ipsi- and contralesional sides for both patient populations	67
4.7	Intracellular volume fraction ( $f_{\text{intra}}$ ) boxplots in the Corticospinal Tract (CST) on the ipsi- and contralesional sides for both patient populations	68
4.8	Free water volume fraction ( $f_{\text{iso}}$ ) boxplots in the Corticospinal Tract (CST) on the ipsi- and contralesional sides for both patient populations	68
4.9	Weighted Fractional Anisotropy (wFA) boxplots in the Corticospinal Tract (CST) on the ipsi- and contralesional sides for both patient populations . . . . .	69
4.10	Weighted Mean Diffusivity (wMD) boxplots in the Corticospinal Tract (CST) on the ipsi- and contralesional sides for both patient populations	69
4.11	Weighted Axial Diffusivity (wAD) boxplots in the Corticospinal Tract (CST) on the ipsi- and contralesional sides for both patient populations	70
4.12	Weighted Radial Diffusivity (wRD) boxplots in the Corticospinal Tract (CST) on the ipsi- and contralesional sides for both patient populations	70
4.13	Fraction of occupancy of the first fascicle population (frac_f0) boxplots in the Corticospinal Tract (CST) on the ipsi- and contralesional sides for both patient populations . . . . .	71
4.14	Fraction of occupancy of the second fascicle population (frac_f1) boxplots in the Corticospinal Tract (CST) on the ipsi- and contralesional sides for both patient populations . . . . .	71
4.15	Fraction of occupancy of the CSF (frac_csf) boxplots in the Corticospinal Tract (CST) on the ipsi- and contralesional sides for both patient populations . . . . .	72
4.16	Total fiber volume fraction (fvf_tot) boxplots in the Corticospinal Tract (CST) on the ipsi- and contralesional sides for both patient populations	72
4.17	Weighted total fiber volume fraction (wfvf) boxplots in the Corticospinal Tract (CST) on the ipsi- and contralesional sides for both patient populations . . . . .	73
5.1	Imperfections of the first acquisition session illustrated for patient 20.06.01 at times T0 and T1 . . . . .	79

5.2	Purely affine registration (red) compared to affine and diffeomorphic registration (green), illustrated for patient <i>20.02.02</i> at times T0 . . . . .	80
A.1	Fractional Anisotropy (FA) boxplots in the Cortico Ponto Cerebellum (CPC), Inferior Cerebellar Pedunculus (iCP) and Superior Cerebellar Pedunculus (sCP) for both patient populations . . . . .	xiii
A.2	Fractional Anisotropy (FA) boxplots in the Middle Cerebellar Pedunculus (mCP) on the ipsi- and contralesional sides for both patient populations	xiii
A.3	Fractional Anisotropy (FA) boxplots in the Superior Longitudinal Fasciculus I (SLF I) on the ipsi- and contralesional sides for both patient populations . . . . .	xiv
A.4	Mean Diffusivity (MD) boxplots in the Cortico Ponto Cerebellum (CPC), Inferior Cerebellar Pedunculus (iCP) and Superior Cerebellar Pedunculus (sCP) on the ipsi- and contralesional sides for both patient populations	xiv
A.5	Mean Diffusivity (MD) boxplots in the Middle Cerebellar Pedunculus (mCP) for both patient populations . . . . .	xiv
A.6	Mean Diffusivity (MD) boxplots in the Superior Longitudinal Fasciculus I (SLF I) on the ipsi- and contralesional sides for both patient populations	xiv
A.7	Axial Diffusivity (AD) boxplots in the Cortico Ponto Cerebellum (CPC), Inferior Cerebellar Pedunculus (iCP) and Superior Cerebellar Pedunculus (sCP) on the ipsi- and contralesional sides for both patient populations	xv
A.8	Axial Diffusivity (AD) boxplots in the Middle Cerebellar Pedunculus (mCP) for both patient populations . . . . .	xv
A.9	Axial Diffusivity (AD) boxplots in the Superior Longitudinal Fasciculus I (SLF I) on the ipsi- and contralesional sides for both patient populations	xv
A.10	Radial Diffusivity (RD) boxplots in the Cortico Ponto Cerebellum (CPC), Inferior Cerebellar Pedunculus (iCP) and Superior Cerebellar Pedunculus (sCP) on the ipsi- and contralesional sides for both patient populations	xvi
A.11	Radial Diffusivity (RD) boxplots in the Middle Cerebellar Pedunculus (mCP) for both patient populations . . . . .	xvi
A.12	Radial Diffusivity (RD) boxplots in the Superior Longitudinal Fasciculus I (SLF I) on the ipsi- and contralesional sides for both patient populations	xvi
B.1	Fiber Orientation Dispersion Index (ODI) boxplots in the Cortico Ponto Cerebellum (CPC), Inferior Cerebellar Pedunculus (iCP) and Superior Cerebellar Pedunculus (sCP) on the ipsi- and contralesional sides for both patient populations . . . . .	xvii
B.2	Fiber Orientation Dispersion Index (ODI) boxplots in the Middle Cerebellar Pedunculus (mCP) on the ipsi- and contralesional sides for both patient populations . . . . .	xvii
B.3	Fiber Orientation Dispersion Index (ODI) boxplots in the Superior Longitudinal Fasciculus I (SLF I) on the ipsi- and contralesional sides for both patient populations . . . . .	xviii

B.4	Extracellular volume fraction ( $f_{\text{extra}}$ ) boxplots in the Cortico Ponto Cerebellum (CPC), Inferior Cerebellar Pedunculus (iCP) and Superior Cerebellar Pedunculus (sCP) on the ipsi- and contralesional sides for both patient populations . . . . .	xviii
B.5	Extracellular volume fraction ( $f_{\text{extra}}$ ) boxplots in the Middle Cerebellar Pedunculus (mCP) for both patient populations . . . . .	xviii
B.6	Extracellular volume fraction ( $f_{\text{extra}}$ ) boxplots in the Superior Longitudinal Fasciculus I (SLF I) on the ipsi- and contralesional sides for both patient populations . . . . .	xviii
B.7	Intracellular volume fraction ( $f_{\text{intra}}$ ) boxplots in the Cortico Ponto Cerebellum (CPC), Inferior Cerebellar Pedunculus (iCP) and Superior Cerebellar Pedunculus (sCP) on the ipsi- and contralesional sides for both patient populations . . . . .	xix
B.8	Intracellular volume fraction ( $f_{\text{intra}}$ ) boxplots in the Middle Cerebellar Pedunculus (mCP) for both patient populations . . . . .	xix
B.9	Intracellular volume fraction ( $f_{\text{intra}}$ ) boxplots in the Superior Longitudinal Fasciculus I (SLF I) on the ipsi- and contralesional sides for both patient populations . . . . .	xix
B.10	Free water volume fraction ( $f_{\text{iso}}$ ) boxplots in the Cortico Ponto Cerebellum (CPC), Inferior Cerebellar Pedunculus (iCP) and Superior Cerebellar Pedunculus (sCP) on the ipsi- and contralesional sides for both patient populations . . . . .	xx
B.11	Free water volume fraction ( $f_{\text{iso}}$ ) boxplots in the Middle Cerebellar Pedunculus (mCP) for both patient populations . . . . .	xx
B.12	Free Water Volume Fraction ( $f_{\text{iso}}$ ) boxplots in the Superior Longitudinal Fasciculus I (SLF I) on the ipsi- and contralesional sides for both patient populations . . . . .	xx
C.1	Weighted Fractional Anisotropy (wFA) boxplots in the Cortico Ponto Cerebellum (CPC), Inferior Cerebellar Pedunculus (iCP) and Superior Cerebellar Pedunculus (sCP) on the ipsi- and contralesional sides for both patient populations . . . . .	xxi
C.2	Weighted Fractional Anisotropy (wFA) boxplots in Middle Cerebellar Pedunculus (mCP) for both patient populations . . . . .	xxi
C.3	Weighted Fractional Anisotropy (wFA) boxplots in the Superior Longitudinal Fasciculus I (SLF I) on the ipsi- and contralesional sides for both patient populations . . . . .	xxii
C.4	Weighted Mean Diffusivity (wMD) boxplots in the Cortico Ponto Cerebellum (CPC), Inferior Cerebellar Pedunculus (iCP) and Superior Cerebellar Pedunculus (sCP) on the ipsi- and contralesional sides for both patient populations . . . . .	xxii
C.5	Weighted Mean Diffusivity (wMD) boxplots in the Middle Cerebellar Pedunculus (mCP) for both patient populations . . . . .	xxii

C.6	Weighted Mean Diffusivity (MD) boxplots in the Superior Longitudinal Fasciculus I (SLF I) on the ipsi- and contralesional sides for both patient populations . . . . .	xxii
C.7	Weighted Axial Diffusivity (wAD) boxplots in the Cortico Ponto Cerebellum (CPC), Inferior Cerebellar Pedunculus (iCP) and Superior Cerebellar Pedunculus (sCP) on the ipsi- and contralesional sides for both patient populations . . . . .	xxiii
C.8	Weighted Axial Diffusivity (wAD) boxplots in the Middle Cerebellar Pedunculus (mCP) for both patient populations . . . . .	xxiii
C.9	Weighted Axial Diffusivity (AD) boxplots in the Superior Longitudinal Fasciculus I (SLF I) on the ipsi- and contralesional sides for both patient populations . . . . .	xxiii
C.10	Weighted Radial Diffusivity (RD) boxplots in the Cortico Ponto Cerebellum (CPC), Inferior Cerebellar Pedunculus (iCP) and Superior Cerebellar Pedunculus (sCP) on the ipsi- and contralesional sides for both patient populations . . . . .	xxiv
C.11	Weighted Radial Diffusivity (RD) boxplots in the Middle Cerebellar Pedunculus (mCP) for both patient populations . . . . .	xxiv
C.12	Weighted Radial Diffusivity (RD) boxplots in the Superior Longitudinal Fasciculus I (SLF I) on the ipsi- and contralesional sides for both patient populations . . . . .	xxiv
D.1	First population fraction (frac_f0) boxplots in the Cortico Ponto Cerebellum (CPC), Inferior Cerebellar Pedunculus (iCP) and Superior Cerebellar Pedunculus (sCP) on the ipsi- and contralesional sides for both patient populations . . . . .	xxv
D.2	First population fraction (frac_f0) boxplots in the Middle Cerebellar Pedunculus (mCP) for both patient populations . . . . .	xxv
D.3	First population fraction (frac_f0) boxplots in the Superior Longitudinal Fasciculus I (SLF I) on the ipsi- and contralesional sides for both patient populations . . . . .	xxvi
D.4	Second population fraction (frac_f1) boxplots in the Cortico Ponto Cerebellum (CPC), Inferior Cerebellar Pedunculus (iCP) and Superior Cerebellar Pedunculus (sCP) on the ipsi- and contralesional sides for both patient populations . . . . .	xxvi
D.5	Second population fraction (frac_f1) boxplots in Middle Cerebellar Pedunculus (mCP) for both patient populations . . . . .	xxvi
D.6	Second population fraction (frac_f1) boxplots in the Superior Longitudinal Fasciculus I (SLF I) on the ipsi- and contralesional sides for both patient populations . . . . .	xxvi
D.7	Free water fraction (frac_csf) boxplots in the Cortico Ponto Cerebellum (CPC), Inferior Cerebellar Pedunculus (iCP) and Superior Cerebellar Pedunculus (sCP) on the ipsi- and contralesional sides for both patient populations . . . . .	xxvii

D.8	Free water fraction (frac_csf) boxplots in the Middle Cerebellar Pedunculus (mCP) for both patient populations . . . . .	xxvii
D.9	Free water fraction (frac_csf) boxplots in the Superior Longitudinal Fasciculus I (SLF I) on the ipsi- and contralesional sides for both patient populations . . . . .	xxvii
D.10	Total fiber volume fraction (fvf_tot) boxplots in the Cortico Ponto Cerebellum (CPC), Inferior Cerebellar Pedunculus (iCP) and Superior Cerebellar Pedunculus (sCP) on the ipsi- and contralesional sides for both patient populations . . . . .	xxviii
D.11	Total fiber volume fraction (fvf_tot) boxplots in the Middle Cerebellar Pedunculus (mCP) for both patient populations . . . . .	xxviii
D.12	Total fiber volume fraction (fvf_tot) boxplots in the Superior Longitudinal Fasciculus I (SLF I) on the ipsi- and contralesional sides for both patient populations . . . . .	xxviii
D.13	Weighted total fiber volume fraction (wfvf) boxplots in the Cortico Ponto Cerebellum (CPC), Inferior Cerebellar Pedunculus (iCP) and Superior Cerebellar Pedunculus (sCP) on the ipsi- and contralesional sides for both patient populations . . . . .	xxix
D.14	Weighted total fiber volume fraction (wfvf) boxplots in the Middle Cerebellar Pedunculus (mCP) for both patient populations . . . . .	xxix
D.15	Weighted total fiber volume fraction (wfvf) boxplots in the Superior Longitudinal Fasciculus I (SLF I) on the ipsi- and contralesional sides for both patient populations . . . . .	xxix
E.1	Inaccurate registration of the corpus callosum illustrated for patient 20.03.03 at time T1 . . . . .	xxx
F.1	Whole-brain tractogram of patient 20.03.03 at time T1 . . . . .	xxxi
F.2	Definition of the seed regions, target regions and exclusion masks for CST tractography, adapted from [1] . . . . .	xxxii
F.3	Illustration of the seed region in the CST and of the target region in the motor cortex . . . . .	xxxii
F.4	Resulting CST ROI for patient 20.03.03 at time T1 . . . . .	xxxii
G.1	Segmentation and parcellation obtained using the FreeSurfer software on patient 20.03.03 at time T1 . . . . .	xxxiii

---

## LIST OF TABLES

1.1	Comparison between T1-weighted, T2-weighted and proton density weighted images, adapted from [14]	13
2.1	Age-adjusted annual incidence and mortality rates, prevalence, and DALYs lost for all stroke, ischemic stroke, and hemorrhagic stroke (HIC = high-income country; LMIC = low-income and middle-income country; DALY = disability-adjusted life-year), adapted from [55]	37
2.2	Summary of the literature articles reviewed. DTI = Diffusion Tensor Imaging; TBSS = Tract-Based Spatial Statistics; TMS = Transcranial Magnetic Stimulation; DKI = Diffusion Kurtosis Imaging; CTI = Correlation Tensor Imaging; HARDI = High Angular Resolution Diffusion Imaging; NODDI = Neurite Orientation Dispersion and Density Imaging; SVM = Support Vector Machine; CST = corticospinal tract; PT = pyramidal tract; PLIC = posterior limb of the internal capsule; WM = white matter	50
3.1	Patients information	53

## INTRODUCTION

Stroke is the second cause of death worldwide and a leading cause of long-term disability, with more than 1.5 million cases reported each year in Europe. Despite years of research in this field, the understanding of the underlying neuronal mechanisms and the development of optimal rehabilitative strategies still require major improvements [1].

Diffusion Magnetic Resonance Imaging (dMRI) is used to analyze the diffusion of water molecules in tissues and is extensively employed as a tool to identify stroke lesions as well as the incurred white matter (WM) tract neurological damage. Indeed, following stroke onset, injured WM tracts lose their integrity and dMRI techniques are used to characterize and quantify the microstructural changes caused by these neurological injuries. The use of powerful mathematical models such as Diffusion Tensor Imaging (DTI) allow the measurement of the diffusion of waters molecules which, in turn provides information regarding the microstructural properties of the surrounding biological tissues. In other words, Diffusion Weighted MRI (DW-MRI) models are used to extract metrics characterizing the brain tissue microstructure which are then used as biomarkers to predict recovery after stroke [2].

As the vast majority of stroke patients are subject to motor impairment, the identification of appropriate rehabilitation methods and the study of motor outcome recovery is of the upmost importance in order to improve patients' quality of life. To this end, DW-MRI models such as DTI but also Neurite Orientation Dispersion and Density Imaging (NODDI), DIistribution of 3D Anisotropic MicrOstructural eNvironments in Diffusion-compartment imaging (DIAMOND) and Microstructure Fingerprinting (MF) are used in the present work to characterize the microstructural evolution of patients' key brain areas involved in motor functions.

More precisely, this study aims at investigating the microstructural changes occurring in key WM motor areas such as the corticospinal tract (CST) in order to infer on the efficacy of a specific rehabilitation treatment called *Hand and Arm Bimanual Intensive Therapy Including Lower Extremities* (HABIT-ILE). The theoretical concepts, needed for a complete understanding of the dMRI techniques used, are first extensively described in the first chapter of this Master's thesis. The second chapter gives an overview of already published studies in this field of research. This is then followed by the description, discussion and interpretation of the methods used and the results obtained in this study. Finally, an assessment of the limitations of this work is presented and completed with the examination of further improvement perspectives.

# CHAPTER 1

## THEORETICAL BACKGROUND

The first two chapters of this Master's thesis cover the fundamental theoretical principles and concepts required for a thorough understanding of the scientific methods used in this work. This first chapter summarizes the concepts of nuclear magnetic resonance, magnetic resonance imaging, diffusion-weighted magnetic resonance imaging and microstructural models.

### 1.1 Magnetic Resonance Imaging

Magnetic resonance imaging (MRI) is a modern microstructure imaging technique used for estimating and mapping histological features of tissue in a non-invasive, non-destructive, relatively fast and cheap manner [3]. MRI can thus be considered as a more practical technique than classical histology and as a safer imaging technique compared to computed tomography (CT) and positron emission tomography (PET) imaging which requires the use of radioactive isotopes. Magnetic resonance imaging relies on the nuclear magnetic resonance (NMR) principle which is based on the fundamental magnetic properties of nuclei.

#### 1.1.1 Basic magnetic properties

Every nucleus can be characterized by a total of four quantum numbers: the principal quantum number ( $n$ ), the orbital angular momentum quantum number ( $l$ ), the magnetic quantum number ( $m_l$ ), and the electron spin quantum number ( $m_s$ ). The electron spin quantum number ( $m_s$ ) can take specific discrete values depending on the mass number  $A$  and the atomic number  $Z$  of the atom. The three specific cases determining the electron spin quantum number value are described as follows:

- In the case of an even mass number  $A$  and an even atomic number  $Z$  (e.g.  $^{12}C$ ,  $^{16}O$ ):  $m_s = 0$
- In the case of an odd mass number  $A$  and an odd atomic number  $Z$  (e.g.  $^1H$ ,  $^{13}C$ ,  $^{15}N$ ):  $m_s = \frac{1}{2}$
- In the case of an even mass number  $A$  and an odd atomic number  $Z$  (e.g.  $^2H$ ,  $^{10}B$ ,  $^{14}N$ ):  $m_s = 1$

Since nuclei are charged particles composed of protons and neutrons, a nucleus with a spin is thus a charged particle rotating around its axis. The rotation of the nucleus

induces an electric current and a magnetic field, characterized by a magnetic moment  $\vec{\mu}$  aligned with the rotation axis of the nucleus denoted  $\vec{S}$  (see Figure 1.1). Rotating nuclei can therefore be assimilated to small magnets.

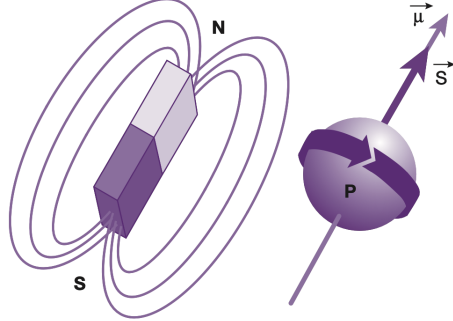


Figure 1.1: Magnetic moment of a rotating nucleus [4]

Magnetic resonance imaging mainly focuses on imaging using the magnetic properties of hydrogen ( $^1H$ ) atoms, which are abundant in the human body (approximately 2/3 of the atoms of the human organism), in order to provide anatomical images. Indeed, the hydrogen nucleus, formed by a single proton, has a large intrinsic magnetic momentum allowing a sharp resonance phenomenon [5].

### 1.1.2 Macroscopic magnetization

Without the application of an external magnetic field, the orientations of the magnetic moments of the nuclei are randomly distributed due to the random Brownian motion of particles in biological tissues. The sum of all the magnetic moments resulting from each spin ( $\sum \vec{\mu}$ ), called net magnetization or macroscopic magnetization vector ( $\vec{M}$ ) is thus null in a large biological medium ( $\vec{M} = \sum \vec{\mu} = \vec{0}$ ). However, when an external magnetic field ( $B_0$ ) is applied on a biological tissue, the orientations of the magnetic moments of particles with a non-zero electron spin quantum number are discretized according to  $2m_s + 1$  possible orientations. The orientations of the magnetic moments of the hydrogen nuclei ( $2m_s + 1 = 2 * \frac{1}{2} + 1 = 2$ ) present in the human body will thus align with the external magnetic field ( $B_0$ ) and take two possible orientations: either a parallel or anti-parallel orientation. The parallel and anti-parallel orientations are often referred to as *spin-up* and *spin-down* orientations and are illustrated on Figure 1.2. The discretization of the orientations of the magnetic moments results in non-zero net magnetization ( $\vec{M} = \sum \vec{\mu} \neq \vec{0}$ ).

The application of the external magnetic field ( $B_0$ ) induces a torque,  $\vec{\tau}$ , onto the magnetic moment of the spinning particle:

$$\vec{\tau} = \vec{\mu} \times \vec{B}_0. \quad (1.1)$$

This torque ( $\vec{\tau}$ ) in turn induces a precession movement around the axis of the spinning

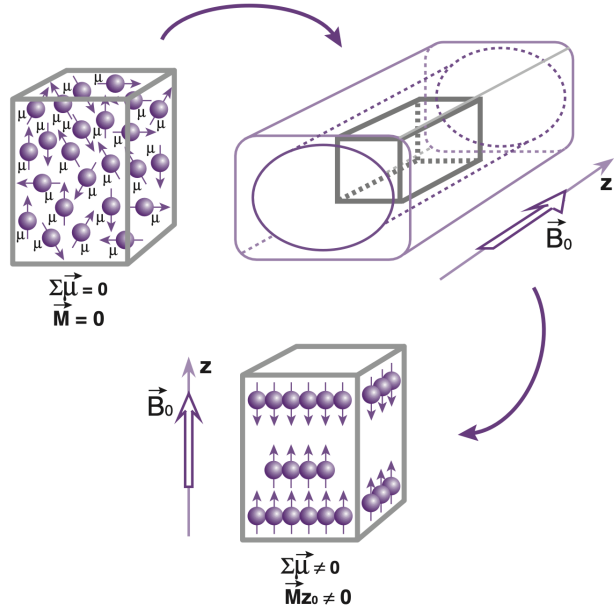


Figure 1.2: Influence of the external magnetic field on net magnetization [4]

particle such as depicted on Figure 1.3 where the precession movement is compared to the behavior of a spinning top under the influence of earth's gravity.

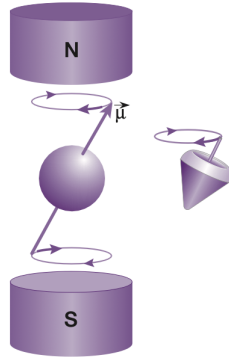


Figure 1.3: Precession movement of a hydrogen nucleus [4]

This precession movement can further be characterized by its angular frequency of rotation around the axis of the particle which is directly proportional to the applied external magnetic field, and called the Larmor frequency:

$$\nu_0 = \frac{\gamma}{2\pi} B_0, \quad (1.2)$$

where  $\gamma$  is the gyromagnetic ratio in  $\text{MHz T}^{-1}$  specific to each nuclei ( $\frac{\gamma}{2\pi} = 42,58 \text{ MHz T}^{-1}$  for  $^1H$ ) [4, 5, 6].

Regarding the macroscopic magnetization, the alignment of the individual magnetic

moments under the influence of the external magnetic field leads to a non-zero net magnetization,

$$\vec{M} = \frac{1}{V} \sum \vec{\mu}_i, \quad (1.3)$$

where  $V$  is the volume of the ensemble of spins and  $\vec{\mu}_i$  is the magnetic moment vector of an individual nucleus in  $V$ . Moreover, the two spin orientations described in the first paragraph of this section and called spin up or down, correspond to two different energy states:  $E_\uparrow$  for spin up and which corresponds to the lower energy state, and  $E_\downarrow$  for spin down and which corresponds to the higher energy state [4, 5, 6]. The difference between the energies of the two states can be calculated as:

$$\Delta E = E_\downarrow - E_\uparrow = h \frac{\gamma}{2\pi} B_0 = \hbar\omega_0, \quad (1.4)$$

where  $h$  is Planck's constant ( $h = 6,6 \cdot 10^{-34}$  Js). Formula 1.4 shows that the energy difference is proportional to the Larmor frequency ( $\nu_0$ ) and that the two energy states have a different occupation rate. The state occupancy ratio can be expressed in thermal equilibrium conditions using Boltzmann distribution:

$$\frac{N_\uparrow}{N_\downarrow} = \exp\left(\frac{\delta E}{kT}\right) = \exp\left(\frac{h\omega_0}{kT}\right), \quad (1.5)$$

where  $T$  is the absolute temperature in K and  $k$  is Boltzman's constant ( $k = 1,38 \cdot 10^{-23}$  JK $^{-1}$ ). Formula 1.5 indicates that the lower energy state ( $E_\downarrow$ ) is more populated than the higher energy state ( $E_\uparrow$ ). As an illustrative example, for a 0.5 T external magnetic field at body temperature, this distribution difference is around 2 protons per million [4]. The net macroscopic magnetization is therefore non-zero and leads to an equilibrium magnetization denoted  $M_0$ :

$$M_0 = \frac{\left(\frac{\gamma}{2\pi}\right)^2 h^2 \rho B_0 m_s (m_s + 1)}{3kT}, \quad (1.6)$$

where  $\rho$  is the spin density (number of spins per unit volume) [5].

### 1.1.3 Radiofrequency pulse

The equilibrium macroscopic magnetization expressed in Eq. 1.6 is directly proportional to the spin density and to the square of the gyromagnetic ratio of the particle. Since both of these quantities are large for hydrogen ( ${}^1H$ ) atoms, it yields a large equilibrium macroscopic magnetization.

However, the resulting macroscopic magnetization ( $\vec{M}_0$ ) is oriented in the direction of the external magnetic field ( $\vec{B}_0$ ) and the magnetization is infinitely small compared

to the applied external magnetic field. Moreover, the individual spins precess around  $B_0$  at the Larmor frequency ( $\nu_0$ ) with randomly distributed phases making it impossible to directly measure  $\vec{M}_0$ . In order to create a magnetization in a different direction than  $\vec{B}_0$ , a time-varying radiofrequency pulse, called RF-pulse, oscillating at the Larmor frequency of the nuclei ( $f_{RF} = \nu_0$ ), and thus oscillating on resonance with the nuclei, can produce a linearly polarized magnetic field with a fixed orientation [5]. In the case that the external magnetic field ( $\vec{B}_0$ ) is oriented along the  $O_z$  axis in an orthonormal plane, the magnetic field created by the RF-pulse will be oriented in the  $(x,y)$ -plane in order to be perpendicular to  $B_0$ . The expression of the magnetic field associated to the RF-pulse is:

$$\vec{B}_1(t) = 2B_1(t) \cos(2\pi f_{RF}t + \phi) \vec{I}_{xy}. \quad (1.7)$$

The representation of the effects of the RF-pulse can be visualized in the fixed laboratory frame  $(x,y,z)$  as depicted in (a) on Figure 1.4 or, for more convenience, in the rotating frame  $(x',y',z'=z)$  that is rotating around the  $O_z$  axis with angular velocity  $\omega_0 = 2\pi\nu_0$  as depicted in (b) on Figure 1.4.

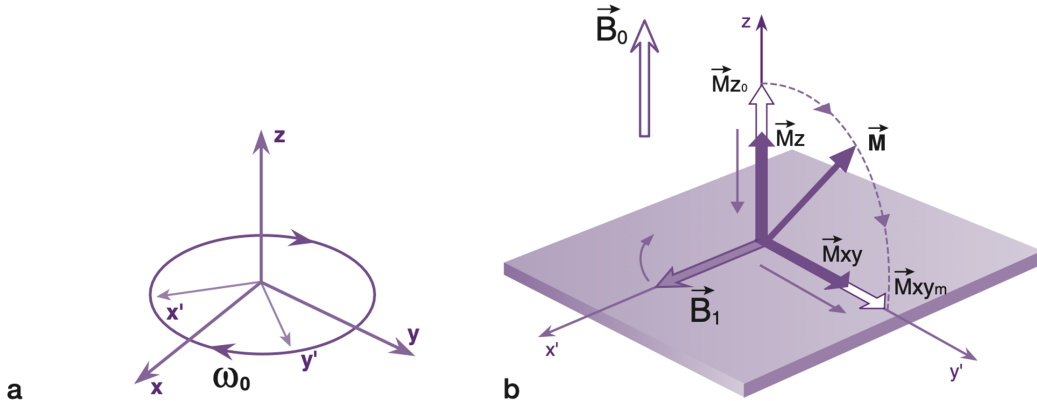


Figure 1.4: Precession movement in (a) the laboratory frame and in (b) the rotating frame [4]

The application of the RF-pulse results in the tilting of the magnetization over an angle ( $\alpha$ ) defined as the flip angle:

$$\alpha = \gamma \int_{T_{RF}} B_1(t) dt, \quad (1.8)$$

where  $T_{RF}$  is the duration of the pulse. The most common RF-pulses are the pulses for which the duration time is adjusted such that  $\alpha = 90^\circ$  and  $\alpha = 180^\circ$  yielding  $90^\circ$ -pulses and  $180^\circ$ -pulses respectively. Since the magnetization  $\vec{M}$  is tilted away from the  $O_z$  axis, a new component in the  $(x,y)$ -plane noted  $M_{xy}$  appears [4, 5, 6]. The magnetization can then be expressed as follows:

$$\vec{M} = M_z \vec{1}_z + M_{xy} \vec{1}_{xy}, \quad (1.9)$$

where  $M_z$  is called longitudinal magnetization and  $M_{xy}$  transverse magnetization. For better understanding, a closer look can be taken at the effect of a typical  $90^\circ$ -pulse and  $180^\circ$ -pulse as represented in Figure 1.5.

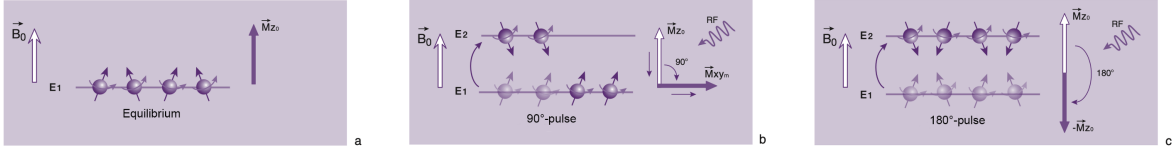


Figure 1.5: (a) resting state, (b)  $90^\circ$ -pulse and (c)  $180^\circ$ -pulse, adapted from [4]

The new states generated by the RF-pulses visible on Figure 1.5 are unstable implying a de-excitation phase in order to return to the resting state. This de-excitation phase is described by two phenomena referred to as relaxation mechanisms.

#### 1.1.4 Relaxation types

Following the application of the RF-pulse, the system returns to equilibrium following two distinct relaxation mechanisms allowing the observation of the Nuclear Magnetic Resonance (NMR) phenomenon [4, 5, 6].

##### T1-relaxation

The first relaxation process is called the spin-lattice relaxation or longitudinal relaxation and is usually referred to as *T1-relaxation*. During this relaxation process, energy exchanges between the spins of the system and the external environment lead to the recovery of the net magnetization ( $M_z(t)$ ) to its original value  $M_0$ . This recovery process is mathematically described by the formula:

$$M_z(t) = M_0(1 - \exp \frac{-t}{T_1}) + M_z(0) \exp \frac{-t}{T_1}, \quad (1.10)$$

where  $T_1$  is the characteristic time representing the time needed to recover 63% of the longitudinal magnetization  $M_z$  such as depicted in Figure 1.6. The  $T_1$  characteristic times are usually comprised between 500 and 1000 ms in biological tissues for a 1.5 T external magnetic field [7].

In Equation 1.10, we can observe that the longitudinal magnetization ( $M_z(t)$ ) exponentially returns to its original value. Physically, this relaxation process is caused by the transition of the spins from the high energy state  $E_\downarrow$  to the low energy state  $E_\uparrow$ , as previously explained using Figure 1.5. The energy released from the transitions between the two energy states is then transferred to the external environment (spin-network relaxation). The efficiency of this energy transfer varies from one external environment

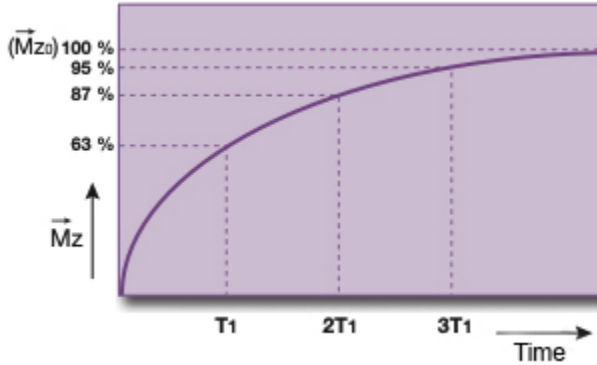


Figure 1.6: Exponential recovery of the net magnetization against  $T_1$  relaxation time, adapted from [4]

to another which leads to different relaxation times ( $T_1$ ) for different biological media according to the molecular collision frequency in the medium ( $\nu_c$ ) as depicted in Figure 1.7.

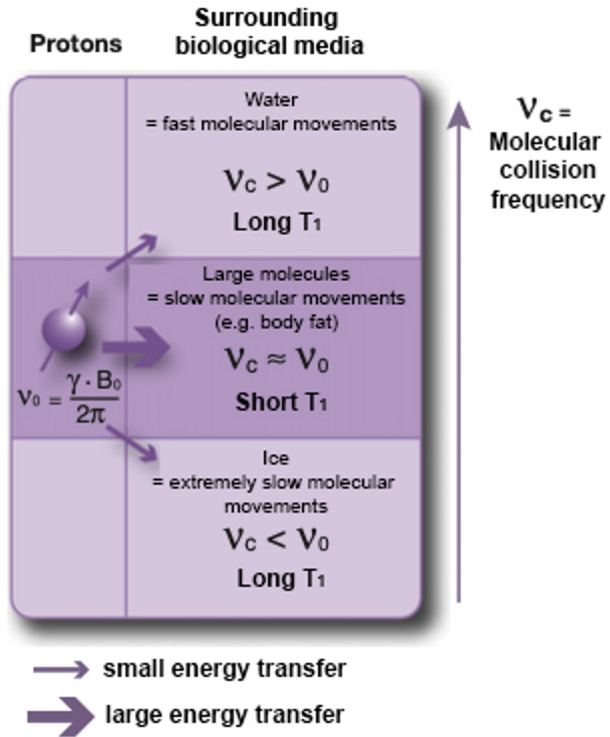


Figure 1.7: Spin-network relaxation for different biological media, adapted from [4]

More precisely and, as indicated on Figure 1.7, the characteristic time  $T_1$  will be short when the molecular collision frequency ( $\nu_c$ ) is similar to the Larmor frequency ( $\nu_0$ ) of the spins. On the other hand,  $T_1$  will be long for dissimilar molecular collision frequency

( $\nu_c$ ) and Larmor frequency ( $\nu_0$ ) of the spins [4, 5, 6].

### T2-relaxation

The second relaxation process is called the spin-spin relaxaion or transverse relaxation and is usually referred to as *T2-relaxation*. During this second relaxation process, interactions between the spins of the system lead to a loss in coherence of the spin phases due to the fact that each proton does not have the exact same precession frequency since they occupy a slightly different biological medium. This second relaxation mechanism does not involve energy exchanges contrary to the *T1-relaxation* mechanism. The recovery of the transverse magnetization ( $M_{xy}(t)$ ) is expressed in terms of the characteristic time  $T_2$ :

$$M_{xy}(t) = M_{xy}(0) \exp \frac{-t}{T_2}, \quad (1.11)$$

where  $T_2$  is the characteristic time representing the time needed to loose 63% of the transverse magnetization  $M_{xy}$  such as depicted in Fig.1.8. The  $T_2$  characteristic times are usually comprised between 50 and 100 ms in biological tissues for a 1.5 T external magnetic field [7].

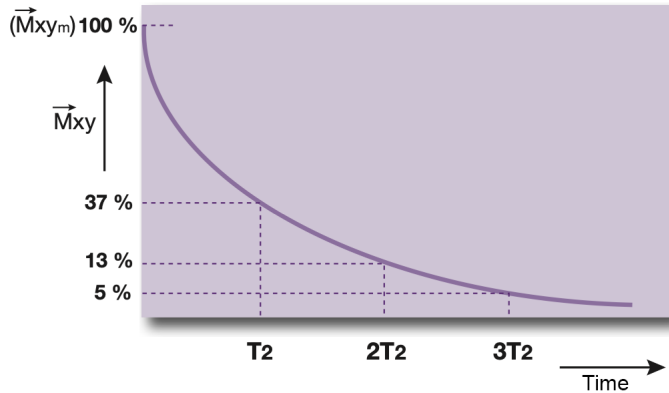


Figure 1.8: Exponential recovery of the net magnetization against  $T_2$  relaxation time, adapted from [4]

In practice, however, the spin-spin relaxation process occurs faster than expressed in the mathematical formula 1.11 as the external magnetic field ( $B_0$ ) is not perfectly homogeneous. Indeed, besides the spin-spin interactions, fluctuations and inhomogeneities in the external magnetic field, due to internal limitations of the magnets used, also influence the loss in coherence of the spins phases [4, 5, 8]. In order to take these effects into account, a third characteristic relaxation time noted  $T_2^*$  must be introduced.  $T_2^*$  is called the effective relaxation time and can be expressed as follows:

$$\frac{1}{T_2^*} = \frac{1}{T_2} + \gamma \Delta B_0. \quad (1.12)$$

### 1.1.5 Free Induction Decay

The oscillating evolution of the transverse magnetization induces a signal called the Free Induction Decay (FID) signal. Since Faraday's law of electromagnetism states that a changing magnetic flux through a closed loop induces an electromotive force ( $\epsilon$ ) over the ends of the loop, the FID signal can be measured using a coil placed in the transverse plane [4, 9]. The coil transforms the FID signal into a measurable electronic signal shaped as an exponentially damped sinusoidal signal with an envelope decreasing exponentially according to the  $T_2^*$  characteristic time constant. The coil actually measures the decay in transverse magnetization  $\vec{M}_{xy}$  such as depicted on Figure 1.9.

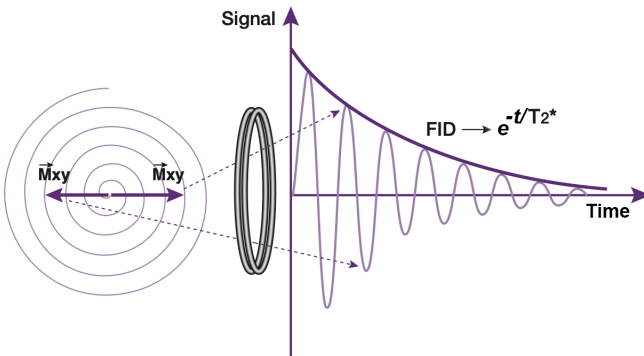


Figure 1.9: Dephasing of the transverse magnetization and measurement of the FID, adapted from [4]

### 1.1.6 Spin-echo sequence

Since the FID signal is rapidly decreasing due to the  $T_2^*$ -relaxation, it is not actually measured in magnetic resonance imaging. Instead, a pulse sequence consisting of two RF-pulses of  $90^\circ$  and  $180^\circ$  respectively, and called spin-echo sequence, is commonly used to circumvent the inhomogeneities of the external magnetic field. In more details, this sequence follows the time sequence described in Figure 1.10. At time  $t = 0$ , the  $90^\circ$ -pulse is applied and converts the longitudinal magnetization into transverse magnetization. The dephasing of the spin isochromats<sup>1</sup> induced by the magnetic field inhomogeneities is countered by the application of the  $180^\circ$ -pulse at time  $t = \tau$  which results in the refocusing of the spin isochromats at time  $t = 2\tau$ . This specific time is also called Spin Echo (SE) time and thus represents the time at which the *echo* is observed and measured. The spin echo sequence is characterized by two main parameters: the Echo Time (TE) which is defined as the time between the  $90^\circ$ -pulse and the first echo, and the Repetition Time (TR) which is defined as the time between two succeeding  $90^\circ$ -pulses [4, 5].

<sup>1</sup>"The magnetization from a group of spins in an infinitesimally small volume element in which the magnetic field can be considered homogeneous is denoted spin isochromat." [5]

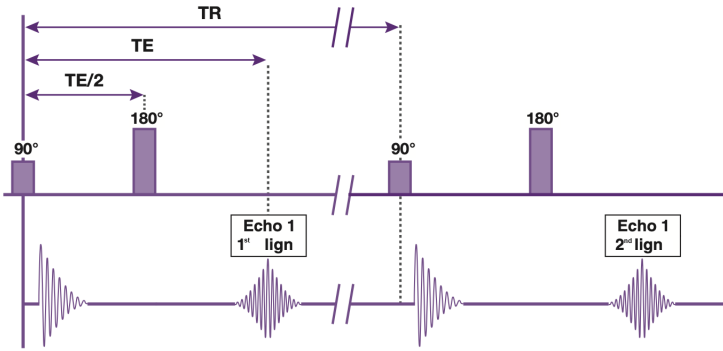


Figure 1.10: Spin echo sequence, adapted from [4]

Spin-Echo pulse sequences are one of the earliest developed sequence in Magnetic Resonance Imaging and are still abundantly used today. The adjustment of the two main time parameters TE and TR is performed to obtain contrasted medical images such as *T1-weighted* images, *T2-weighted* images and *proton density* images [10].

### 1.1.7 Magnetic Resonance Imaging contrast

Contrast in MRI is used to highlight differences in relaxation times as well as in proton density. Through the fine tuning of the MRI sequence parameters, it is possible to obtain T1, T2 and proton density contrasts allowing for weighted visualizations of the main components of the brain such as white matter (WM), grey matter (GM) and cerebrospinal fluid (CSF).

#### T1 contrast

T1-weighted imaging relies on the longitudinal relaxation of a tissue's net magnetization and is characterized by a short TR (400 to 600 ms), to promote T1 contrast, and by a short TE (15 ms), to minimize T2 contrast (see Figure 1.11). More precisely, body fat quickly realigns its longitudinal magnetization with the external magnetic field  $B_0$  whereas water has much slower longitudinal magnetization realignment resulting in a high signal (bright on image) and a low signal (dark on image) respectively. The key parameter is thus TR as selecting a TR shorter than a specific tissue's recovery time allows for the differentiation of the different types of biological tissues [4, 11]. The obtained contrasted image is thus generally used to distinguish the WM from the GM as the WM is represented in white or light grey, the GM in grey and the CSF in black.

#### T2 contrast

T2-weighted imaging, on the other hand, relies on the transverse relaxation of the net magnetization and is characterized by a long TR (2000 ms), to minimize T1 contrast, and by a long TE (120 ms), to promote T2 contrast (see Figure 1.12). Physically, T2 weighting is based on the fact that spins are decaying from their aligned precession after the RF pulse application. The T2-weighted images display the WM in black or

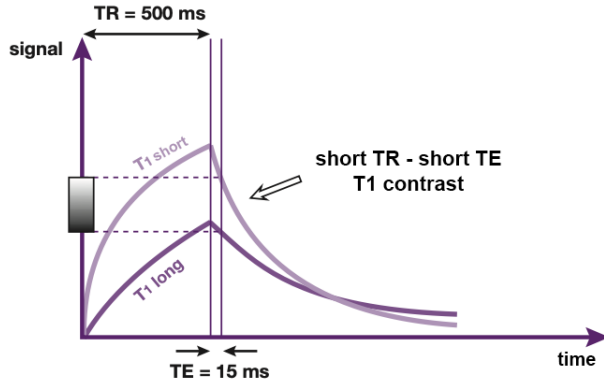


Figure 1.11: T1 contrast principle, adapted from [4]

dark grey, the GM in grey and the CSF in white [4, 12].

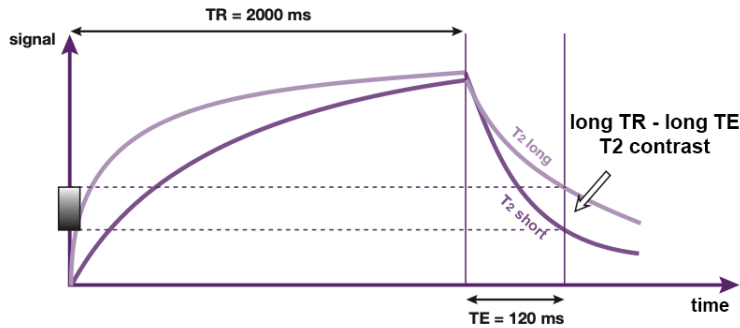


Figure 1.12: T2 contrast principle, adapted from [4]

### Proton density contrast

Proton density weighting in images is related to the number of nuclei in the area being imaged and this contrast is obtained by using a long TR ( $> 2000$  ms), to minimize T1 contrast, and a short TE (20 ms), to minimize T2 contrast (see Figure 1.13). A higher proton density will appear brighter on the image and the proton density images display the WM in grey, the GM in light grey and the CSF in dark grey [4, 13].

Table 1.1 summarizes the comparison between T1-weighted, T2-weighted and proton density weighted images.

### 1.1.8 Magnetic Resonance Imaging acquisition

The first step in the magnetic resonance imaging acquisition process is the addition of spatial information about the signal received through the selective excitation of spins in a well-defined slice. The spatial encoding of the signal relies on two essential notions: the use of magnetic field gradients to encode the three spatial directions of the signal and the application of the Fourier transform to obtain the resulting images.

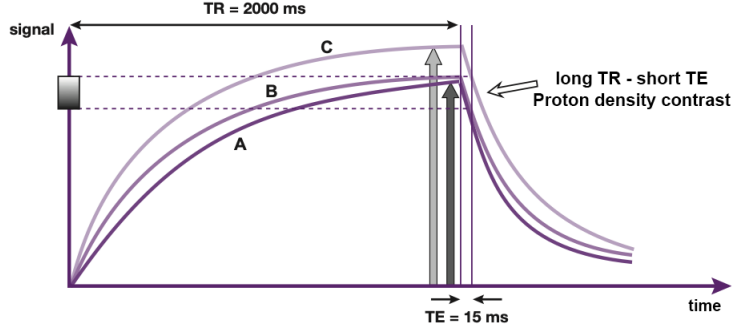


Figure 1.13: T2 contrast principle - tissues A & B have the same proton density whereas tissue C has a greater proton density resulting in different signals, adapted from [4]

Tissue	T1-weighted	T2-weighted	Proton density
CSF	Dark	Bright	Dark
WM	Light	Dark grey	Dark grey
GM	Grey	Light grey	Light grey
Fat (within bone marrow)	Bright	Light	Light
Inflammation (infection, demyelination)	Dark	Bright	Bright

Table 1.1: Comparison between T1-weighted, T2-weighted and proton density weighted images, adapted from [14]

The first magnetic gradient applied is a linear magnetic gradient used to select a slice of interest, perpendicular to the direction of application of the gradient, in the anatomical body and is called the slice-select gradient, noted  $G_{ss}$ . Since the slice-select gradient is applied in the same direction as the external magnetic field  $B_0$  (along  $O_z$ ), the Larmor frequency (precession frequency) of spins will vary linearly along the direction of propagation of the gradient (see Formula 1.13) as the  $G_{ss}$  superimposes with  $B_0$  :

$$f(z) = \frac{\gamma}{2\pi}(B_0 + G_{ss}z), \quad (1.13)$$

Therefore, the application of a RF-pulse with a specific bandwidth ( $\Delta f$ ) results in the excitation of spins located only in the slice of interest [4, 5].

In the case of a spin-echo sequence, the chronology of the selective RF-pulses and of the magnetic field gradients can already be summarized as illustrated on Figure 1.14. The first  $90^\circ$ -pulse is applied simultaneously with the slice-select gradient  $G_{ss}$  such that the spins in the selected slice all precess at the same frequency. The same slice-select gradient  $G_{ss}$  must also be applied at the same time as the  $180^\circ$ -pulse in order to re-focus all of the excited spins. However, as the slice-select gradient is a linear gradient, protons in the center of the selected slice will be perfectly in phase whereas protons on the extremities of the slice will undergo a slight dephasing due to  $G_{ss}$ . In order to

compensate this slight phase shift, a second gradient of inverse polarity lasting for half of the first positive lobe duration must be applied (+2/-1 ratio gradient).

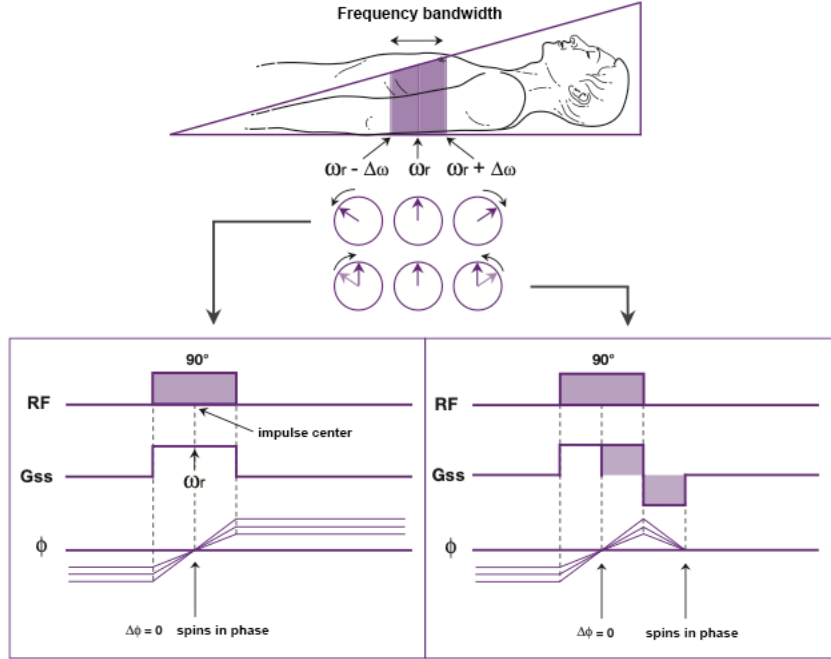


Figure 1.14: Bipolar slice-select gradient principle, adapted from [4]

After the protons contained in the slice of interest have been excited, spatial information has to be encoded in the measured signal in order to localize the spins. In order to proceed with the spatial encoding of the signal, a second magnetic gradient called the phase encoding gradient and noted  $G_\Phi$  must be applied. This second gradient is applied perpendicularly to the slice-select gradient  $G_{ss}$  and influences linearly the precession frequency of protons perpendicular to the direction of propagation of  $G_\Phi$  (along  $O_y$ ):

$$\Phi(y) = -\gamma G_y y T_y, \quad (1.14)$$

where  $T_y$  is the duration of application of the phase encoding gradient influencing the degree of defocusing of the protons [4] [5].

Finally, a third magnetic gradient is applied along the last spatial direction ( $O_x$ ) and is referred to as the frequency encoding gradient, noted  $G_\omega$ . This last magnetic gradient influences the precession frequency of protons perpendicular to its direction and, in order to observe this phase shift in the measured signal, the phase encoding gradient must be applied exactly when the signal is collected. This is the reason why  $G_\omega$  is often referred to as the readout gradient.

To summarize, the slice-select gradient  $G_{ss}$  is used to isolate the anatomical volume of interest then, the phase encoding gradient  $G_\Phi$  and the frequency encoding gradient  $G_\omega$  encode the vertical and horizontal spatial positions of each point in the slice, respectively.

Each amplitude of the phase encoding gradient  $G_\Phi$  allows the measurement of a line in the Fourier space, also called k-space, which contains the raw frequency information of the MR signal measured. It is thus necessary to repeat this cycle for multiple values of  $G_\Phi$  in order to completely fill the k-space (see Figure 1.15). The different values taken by  $G_\Phi$  are comprised between a positive maximum value and a negative minimum value (bipolar gradient) and each value changes for every new cycle by a constant step [4, 5].

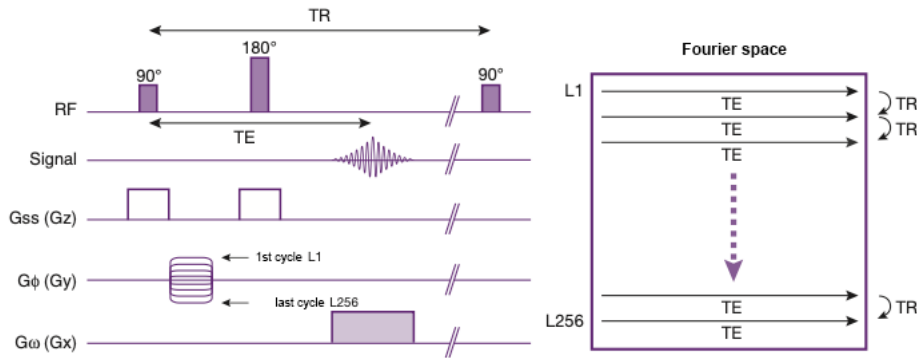


Figure 1.15: Complete chronology of RF-pulses and gradient applications for a spin-echo sequence, adapted from [4]

### 1.1.9 Magnetic Resonance Imaging artifacts

Magnetic Resonance images can be altered by different type of artifacts which can significantly impact the MRI exam and affect the diagnostic quality. Examining the general feature of an artifact in order to identify the type of the artifact allows one to understand its origin and its effect on the medical images. More precisely, MRI artifacts can be classified into five distinct groups based on their general features [14, 15, 16].

#### Patient and physiologic motion artifacts

As the duration of MRI acquisition sequences varies between a few minutes up to over an hour, it becomes impossible to completely restrain patients' motion. The movement of body tissues and fluids during the acquisition time result in motion artifacts. Depending on the motion type, motion artifacts will have different effect on the MR image. Periodic motion such as swallowing, breathing, cardiac movement, blood flow, CSF pulsation or peristalsis result in well defined ghost artifacts (faint copies of the image superimposed on the image) whereas random motion such as physical movement of a patient produce a smear in the phase direction (see Figure 1.16 A). Motion artifacts can be reduced by cardiac or respiratory gating, saturation bands, patient immobilization or through the use of fast MRI techniques such as echo-planar imaging (EPI) [16],

17, 18, 19].

### Tissue heterogeneity and foreign bodies artifacts

Tissue heterogeneity results in chemical shift artifacts at the interface between tissues with different composition and thus different chemical properties, such as water and fat. As the chemical composition of water and fat differ from one another, these tissues will have different resonance frequencies resulting in spatial misregistration of fat and water molecules in the slice select direction. Chemical shift artifacts appear as dark or bright bands on borders of structures with different chemical compositions (see Figure 1.16 B) and their effect can be reduced by increasing the bandwidth, using a low field strength scanner or using fat suppressed imaging [16, 19, 20]. The proximity of foreign bodies during the MRI acquisition sequence may generate magnetic field inhomogeneities which, in turn, impact the local signal. These distortion artifacts, called magnetic susceptibility artifacts, are usually generated by the proximity of compounds, such as metallic hardware or dental work, containing ferromagnetic materials (strong artifacts) or paramagnetic and diamagnetic materials (weak artifacts). Magnetic susceptibility artifacts appear as darkening in a portion of the image (see Figure 1.16 C), which indicates a signal dropout, and can be alleviated by removing the metallic compound from the scan and by using short echo time (TE) imaging sequences [19, 21].

### Fourier transform and Nyquist sampling theorem artifacts

Artifacts can arise through the use of the inverse Fourier transform to convert the k-space map into the MR image. Mathematically, the Fourier transform at high-contrast boundaries requires a nearly infinite number of frequencies to be constructed. However, as the reconstruction from k-space is performed through a finite sampling, only a finite number of frequencies can be sampled causing an oscillation in the reconstructed image. The Fourier series is said to be truncated, hence the name truncation artifact. These artifacts are known as Gibbs artifacts, also called truncation artifact or ringing artifact, and appear as series of fine parallel lines ("ringing") adjacent to a high-contrast interface such as the CSF-spinal cord and the skull-brain interface (see Figure 1.16 D). Increasing the matrix size and performing k-space post-processing, such as the application of smoothing filters, can reduce Gibbs artifacts [16, 19, 22]. Aliasing, or wrap-around, artifacts are often visible on MR images and arise when field-of-view (FOV) is smaller than the body part being imaged. Visually, the part of the body outside of the FOV is superimposed, or wrapped around, on the opposite side of the image (see Figure 1.16 E). Aliasing artifacts can be removed by enlarging the FOV or by using an anti-aliasing software [16, 19, 23].

### MRI hardware and software artifacts

The complex hardware and software constituting the MR scanner also cause a number of artifacts such as Moiré fringes, Zipper artifacts or aliasing. Moiré fringes appear as repeated interference pattern of irregular bright and dark bands (see Figure 1.16) and are due to the imperfect homogeneity of the main magnetic field from one side of the body to the other. These fringes can also be created through the constructive

and destructive interference of signals arising from different sides of the body [19, 24]. Zipper artifacts appear when a spurious RF signal contaminates the signal picked up by the receiver, and can be seen as interfering bands of electronic noise on the image (see Figure 1.16) [19, 25].

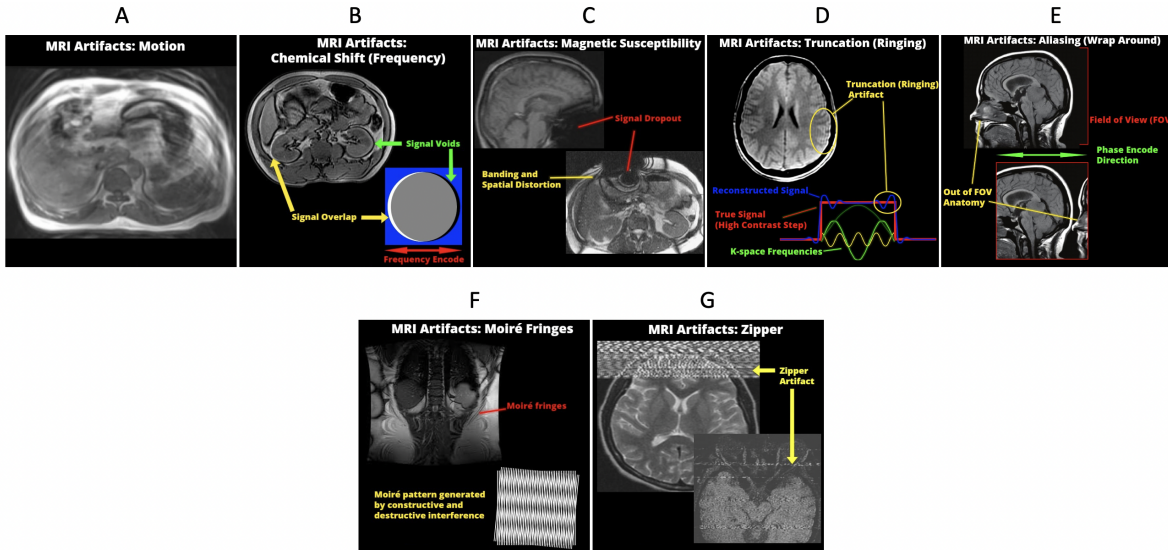


Figure 1.16: MRI artifacts: (A) Motion artifact; (B) Chemical shift artifact; (C) Magnetic susceptibility artifact; (D) Gibbs artifact; (E) Aliasing artifact; (F) Moiré fringes; (G) Zipper artifacts, adapted from [19]

## 1.2 Diffusion Weighted Magnetic Resonance Imaging

Diffusion-weighted Imaging (DWI) is a form of MR imaging relying on the quantification of water molecule movements, based on differences in the magnitude of diffusion of these water molecules within a voxel of tissue. The random thermal diffusion of water molecules in a free environment follows the principles of Brownian motion, which is described as isotropic. Within the brain, however, the diffusion of water molecules is influenced by a number of factors, such as the temperature or the microenvironmental architecture. The diffusion of water molecules within the brain can be described by two types of movement (represented on Figure 1.17): free or isotropic diffusion, observable in the CSF, and restricted or anisotropic diffusion, observable along brain WM tracts. Through the use of the appropriate diffusion sensitive MR sequences, the different rates in water molecules diffusion can be measured and further interpreted into image contrast. The images obtained by DW-MRI thus carry information about the organization and microscopic architecture of the tissues surrounding the water molecules and are often used for early identification of ischemic stroke and differentiation of acute from chronic stroke [6, 26, 27].

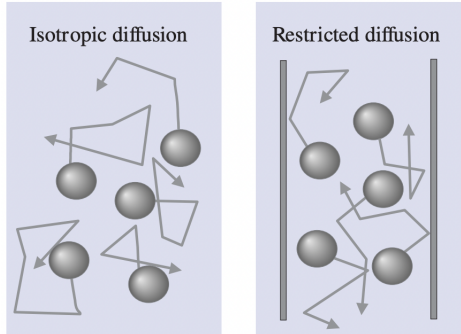


Figure 1.17: Water molecular motion types, adapted from [28]

### 1.2.1 Pulse Gradient Spin Echo

In order to extract spatial information about water molecules diffusion and generate qualitative diffusion maps, specific sequences must be used. The most popular sequence is, by far, a sequence based on the SE sequence (see section 1.1.6), called the Pulse Gradient Spin-Echo (PGSE) sequence composed of two large and equal diffusion gradients, placed on either side of the  $180^\circ$ -pulse, as visible on Figure 1.18 [27] [28].

As shown on Figure 1.18, a first diffusion gradient is applied after the  $90^\circ$ -pulse causing a phase shift in molecules which is then, in theory, canceled out by a second gradient, applied after the  $180^\circ$ -pulse refocusing pulse. In practice, this is effectively the case only for non-moving stationary protons. Indeed, moving spins are not perfectly refocused by the  $180^\circ$ -pulse resulting in an effective phase shift causing an attenuation of the measured signal. The influence of the motion of protons on the phase shift experienced is illustrated on Figure 1.19.

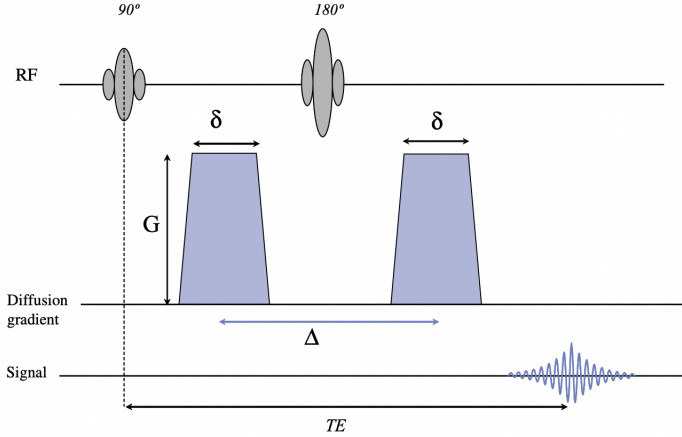


Figure 1.18: PGSE sequence diagram, adapted from [28]

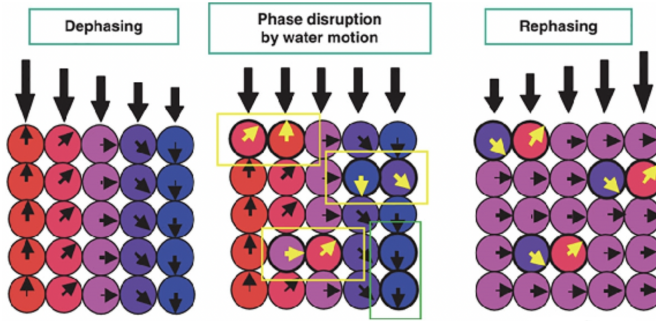


Figure 1.19: Effects of molecular motion on phase shift with a pair of gradients. Large black arrows represent the strength of the magnetic field; small black arrows indicate phases of individual protons; proton motion in between gradient application is represented by colored boxes, adapted from [29]

The diffusion motion of water molecules in the brain thus results in the contrast of the MR signal, which can be tuned by varying the time between the onset of the two gradients, the duration and the intensity of the applied gradients. These parameters characterize the PGSE sequence and are defined by the degree of weighting or *b-value* ( $\text{s/mm}^2$ ) defined as:

$$b = (\gamma G \delta)^2 (\Delta - \frac{\delta}{3}), \quad (1.15)$$

where  $\gamma$  is the gyromagnetic ratio,  $G$  the gradient intensity,  $\delta$  the gradient duration and  $\Delta$  the time between the onset of the two gradients [27, 28]. The DW-MR images are obtained using *b*-values ranging from 0, without diffusion weighting, up to  $5000 \text{ s/mm}^2$  achieving high contrast. As explained here above, watery tissues that have very mobile molecules, experiencing free diffusion, give a lower signal intensity whilst more solid and static tissues, experiencing restricted diffusion, give a stronger signal. The signal strength is described by the Stejskal-Tanner equation:

$$S(b) = S(0)\exp(-bD), \quad (1.16)$$

where  $S(b)$  is the signal for b-value  $b$  and  $D$  is the self-diffusion constant of the tissue [28].

In MRI, DWI maps often display the apparent diffusion coefficient (ADC) which shows the diffusion rate in each voxel for a specific b-value. This coefficient can be calculated from two DWI maps: a first map obtained using a null b-value, for which no diffusion weighting is applied, and a second map obtained using a b-value  $b$ . The ADC ( $\text{mm}^2/\text{s}$ ) is an absolute quantitative measurement of water motion and is expressed by the following formula:

$$\text{ADC} = -\log\left(\frac{S(b)}{S(0)}\right)/b, \quad (1.17)$$

where  $S(b)$  is the signal for b-value  $b$  and  $S(0)$  is the signal for a null b-value [28]. Physically, areas of the brain with free diffusion (e.g. CSF) will have a high ADC value and thus appear bright on the ADC maps. Conversely, areas of the brain with restricted diffusion (e.g. GM and WM) appear dark on the ADC maps [26, 27].

### 1.2.2 Diffusion Tensor Imaging

The diffusion motion of molecules is, however, a three-dimensional phenomenon dependent on the microstructural architecture and physiologic factors of the brain. The scalar ADC coefficient, introduced here above, does not take the directionality of the diffusion into account and it is necessary to introduce a mathematical construct, known as the diffusion tensor. The imaging technique based on the use of a diffusion tensor is called Diffusion Tensor Imaging (DTI) and uses anisotropic diffusion to characterize the organization of the brain tissues [6, 27, 30]. The diffusion tensor is composed of nine values, each corresponding to a gradient and cell orientation, and is expressed as follows:

$$\mathbf{D} = \begin{pmatrix} D_{xx} & D_{xy} & D_{xz} \\ D_{yx} & D_{yy} & D_{yz} \\ D_{zx} & D_{zy} & D_{zz} \end{pmatrix}, \quad (1.18)$$

where the first set of subscripts  $(x,y,z)$  refers the cell orientation and the second set to the gradient orientation. In practice, there is a degree of redundancy and  $\mathbf{D}$  is symmetric ( $D_{xy} = D_{yx}$ ;  $D_{xz} = D_{zx}$ ;  $D_{yz} = D_{zy}$ ) implying that, in order to be completely determined, diffusion data must be measured in a minimum of six noncollinear orientations. To obtain a DTI metric map for an anisotropic tissue, the tensor components as well as a null b-value image (baseline reference image) are required. Once these measurements are obtained, it becomes possible to characterize the diffusion of molecules and thus to infer on the properties of brain tissues. Indeed, a tensor is a mathematical

tool representing an ellipsoid and, its three eigenvalues  $\lambda_1$ ,  $\lambda_2$  and  $\lambda_3$  and three eigenvectors  $v_1$ ,  $v_2$  and  $v_3$  represent the magnitude and directions of the three major planes of the diffusion ellipsoid (see Figure 1.20), respectively [6, 27].

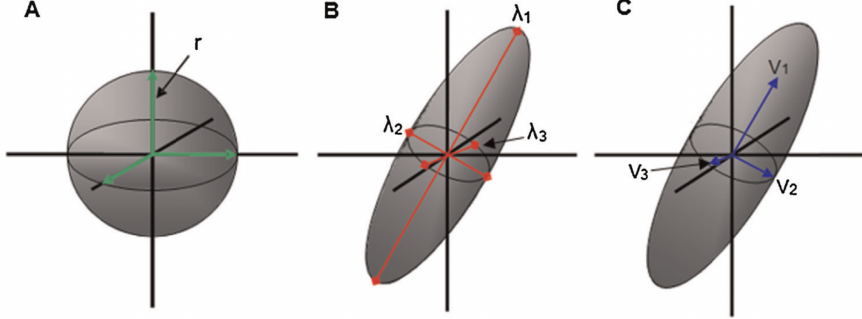


Figure 1.20: (A) Isotropic diffusion; (B) restricted diffusion with tensor eigenvalues; (C) restricted diffusion with tensor eigenvectors, adapted from [6]

The relationship between  $\mathbf{D}$  and its eigenvalues and eigenvectors can be expressed as follows:

$$\mathbf{D} = \mathbf{Q} \cdot \Lambda \cdot \mathbf{Q}^{-1}, \quad (1.19)$$

where  $\Lambda$  is the diagonal eigenvalue matrix and  $\mathbf{Q}$  is the eigenvector matrix

$$\mathbf{Q} = \begin{pmatrix} q_{1x} & q_{2x} & q_{3x} \\ q_{1y} & q_{2y} & q_{3y} \\ q_{1z} & q_{2z} & q_{3z} \end{pmatrix}, \quad \Lambda = \begin{pmatrix} \lambda_1 & 0 & 0 \\ 0 & \lambda_2 & 0 \\ 0 & 0 & \lambda_3 \end{pmatrix}. \quad (1.20)$$

As the DTI tensor is computed, diffusion maps containing indications about the magnitude and dominant direction of the diffusion process can be extracted. Various metrics, detailed in the next sections, can then be computed in order to infer on the microstructure of brain tissue. The process of following the dominant direction of diffusion voxel by voxel is known as tractography and will be reviewed in a further section.

### Mean Diffusivity (MD)

The trace of the DTI tensor  $\mathbf{D}$  is used as an indicator of the overall mean motion of molecules in a given voxel and is computed as follows:

$$Tr(\mathbf{D}) = D_{xx} + D_{yy} + D_{zz} = \lambda_1 + \lambda_2 + \lambda_3. \quad (1.21)$$

The mean diffusivity (MD) can then be computed as the mean of the trace and can be interpreted as an inverse measure of the membrane density:

$$MD = \frac{Tr(\mathbf{D})}{3} = \frac{\lambda_1 + \lambda_2 + \lambda_3}{3}. \quad (1.22)$$

The MD value will be similarly low for GM and WM and will display higher values in the CSF as molecules undergo less restricted diffusion. MD is sensitive to cellularity, edema, and necrosis and a MD map is displayed on Figure 1.21 [31, 32].

### Axial Diffusivity (AD)

Axial diffusivity (AD) is computed along the direction of maximal diffusion, which corresponds to the first eigenvector ( $\nu_1$ ) associated to the first eigenvalue ( $\lambda_1$ ), and is equal to the latter:

$$AD = \lambda_1. \quad (1.23)$$

AD tends to be variable in WM changes and pathology, and is used to infer on axonal integrity as AD decreases in axonal injury [31, 32]. An AD map is shown on Figure 1.21.

### Radial Diffusivity (RD)

In order to determine the radial diffusivity (RD), the second ( $\lambda_2$ ) and third ( $\lambda_3$ ) eigenvalues are used, and it represents the diffusivity perpendicular to the principal direction of diffusion:

$$RD = \frac{\lambda_2 + \lambda_3}{2}. \quad (1.24)$$

RD is used to represent myelination integrity as RD increases in WM after de-myelination [31, 32]. A RD map is shown on Figure 1.21.

### Fractional Anisotropy (FA)

This last metric is the most commonly used metric to measure the degree of anisotropy in a voxel. Fractional anisotropy (FA) quantifies the ratio between the magnitude of the anisotropic component of the DTI tensor  $\mathbf{D}$  and the magnitude of  $\mathbf{D}$ . FA values vary between 0 and 1 and serves as a rotationally invariant scalar that quantifies the shape of  $\mathbf{D}$ . FA can be calculated in each voxel:

$$FA = \sqrt{\frac{3}{2}} \sqrt{\frac{(\lambda_1 - MD)^2 + (\lambda_2 - MD)^2 + (\lambda_3 - MD)^2}{\lambda_1^2 + \lambda_2^2 + \lambda_3^2}}. \quad (1.25)$$

A FA value of 0 corresponds to the case when the tensor is completely isotropic and the diffusion tensor is represented as a sphere. On the other hand, a FA value of 1 represents maximal anisotropic diffusion as diffusion is bound to a single axis and the diffusion tensor is illustrated as an ellipsoid (see Figure 1.20). A FA map (visible on Figure 1.21) is obtained as the FA values are calculated in every voxel. On these maps, areas with a high degree of anisotropic diffusion are bright whereas areas with low

anisotropic diffusion appear dark [27, 28, 31]. The FA metric is used as an indicator of the microstructural integrity in the brain (high FA values indicate high WM integrity) but it is not specific to the type of microstructural change [32]. In the literature, FA maps are often displayed as RGB FA maps, visible on Figure 1.21, in which each color is used to represent one of the three principal direction of diffusion (eigenvalues of the diffusion tensor:  $\lambda_1$ ,  $\lambda_2$ ,  $\lambda_3$ ) (Red: left-right; Green: anterior-posterior; Blue: superior-inferior), useful for a quick overview of the FA values.

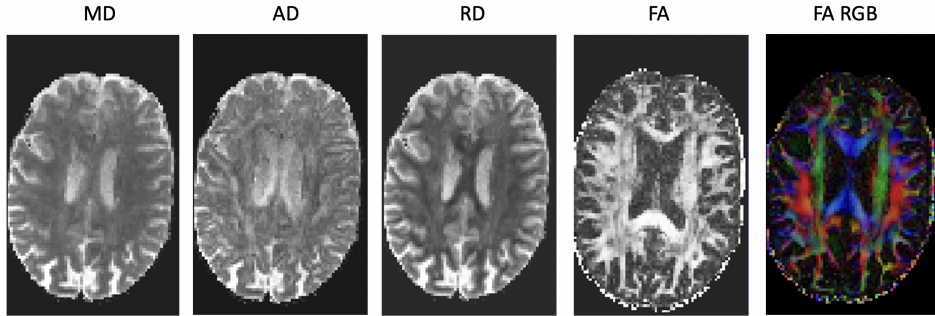


Figure 1.21: Diffusion Tensor Imaging metrics maps: Mean Diffusivity (MD); Axial Diffusivity (AD); Radial Diffusivity (RD); Fractional Anisotropy (FA), Red-Green-Blue Fractional Anisotropy

### Advantages and Limitations

Diffusion tensor imaging allows the extraction of relevant rotationally invariant metrics yielding information about the integrity of the brain microstructure in a non-invasive way. As stated before, DTI can also be used to isolate WM bundles through a process called tractography and is extensively used for clinical studies and as an aid for diagnosis. Despite these advantages, DTI presents some important limitations requiring a cautious interpretation of its metrics. The major limitation of this diffusion model relies in its assumption. Indeed, DTI is based on the assumption that the diffusion of water molecules follows a Gaussian distribution implying that only a single-fiber population can be modeled at each voxel. In other words, the impact of multiple crossing fiber populations is not taken into account by this model. In these voxels, the Gaussian distribution assumption does not hold and the resulting DTI metrics value may lead to misinterpretations of the actual anatomical microstructure. For example, a voxel containing two organized but crossing fiber populations will result in a low FA value on the FA map which could be wrongly interpreted by the user. Multiple complex fiber population organizations can present the same DTI metric value (i.e. a reduction in FA may be caused by a reduction in neurite density or an increase in the dispersion of neurite orientation distribution [33]) indicating that these metrics should be carefully interpreted. Therefore, it is necessary to go beyond DTI through the use of higher order microstructural models giving more precise information about the brain microstructure [31, 34].

### 1.2.3 Tractography

As mentioned here above, white matter tracts bundles can be determined using the direction and magnitude of the water diffusion in each voxel. Fiber tractography is a three dimensional reconstruction technique allowing the identification of the trajectories of white matter tracts. This technique relies on powerful mathematical algorithms and on the idea that if the local principal direction of anisotropic diffusion (represented by the direction of the principal eigenvector) in a voxel is known, integrating along these principal direction allows the reconstruction of the whole white matter tract [27]. Figure 1.22 shows the visually intuitive 3D RGB (same color code as FA RGB maps) images, showing the course of brain white matter pathways in th brain, obtained using tractography [27, 30].



Figure 1.22: Whole-brain tractogram obtained from DTI metrics, adapted from [31]

Concretely, deterministic and probabilistic algorithms can be used to perform local fiber tracking starting from a seed location and following the preferred diffusion direction until a target is reached. Deterministic models (e.g. Fiber Assignment by Continuous Tracking (FACT) model) are more basic as they follow the direction with the highest probability from a distribution within each voxel, and may lead to erroneous results as they are sensitive to noise. In contrast, probabilistic models (e.g. Constrained Spherical Deconvolution - Fiber Orientation Distribution (CSD-FOD) model) follow, in each voxel, a direction of propagation taken at random from a distribution based on the diffusion data in the voxel. Probabilistic models are more robust as they are able to better deal with noise. Figure 1.23 illustrates the difference between these two types of models through a basic tracking example.

## 1.3 Microstructural models

The limitations of DW-MRI and DTI make the interpretation of their metrics not straightforward and it is thus required to use more advanced models enabling the reconstruction of higher-order information. These advanced models are referred to as microstructural models relying on biophysical assumptions about the microstructure of white matter tissue and based on the partition of voxels into multi-compartment models [34].

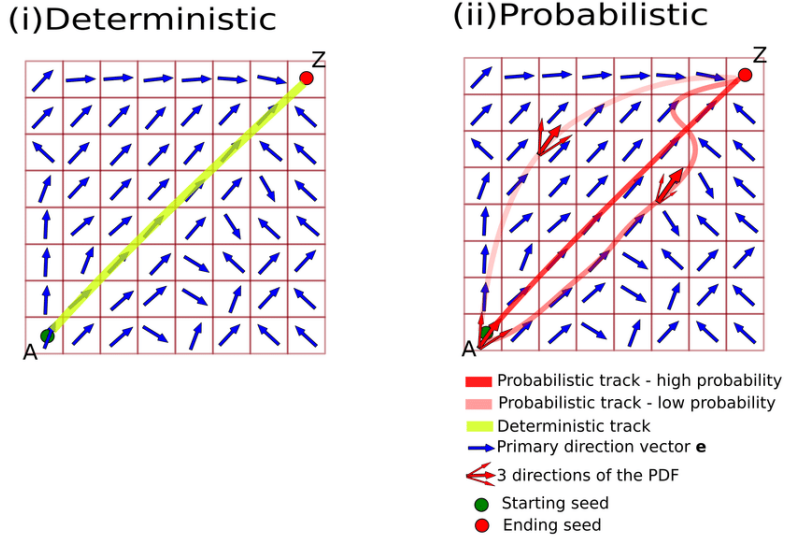


Figure 1.23: Basic example showing the difference between deterministic and probabilistic tracking models, adapted from [35]

### 1.3.1 NODDI

The Neurite Orientation Dispersion and Density Imaging (NODDI) model is a multi-compartment model using diffusion MRI to infer on the microstructural complexity of dendrites and axons of the brain. This advanced model proposed by Zhang et al. [33] is used to perform *in vivo* neurite (axons and dendrites) orientation dispersion and density imaging allowing to capture the main features of neurite morphology. High-order information about neurite morphology can further be used to infer on the brain functions in normal and pathological populations as it carries information about brain development and aging [33].

The NODDI model is based on the separation of three distinct tissue compartments: intracellular (intraneurite) water, extracellular (extraneurite) water and cerebrospinal fluid (CSF) compartments. As each of these three compartments present different diffusion motion properties, they each give rise to a particular MR signal and the total normalized signal can be expressed as follows:

$$A = (1 - \nu_{iso})(\nu_{ic}A_{ic} + (1 - \nu_{ic})A_{ec}) + \nu_{iso}A_{iso}, \quad (1.26)$$

where  $A_{ic}$ ;  $A_{ec}$ ;  $A_{iso}$  and  $\nu_{ic}$ ;  $\nu_{ec}$ ;  $\nu_{iso}$  are the normalized signal and volume fraction of the intracellular; extracellular; and CSF compartments respectively [33].

#### Intracellular model

The intracellular or intraneurite compartment refers to the space in between the membrane of neurites and is modeled as a set of sticks representing cylinders of zero radius. Modeling using this set of sticks allows the representation of the diffusion pattern

followed by water molecules near neurites which is highly restricted perpendicular to neurites and unrestrained parallel to neurites. It then becomes possible to model highly oriented (as in WM) to bending or sprawling neurite bundles (as in GM) through orientation distribution of the set of sticks. Mathematically, the normalized signal generated by the intraneurite compartment is expressed as follows:

$$A_{ic} = \int_{\mathbb{S}^2} f(\mathbf{n}) \exp(-bd_{\parallel}(\mathbf{q} \cdot \mathbf{n})^2) d\mathbf{n}, \quad (1.27)$$

where  $\mathbf{q}$  is the gradient direction,  $b$  is the DW b-value,  $f(\mathbf{n})$  is the sticks orientation distribution function,  $\exp(-bd_{\parallel}(\mathbf{q} \cdot \mathbf{n})^2)$  gives the signal attenuation due to unhindered diffusion along a stick with intrinsic diffusivity  $d_{\parallel}$  and orientation  $\mathbf{n}$ . More precisely, the sticks orientation distribution function follows a Watson distribution:

$$f(\mathbf{n}) = M\left(\frac{1}{2}, \frac{3}{2}, \kappa\right)^{-1} \exp(\kappa(\mu \cdot \mathbf{n})^2), \quad (1.28)$$

where  $M$  is a confluent hypergeometric function<sup>2</sup>,  $\mu$  is the mean orientation of the set of sticks, and  $\kappa$  is the concentration parameter that measures the extent of orientation dispersion about  $\mu$ . This distribution is defined such that  $f(\mathbf{n})d\mathbf{n}$  gives the probability of finding sticks along the orientation  $\mathbf{n}$  [33].

### Extracellular model

In the extracellular compartment, designating the space around neurites, the diffusion of water molecules is hindered by the presence of various glial cells and cell bodies but remains unrestricted. The diffusion motion is modeled by a Gaussian anisotropic distribution and the set of modeling sticks is also used to express the normalized signal of the extraneurite compartment:

$$A_{ec} = -b\mathbf{q}^T \left( \int_{\mathbb{S}^2} f(\mathbf{n}) D(\mathbf{n}) d\mathbf{n} \right) \mathbf{q}, \quad (1.29)$$

where  $D(\mathbf{n})$  is a cylindrically symmetric tensor with the principal direction of diffusion  $\mathbf{n}$ ,  $d_{\parallel}$  and  $d_{\perp}$  are diffusion coefficients parallel and perpendicular to  $\mathbf{n}$ , respectively. While  $d_{\parallel}$  for the extracellular compartment as for the intracellular compartment,  $d_{\perp}$  is defined with a simple tortuosity model which links these two diffusivity coefficients:

$$d_{\perp} = d_{\parallel}(1 - \nu_{ic}), \quad (1.30)$$

which expresses the fact that  $d_{\parallel}$  and  $d_{\perp}$  are directly related to the neurite morphology [33].

---

<sup>2</sup>In mathematics, the Gaussian or ordinary hypergeometric function is a special function represented by the hypergeometric series, that includes many other special functions as specific or limiting cases [36].

## CSF model

The third compartment uses an isotropic Gaussian distribution to characterize the unconstrained water molecules diffusion motion and is referred to as the CSF compartment. The normalized signal is then expressed as follows:

$$A_{iso} = \exp(-bd_{iso}), \quad (1.31)$$

where  $d_{iso}$  is the isotropic diffusion coefficient [33].

## Parameters

Once the NODDI model is correctly fitted, three interesting parameters, enabling *in vivo* estimation of neurite organization, can be extracted from this model: the neurite density index (NDI), the fiber orientation dispersion index (ODI) and the volume fraction of isotropic diffusion ( $\nu_{iso}$ ). The NDI estimates the packing density of neurites (axons and dendrites) in a given voxel. The ODI gives information about the variability of the orientational configuration of neurites in a given voxel and ranges from 0 (totally coherent and parallel neurites) to 1 (randomly oriented neurites). The ODI is computed as:

$$ODI = \frac{2}{\pi} \arctan \frac{1}{\kappa}, \quad (1.32)$$

Finally,  $\nu_{iso}$  illustrates the free water isotropic volume fraction [33] [37].

Figure 1.24 shows a summary of the three compartments composing the NODDI model as well as its most interesting parameters.

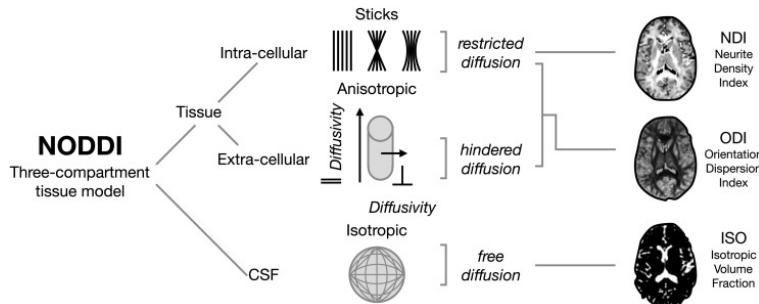


Figure 1.24: NODDI compartments and parameters, adapted from [37]

## Advantages and Limitations

The NODDI multi-compartment biophysical model allows the acquisition of biologically interpretable indices, in a clinically feasible manner, whereas DTI metrics are often not straightforward to interpret. Diffusion MRI multi-compartment models, however, make explicit assumptions about the underlying tissue microstructure and about the resulting diffusion properties of water molecules. The simplifying assumptions imposed by the

NODDI model allows to facilitate model fitting and to avoid degeneracies but are its main limitations as it can lead to erroneous parameter estimation. Moreover, the fixed parameters introduced in the model such as the fixed intrinsic diffusivity ( $d_{\parallel}$ ) for both intra- and extracellular compartments may lead to inaccurate parameter estimation. The assumption made on the modeling of dentrites and axons as a set of sticks has been shown to be acceptable for myelinated axons but tends to be inexact for dentrites. Finally, the use of a simplified three compartment biophysical model does not take into account the contributions from other tissue compartments such as the cell bodies and glial cells and, therefore, is not capable of estimating more complex neuritic spatial configurations. Although the NODDI model allows identification of neurobiologically interpretable parameters for heterogeneous tissue microstructures, the optimization of NODDI parameters as well as improvements on its key assumptions require further research in order to yield more accurate results [33, 37].

### 1.3.2 DIAMOND

The DIistribution of 3D Anisotropic MicrOstructural eNvironments in Diffusion-compartment imaging (DIAMOND) model is a biophysical multi-compartment model developed by Scherrer et al. [38], that uses statistical modeling to provide a more detailed model of the tissue microstructure. The DIAMOND model considers that each voxel is composed of heterogeneous populations characterized by a statistical distribution of diffusivities (see Figure 1.25). These populations are modeled within each voxel by a large number of homogeneous and heterogeneous 3D spin packets. The use of 3D spin packets allows to model their interaction with homogeneous part of the brain microstructure through anisotropic 3D Gaussian diffusion. The diffusion properties of each spin packet are described by means of a diffusion tensor  $\mathbf{D}$  which translates the restriction and hindrance to diffusion experienced by the water molecules. The fraction of spin packets with a diffusion tensor  $\mathbf{D}$  is represented by a matrix-variate distribution  $P(\mathbf{D})$  which can be put in relation with the DW signal  $S_k$  obtained for b-value  $b_k$ :

$$S_k = S_0 \int_{\mathbf{D} \in Sym^+(3)} P(\mathbf{D}) \exp(-b_k \mathbf{g}_k^T \mathbf{D} \mathbf{g}_k) d\mathbf{D}, \quad (1.33)$$

where  $S_0$  is the signal obtained for b-value  $b_0$ ,  $Sym^+(3)$  is the set of  $3 \times 3$  symmetric positive-definite matrices and  $\mathbf{g}_k$  is the diffusion gradient [38].

In order to account for the heterogeneity of the microstructural environment, the modeling of the composition of each compartment is defined by a peak-shaped distribution ( $P(\mathbf{D})$  visible on Figure 1.25). Indeed, if the characterization was done though the use of delta functions,  $P(\mathbf{D})$  is then defined as  $P(\mathbf{D}) = \delta(\mathbf{D} - \mathbf{D}^0)$ , and it would represent a homogeneous microstructural environment with diffusion tensor  $D^0$  in each voxel, which is equivalent to DTI. The peak-shaped distributions allow for a more realistic modeling of the multiple compartments and are mathematically described by the matrix-variate Gamma ( $mv - \Gamma$ ) distribution:

$$P_{\kappa,\Sigma}(\mathbf{D}) = \frac{|\mathbf{D}|^{\kappa-(p+1)/2}}{|\Sigma|^{\kappa}\Gamma_p(\kappa)} \exp(-Tr(\Sigma^{-1}\mathbf{D})), \quad (1.34)$$

$$\Gamma_p(\kappa) = \pi^{p(p-1)/4} \prod_{j=1}^p \Gamma(\kappa - (j-1)/2), \quad (1.35)$$

where  $\kappa$  is the shape parameter ( $\kappa > (p-1)/2$ ),  $\Sigma$  is the scale parameter ( $\Sigma \in Sym^+(p)$ ) and  $\Gamma_p(\kappa)$  is the multivariate gamma function. As illustrated on Figure 1.25, this distribution function can describe different population types. Indeed, a narrow peak distribution is used to capture globally homogeneous populations whereas a broad peak distribution is used to model heterogeneous populations. If  $N_p$  populations of spin packets are considered in every voxel and if the composition of each population is captured by a  $mv - \Gamma$  distribution of spin packets, the voxel total distribution is:

$$P(\mathbf{D}) = \sum_{j=1}^{N_p} f_j P_{\kappa_j, \Sigma_j}(\mathbf{D}), \quad (1.36)$$

where  $f_j \in [0, 1]$  are the fractions of occupancy ( $\sum_{j=1}^{N_p} f_j = 1$ ). It then becomes possible (by combining Equation 1.33 and Equation 1.36) to have a generic expression of the DW signal arising from heterogeneous populations of heterogeneous spin packets:

$$S_k = S_0 \sum_{j=1}^{N_p} f_j \int_{\mathbf{D} \in Sym^+(3)} P_{\kappa_j, \Sigma_j} \mathbf{D} \exp(-b_k \mathbf{g}_k^T \mathbf{D} \mathbf{g}_k) d\mathbf{D}, \quad (1.37)$$

As the DIAMOND 3D spin packets model is fitted, the modeling of multiple heterogeneous compartments within each voxel becomes possible provided that the number of compartments is specified by the user. DIAMOND then enables the direct assessment of compartment-specific diffusion characteristics such as the compartment mean diffusivity, axial diffusivity, radial diffusivity and fractional anisotropy (cMD, cAD, cRD and cFA) as well as an overall measure of heterogeneity for each compartment (cHEI) [38].

### Advantages and Limitations

Even though the DIAMOND multi-compartment model is able to accurately characterize the 3D diffusion motion of water molecules in multiple heterogeneous compartments, one limitation remains. Indeed, in order to be able to infer on the microstructural changes, the number of compartment must be set by the user. In practice, however, the number of compartments is usually set to three so as to capture isotropic, hindered and restricted diffusion [38].

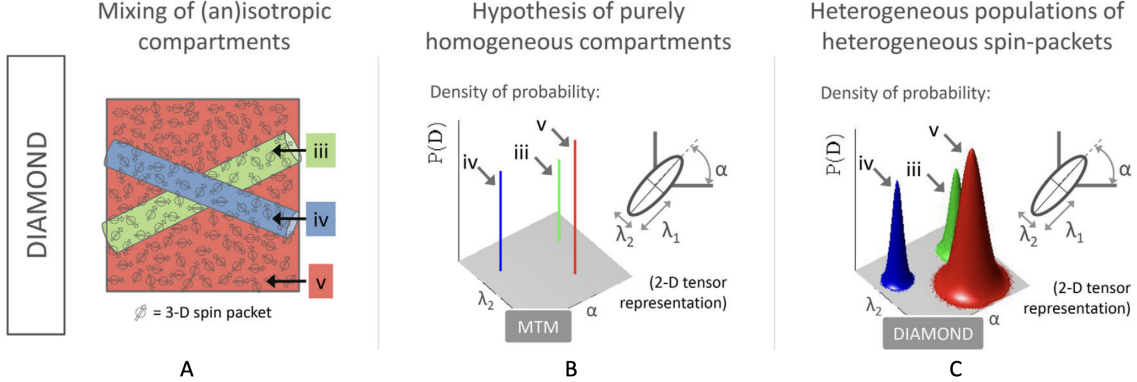


Figure 1.25: DIAMOND model: (A) Multi-compartment model with isotropic (red) and anisotropic (blue and green) compartments; (B) Multi-Tensor Model with purely homogeneous compartments; (C) DIAMOND peak-shaped distributions of multidimensional diffusivities accounting for heterogeneity in each compartment, adapted from [38]

### 1.3.3 Microstructure fingerprinting

Contrary to the NODDI and DIAMOND models which rely on assumptions made about the tissue microstructure and the underlying diffusion processes, the Microstructure Fingerprinting (MF) model relies on Monte Carlo simulations of the random motion of water molecules. The MF model, developed by Rensonnet et al. [39], assumes that the DW-MRI signal  $S$  arising from each voxel corresponds to the independent contribution of multiple compartments constituted of  $K$  fascicles of axons with different orientations ( $\mathbf{u}_1, \dots, \mathbf{u}_k$ ) and volume fractions ( $\nu_1, \dots, \nu_k$ ), and of a partial volume CSF ( $\nu_{CSF}$ ) compartment (see Figure 1.26). Using the superposition principle in the diffusion environment, the DW-MRI signal can be expressed as:

$$S = M_0 \left[ \sum_{k=1}^K \nu_k A_{fasc}(\Omega_k, \mathbf{T}_k, \mathbf{u}_k; \mathbf{g}) + \nu_{CSF} A_{CSF}(D_{CSF}, \mathbf{T}_{CSF}; \mathbf{g}) \right] \quad (1.38)$$

$$= \sum_{k=1}^K w_k A_k + w_{CSF} A_{CSF}, \quad (1.39)$$

where  $M_0$  is a scaling factor capturing the net initial transverse magnetization,  $A_k$  is the normalized DW-MRI signal of the  $k$ -th fascicle modeled by a Monte Carlo simulation and  $w_k$  is the signal weight of the  $k$ -th fascicle contribution in the NMR-apparent signal [39].

Based on this, a wide dictionary containing multiple single-fascicle DW-MRI signals, called fingerprints, are created for various microstructural configurations using Monte Carlo simulations. Once this dictionary is created, the model is fitted to the information contained in the DW-MRI signal by selecting the optimal sparse combination of fingerprints (see Figure 1.26). The selection is done by solving a sparse optimization problem

such that the selected fingerprints allow the characterization of the microstructural properties [39].

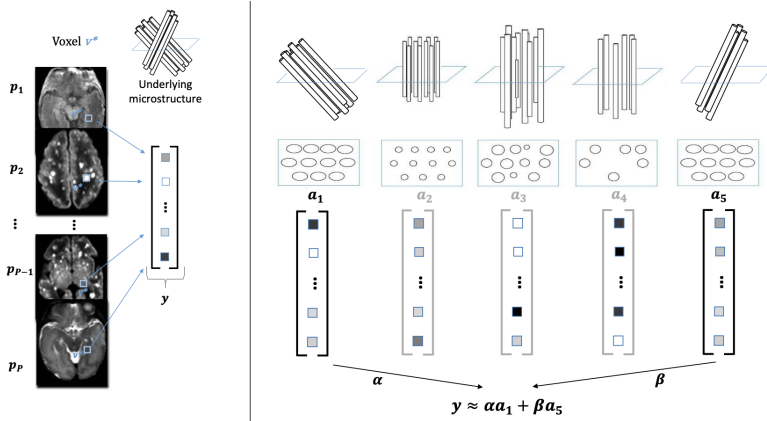


Figure 1.26: Microstructure fingerprinting model sparse dictionary matching between the acquisition  $y$  and the linear combinations of signals  $a_1, a_2, \dots$  stored in the dictionary, adapted from [40]

### Advantages and Limitations

Monte Carlo simulations of the random walk of water molecules used in the MF model allow the characterization of various geometry of cellular environments and has been shown to provide microstructural parameters showing better correspondence with histology than the multi-compartment models such as NODDI and DIAMOND. The tissue geometry selected for the Monte Carlo simulations and the superposition principle used to derive Equation 1.38 are, however, not perfectly identical to what is observed in reality and further improvement should be made to characterize the tissue at the single-fascicle level [39].

## 1.4 ElikoPy pipeline

This second section provides a detailed explanation of the ElikoPy Python library, developed by Dessain Q. and Simon M. in the framework of their Master's thesis [41], aiming at correcting common DW-MRI artifacts (see Section 1.1.9) for large-scale population studies. The ElikoPy library is a complete diffusion MRI processing pipeline improving the interpretation of the dMRI results and allowing the computation of multiple microstructural diffusion models such as DTI (see Section 1.2.2), NODDI (see Section 1.3.1), DIAMOND (see Section 1.3.2) and MF (see Section 1.3.3) on large databases and for different types of acquisitions [42].

The pipeline supports various state-of-the-art medical imaging file formats as input, such as the Brain Imaging Data Structure (BIDS) format<sup>3</sup>, the Digital Imaging and Communication in Medicine (DICOM) format<sup>4</sup> and the Neuroimaging Informatics Technology Initiative (NIfTI) format<sup>5</sup>. The implementation of the processing of these files is mainly based on existing Python packages already widely used for dMRI data processing. The main packages used are: the Diffusion Imaging in Python (DiPy) package [46], the Diffusion Microstructure Imaging in Python (Dmipy) package [47] and the MF package [39]. The pipeline also uses the FSL software [48], Freesurfer [49], Advanced Normalization Tools (ANTs) [50], Itktools [51] and Mrtrix3 [52]. Using its large set of available functions, the ElikoPy pipeline is used to process the data following a set of steps regrouped on Figure 1.27.

### 1.4.1 Preprocessing

The very first step consists in an evaluation of the data to be processed. The image dimensions is checked to make sure it corresponds to the dimensions of the b-value and b-vector files along the acquisition parameters and index files. If the correspondence is validated, a dedicated storage folder for each subject is generated and the preprocessing of the data can be performed in order to correct the non idealities of the raw images. The preprocessing of the raw data is then subsequently divided into several successive steps as illustrated on Figure 1.28.

#### Reslice

The clinical MRI scanners usually perform an automatic interpolation step in order to obtain high resolution images. However, the intrinsic resolution is not augmented by this time consuming interpolation step making it not ideal for research purposes. The reslicing step is thus used to deal with the disadvantages caused by the interpolation

---

<sup>3</sup>BIDS is a file format organizing neuroimaging and behavioral data based on simple file formats and folder structures to reflect current lab practices [43].

<sup>4</sup>DICOM is used for the integration of medical imaging devices like printers, servers or scanners from various vendors and also contains identification data of each patient for uniqueness [44].

<sup>5</sup>NIfTI provides coordinated and targeted service, training, and research to speed the development and enhance the utility of informatic tools related to neuroimaging [45].

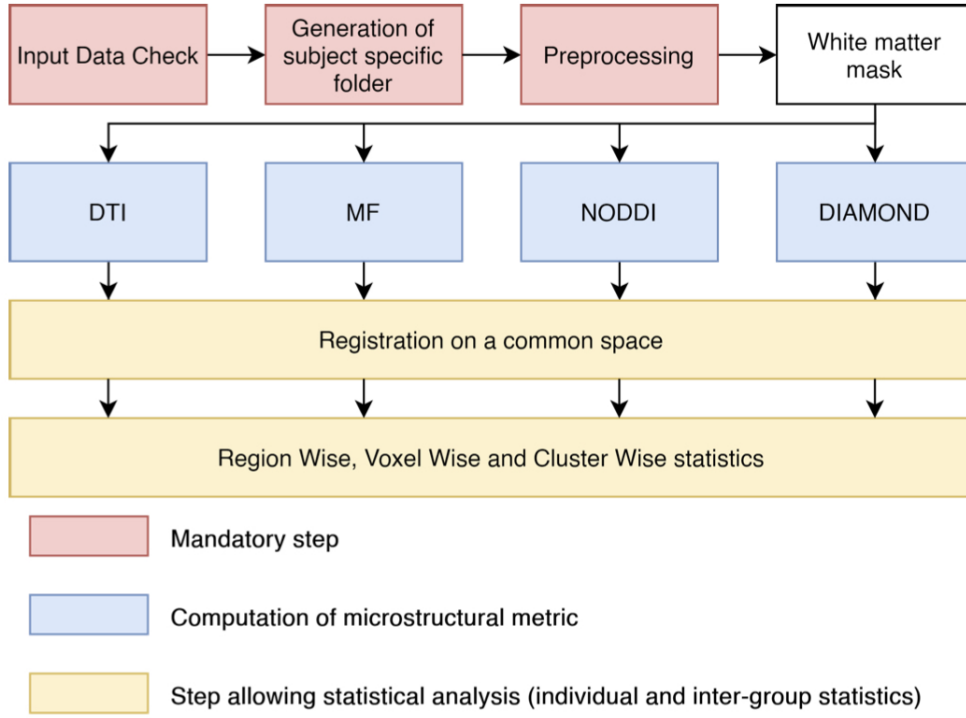


Figure 1.27: Overview of the main processing steps in the ElicoPy pipeline, adapted from [41]

step and to ensure isotropic voxels. The reslicing step is performed using the `align DiPy` function [42].

### Brain extraction

A brain mask departing the brain tissues from the skull and the other surrounding tissues is then extracted and further used in the subsequent preprocessing steps. This step allows for computational time gains and is usually required by diffusion image processing algorithms. The brain mask is obtained using the `median_otsu` DiPy function [42].

### MPPCA denoising

Principal Component Analysis of Marchenko-Pastur (MPPCA) is used to reduce the Rician noise usually present in MR images. This methods allows a fast denoising of the images without creating additional artifacts or blurring the anatomical structures in the images. The uncorrelated noise is then removed from the MR images. The MPPCA denoising step is carried out by using the `mppca` DiPy function [42].

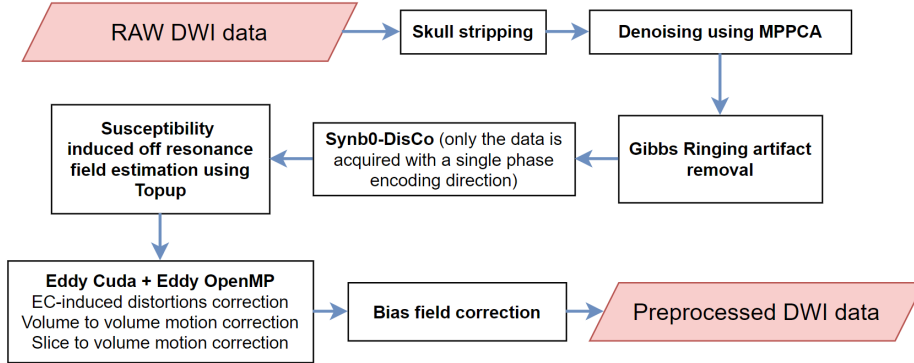


Figure 1.28: Preprocessing steps of the ElikoPy pipeline [42]

### Gibbs ringing correction

The Gibbs artifacts described in Section 1.1.9 can be removed using the `gibbs_removal` DiPy function [42]. As the data used in this Master's thesis is unaffected by Gibbs ringing artifacts, this preprocessing step was skipped.

### 1.4.2 Motion, Eddy current and susceptibility distortion correction

The displacement and deformation artifacts caused by motion, Eddy current and magnetic susceptibility differences near junctions of tissues (see Section 1.1.9) present the same features and can thus be jointly corrected. The susceptibility distortions are first estimated using the `topup` FSL tool and then corrected using the `eddy` FSL tool [42].

### Bias field correction

The inhomogeneities of the external magnetic field inside the MR scanner have to be accounted for in order to avoid variability of the signal in tissues of the same type which can directly affect microstructural metrics computation. This correction is carried out by using the N4 Bias Field Correction ANTs package [42]. As the field inhomogeneities are already corrected for the data used in this work, this correction has not been performed.

### 1.4.3 White matter mask extraction

The preprocessing steps are then followed by the extraction of a white matter mask useful to accelerate the computation of the microstructural models metrics. If a T1 image is available for the considered data, a white matter mask can be directly computed using this image. On the other hand, the white matter mask can be computed using the diffusion data if the T1 image is unavailable. The extraction of the mask is done by using the `white_mask` ElikoPy function [42].

#### 1.4.4 Diffusion models and metrics

The ElicoPy pipeline can further be used to extract the features and metrics of four different microstructural models. Indeed, the DTI, NODDI, DIAMOND and MF metrics can be computed from the preprocessed diffusion data. The DTI metrics are computed using the DiPy library, DIAMONDS metrics are computed using the work of Scherrer et al. [38], NODDI metrics are obtained using the Dmipy library and MF metrics are determined using the work of Rensonnet et al. [39] [42].

#### 1.4.5 Statistical analysis

As the microstructural diffusion metrics are computed, the ElicoPy pipeline gives the possibility to calculate basic group comparison statistics useful to rapidly analyze key brain tissue changes [42].

# CHAPTER 2

## STROKE PATHOLOGY

This second chapter offers an overview of the causes and consequences of the stroke pathology, and provides a narrative review of state-of-art methodological aspects of dMRI data analysis used to characterize the impact of strokes on the brain microstructure.

### 2.1 Pathophysiology and Treatment of Stroke

Stroke is a deadly and debilitating neurological disorder characterized by loss of blood flow, or even the blockage of blood vessels, in the brain. The formation of clots in the brain leads to poor and interrupted blood flow, clogging arteries and causing blood vessels to break, leading to bleeding. The lack of oxygen caused by the interrupted blood flow results in the death of brain cells, affecting the proper functioning of the brain. Despite being the second cause of death and one of the main causes of loss of Disability-Adjusted Life Years (DALYs) worldwide, prevention and post-stroke treatments still need improvements as the global burden of this condition remains substantial [53] [54] [1].

#### 2.1.1 Epidemiology of Stroke

In 2010, estimated figures of the impact of stroke worldwide indicate that 16.9 million incident strokes occurred and that stroke was the cause of 5.9 million deaths (see Table 2.1). The statistical analysis of these figures show that the incidence of stroke and the number of stroke survivors increased over the years in low-and-middle income countries but the incidence of stroke has declined in high-income countries. Moreover, the absolute number of DALYs due to stroke increased over the past 30 years due to population growth and increased life expectancy resulting in a greater number of people with stroke related impairments and thus highlighting the importance of efficient stroke rehabilitation treatments [53] [55].

Stroke occurrences are influenced by multiple other factors such as age, gender, ethnicity, hereditary characteristics and socioeconomic status which will be detailed in a further section.

	2010		Change from 1990-2010		
	Number of events	Rate per 100 000 person-years	Change in number of events	Change in rate in HICs	Change in rate in LMICs
<b>All stroke</b>					
Incidence	16 894 536	258	68% increase	12% decrease	12% increase
Prevalence	33 024 958	502	84% increase	..	..
DALYs lost	102 232 304	1554	12% increase	..	..
Deaths	5 874 182	88	26% increase	37% decrease	20% decrease
<b>Ischemic stroke</b>					
Incidence	11 569 538	176	37% increase	13% decrease	6% increase
DALYs lost	39 389 408	598	18% increase	34% decrease	16% decrease
Deaths	2 835 419	42	21% increase	37% decrease	14% decrease
<b>Hemorrhagic stroke</b>					
Incidence	5 324 997	82	47% increase	8% decrease	22% increase
DALYs lost	62 842 896	956	14% increase	39% decrease	25% decrease
Deaths	3 038 763	46	20% increase	38% decrease	23% decrease

Table 2.1: Age-adjusted annual incidence and mortality rates, prevalence, and DALYs lost for all stroke, ischemic stroke, and hemorrhagic stroke (HIC = high-income country; LMIC = low-income and middle-income country; DALY = disability-adjusted life-year), adapted from [55]

### 2.1.2 Pathophysiology of Stroke

As illustrated on Figure 2.1, strokes can be divided in two categories depending on the impact produced by the stroke. Approximately 80-85% of strokes are ischemic infarction (IS), characterized by blood hypoperfusion leading to cell death and tissue integrity loss whereas in hemorrhagic strokes (HS) (10-15%), primary hemorrhages derive from hematoma formation and secondary injury, and result in edema and cellular death [56].

More precisely, ischemic occlusions cause brain thrombosis and embolism which both result in decreased blood supply to part of the brain. In thrombosis, the narrowing of blood vessels due to atherosclerosis<sup>1</sup> affects the blood flow. Plaque accumulation eventually causes the vascular chamber to narrow and clot, leading to thrombotic stroke. In embolic stroke, reduced blood supply to the brain results in an embolism which results in acute stress and premature cell death (necrosis). Necrosis is followed by disruption of the plasma membrane, organelle swelling, leaking of cellular contents into extracellular space and loss of neuronal function [53].

Hemorrhagic strokes account for a small percentage (10-15%) of all strokes but present a significant mortality rate. This second type of stroke is characterized by the rupture of blood vessels due to internal damage and increased stress on the brain tissues. The heme degradation is the cause of cytotoxic effects in the vascular system resulting in infarction. Hemorrhagic strokes can further be divided into intracerebral hemorrhage

<sup>1</sup>Atherosclerosis is the buildup of fats, cholesterol and other substances in and on the artery walls into a plaque causing the arteries to narrow, blocking blood flow. The plaque can also burst, transforming into a blood clot [57].

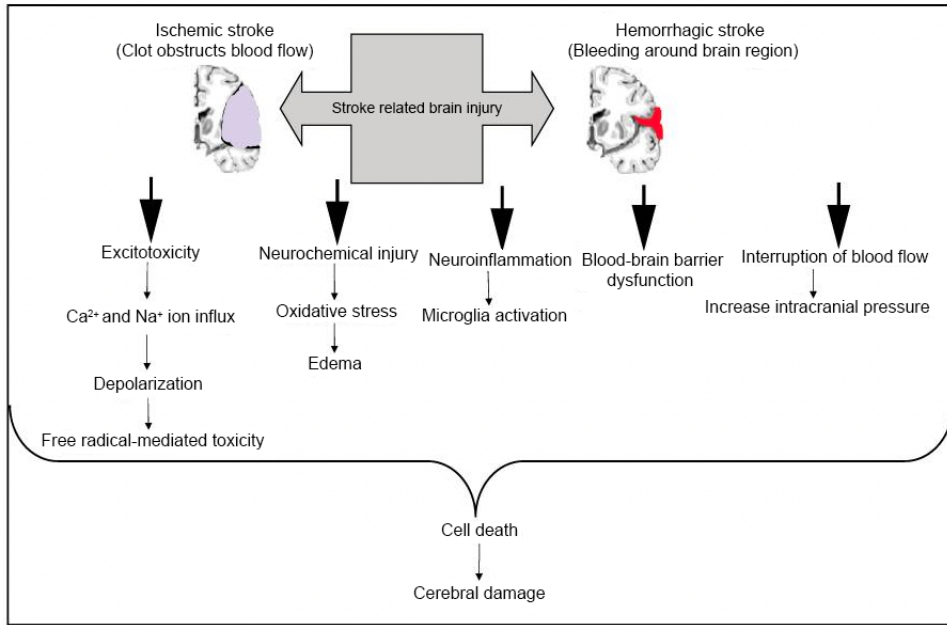


Figure 2.1: Molecular mechanisms of ischemic and hemorrhagic stroke, adapted from [53]

(ICH) in which blood vessels burst resulting in abnormal blood buildup inside the brain, and subarachnoid hemorrhage in which a head injury or a cerebral aneurysm<sup>2</sup> provokes blood accumulation in the subarachnoid space of the brain [53].

It must be noted that stroke is distinguished from transient ischaemic attack (TIA) if the symptoms persist longer than 24 hours. A TIA thus defines a focal dysfunction of less than 24 hours duration and for which the infarction cannot be correctly identified using medical imaging [55].

### 2.1.3 Diagnosis of Stroke

Stroke symptoms generally start suddenly, over seconds to minutes, and in most cases do not progress further. The symptoms depend on the area of the brain affected and are typically characterized by unilateral weakness, numbness, visual loss and altered speech. The diagnosis of stroke can be carried out using clinical tests such as the Face Arm and Speech Test (FAST) [59] and the Recognition of Stroke in the Emergency Room (ROSIER) score [60], and through the use of medical imaging techniques such as CT imaging and DW-MRI. CT scans show a high sensitivity to detect intracranial hemorrhage but, if the ischemic infarct is small or recent, the detection of ischemic stroke may become arduous. DW-MRI, on the other hands, allows the near-perfect detection of ischemic stroke and TIA. Moreover, gradient-echo T2-weighted susceptibility MRI can be used to identify hemorrhagic stroke with a precision similar to CT [55].

<sup>2</sup>A cerebral or intracranial aneurysm is an abnormal focal dilation of an artery in the brain that results from a weakening of the inner muscular layer (the intima) of a blood vessel wall [58].

## 2.1.4 Risk Factors of Stroke

Numerous factors influence the occurrence of stroke. These factors can be classified as non-modifiable and modifiable risk factors as shown on Figures 2.2 and 2.3.

### Non-Modifiable Risk Factors

Non-modifiable risk factors are visible on Figure 2.2 and include age, sex, ethnicity, TIA and hereditary characteristics. According to recent studies, the average age of stroke occurrence in the US is around 65 years and it has been shown that the stroke risk in adults between the ages of 20 and 54 is rising [56]. Moreover, sex influence on stroke occurrence depends on the patient's age as the influence of sex on stroke risk and outcome changes across the patient's lifespan. Indeed, until early adulthood, females show a lower incidence of stroke as well as better functional outcomes as compared to males. However, as female experience menopause, stroke rates begin to increase in females. Stroke rates after middle age are comparable between men and women, and elderly women can even present higher stroke incidence than elderly men after the age of 85 [54]. Patients having already experienced TIA are at greater risk of stroke incidence. As TIA can be assimilated to a sort of "mini stroke", it acts as a warning signal for the risk of an upcoming stroke. Both modifiable and non-modifiable stroke risk factors are influenced by genetics. Although a variety of genetic processes can raise the risk of stroke, genetic risk is proportionate to an individual's age, sex, and race. More specifically, a family history of stroke, rare single gene mutations (e.g. cerebral autosomal dominant arteriopathy and sickle cell anemia) and common genetic variants (e.g. genetic polymorphism in 9p21) are all associated with an increased risk of stroke incidence [53, 55].

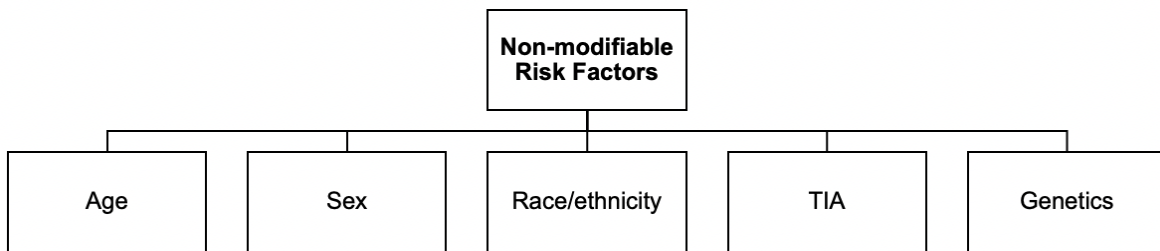


Figure 2.2: Non-modifiable risk factors associated with stroke

### Modifiable Risk Factors

Since a change in lifestyle habits and appropriate medical intervention can effectively reduce the risk of stroke, modifiable risk factors are of the upmost importance for the prevention of stroke. Modifiable risk factors are shown on Figure 2.3 and comprise hypertension, smoking, alcohol and drug abuse, lack of physical exercise, diabetes, cholesterol, diet management and genetics. A history of hypertension and a high blood pressure is one of the major risk factors for stroke as it accounts for 35 to 50% of stroke risk. Fortunately, recent medical intervention to reduce hypertension and blood pressure has been shown to reduce the risk of stroke by approximately 40% [61, 62].

Diabetes is another important risk factor as it increases the risk of stroke by 2 to 3 times and worsens the prospects of recovery after stroke. However, blood sugar level regulation has not been shown to reduce stroke risk [63]. Atrial fibrillation can increase the risk of stroke by 2 to 5 times depending on the individual's age and results in more substantial disability [64]. Hyperlipidemia, characterized by high cholesterol levels, has been inconsistently associated with stroke but the presence of other lipids, such as high-density lipoprotein (HDL), have been shown to decrease stroke incidence and mortality. The influence of hyperlipidemia on stroke incidence is thus not straightforward to interpret as it depends on the lipid profile of the individual [65]. Stroke risk is decreased when alcohol consumption is low to moderate (2 standard drinks per day for males and 1 for females), however it is increased when intake is excessive [66]. All subtypes of stroke are associated with an increased risk of incidence following the regular consumption of illegal substances such as cocaine, heroin, phencyclidine (PCP), lysergic acid diethylamide (LSD), cannabis/marijuana and amphetamines [67]. Tobacco smoking is directly associated with a higher risk of stroke, the average smoker has a twofold increased risk of having a stroke in comparison to non-smokers. Stopping smoking lowers an individual's relative risk of stroke [68]. Finally, poor nutrition and insufficient physical activity are linked to an increased risk of stroke. Indeed, lack of exercise is linked to other health issues which are themselves related to high stroke incidence. Poor diet, on the other hand, impacts hypertension, hyperlipidemia and diabetes which are all contributing risk factors of stroke [69].

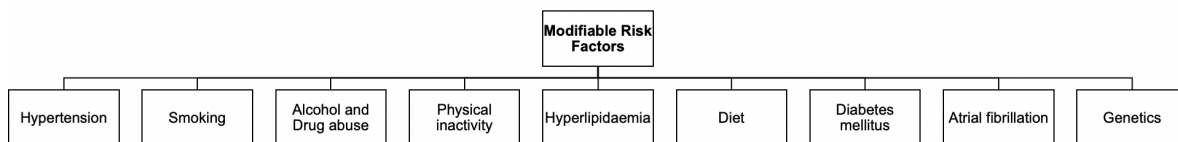


Figure 2.3: Modifiable risk factors associated with stroke

### 2.1.5 Prevention and Treatment Strategies for Stroke

Stroke prevention can be achieved by mitigating the multiple risk factors described in the previous section. In spite of extensive research over the past decades, no simple means of treating or preventing all the clinical causes of stroke has been established. However, many stroke therapy strategies, regrouped on Figure 2.4, have been developed in the aim of managing stroke incidence.

Reperfusion strategies include intravenous thrombolytics (IVT), intra-arterial thrombolysis (IAT) and the use of fibrinogen-depleting agents. IVT and IAT treatments rely on the use of drugs (e.g. recombinant tissue plasminogen activator) to promote fibrinolysis formation, which catalyzes the dissolution of the clot blocking the cerebral vessel. IVT and IAT treatments are, however, most effective in the first hours of the stroke onset. Recent research have found that high fibrinogen levels is related to higher stroke incidence and poorer clinical outcomes. The reduction of blood thickness, the removal of the blood clot and the restoration of blood flow can be achieved through the

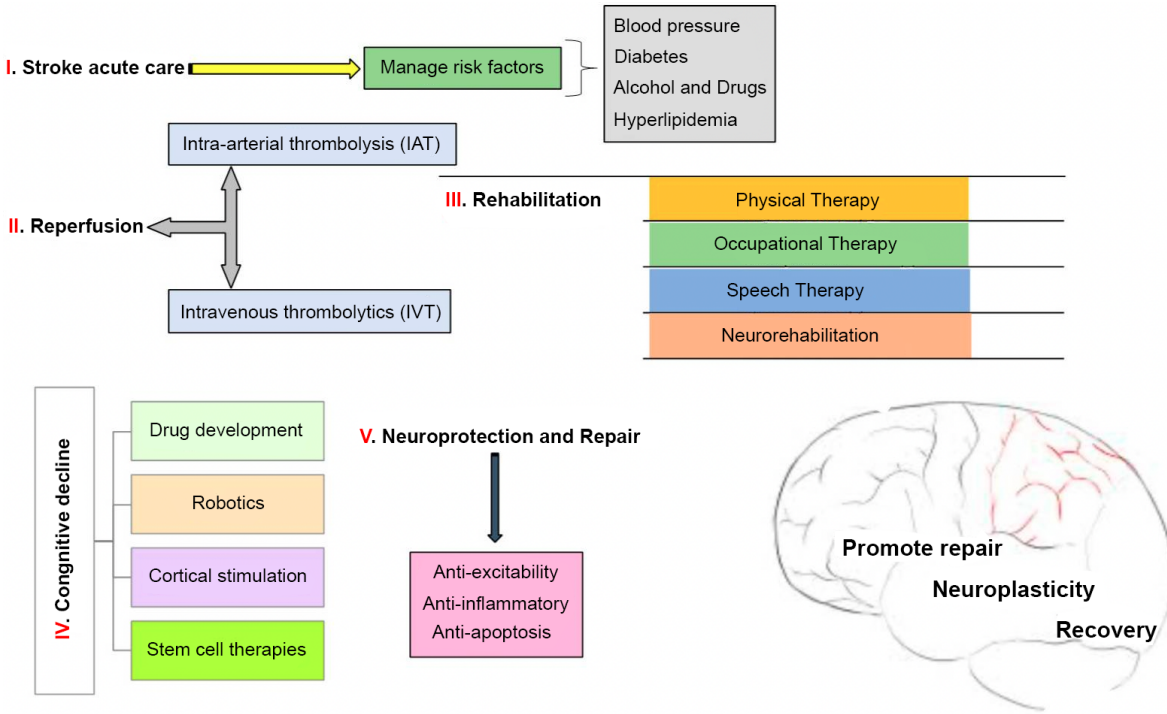


Figure 2.4: Stroke therapy strategies, adapted from [53]

use of fibrinogen-depleting agents [53].

Other stroke management strategies are antihypertensive therapy which aims at reducing hypertension, glucose blood level management, antiplatelet therapy, stem cell therapy, neural repair and rehabilitation. As this Master's thesis focuses on the efficacy of a specific stroke rehabilitation treatment (HABIT-ILE), only the rehabilitation strategy is further developed in more details. Stroke rehabilitation aims at tackling the short- and long-term disabilities and handicaps resulting from stroke. The adequate recovery strategy should be determined in accordance with the phase of the stroke which can be acute (about 2 weeks after the onset of the lesion), subacute (up to 6 months after onset) and chronic (months to years after stroke). The strategy determination process usually comprises the following cyclic steps [70]:

1. Assessment: identification and quantification of the patient's needs;
2. Goal setting: definition of realistic and attainable goals for improvement;
3. Intervention: assistance in the achievement of goals;
4. Reassessment: progress assessment;

Stroke can cause sensorimotor, visual, cognitive and motor impairments, the latter being the most widely recognized. Rehabilitation thus aims at recovering problem-solving skills, accessing social and psychological support, improving mobility and achieving independent living. Motor impairment rehabilitation usually takes the form of task-specific and context-specific training to assist in the complex and heterogeneous recovery

process (see Figure 2.5) of each individual. Recent studies show that rehabilitation should begin as soon as possible after stroke, that patient's training should be ideally given in the patient's own environment and that positive rehabilitation outcome seem to be strongly correlated with patient's motivation and engagement. The duration of the recovery process can vary from several months to years as it is very patient specific [53, 70].

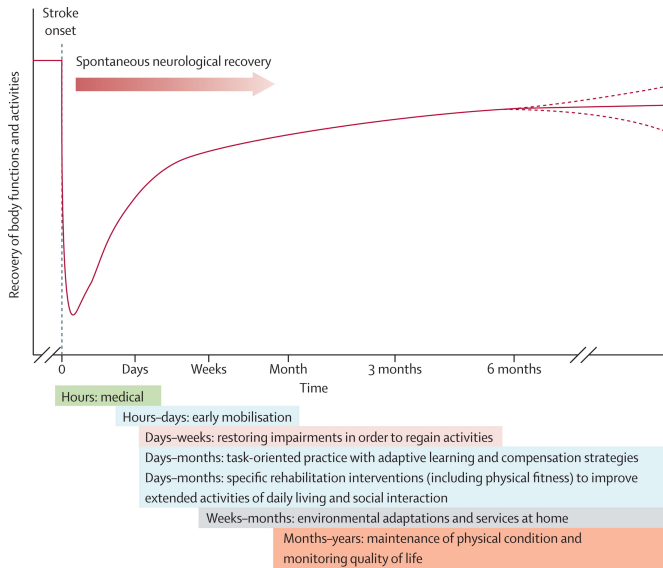


Figure 2.5: Hypothetical pattern of recovery after stroke [70]

Multiple training strategies such as bilateral training, constraint-induced movement therapy at modified doses, electrical stimulation, high-intensity therapy, repetitive task training, robotics and splinting have been used to improve motor function. The rehabilitation technique followed by the patients studied in this work is the Hand and Arm Bimanual Intensive Therapy Including Lower Extremities (HABIT-ILE) method. The HABIT-ILE method was developed in 2011 by Pr. Yannick Bleyenheuft from UCLouvain, in collaboration with Columbia university, and was initially designed for assisting the motor recovery of young infants. The main objective of this method is to improve patients' independence in their daily life by enhancing the physical capacity of both upper (UE) and lower (LE) body extremities. More precisely, the HABIT-ILE method is based on intensive practice of bimanual functional tasks to improve UE function and a simultaneously LE stimulation to improve LE function and UE-LE coordination. HABIT-ILE has already been reviewed in studies involving children from 1 to 6 years with unilateral spastic cerebral palsy (USCP) and has shown positive functional improvements [71, 72, 73].

The task performed in the HABIT-ILE method are described as structured bimanual tasks with increasing motor difficulty combined with a systematical engagement of the trunk and LE postural control. For example, UE bimanual tasks and activities include gross dexterity, manipulative games and tasks, functional tasks, arts and crafts,

virtual reality, and coupled LE postural stimulation examples are ball sitting, standing, balance board standing, virtual reality, walking/running, jumping and cycling [72, 73].

## 2.2 Stroke induced microstructural changes

As stated here above, diffusion MRI has, since the 1990's, played an essential role in the diagnosis, prognosis and management of stroke. dMRI sequences allow the characterization of water molecules motion and are thus used to accurately identify stroke infarcts. The identification process is carried out by analyzing Apparent Diffusion Coefficient (ADC) maps since ADC decrease indicates the presence of an infarct. The fast acquisition and the good interpretability of the DWI maps are key advantages in defining the adequate stroke management strategy. Moreover, as stroke can directly impact the integrity of WM tracts, DTI and microstructural models metrics (see Section 1.3) are used as biomarkers in the assessment of the degree of tissue impairment after stroke. Longitudinal stroke studies are based on the analysis of these metrics to infer on post-stroke degeneration and regeneration processes in WM brain regions. Since motor impairments are the most broadly recognized consequence of stroke, the vast majority of dMRI stroke studies focus on the analysis of the corticospinal tract integrity as it is the major pathway for carrying movement-related information from the brain to the spinal cord [1, 74].

### 2.2.1 Corticospinal Tract

The corticospinal tract (CST) is a collection of neuronal axons that carry movement-related information from the cerebral cortex to the spinal cord. It forms a major neuronal pathway providing voluntary motor output to control the body's musculature via motor neurons (see Figure 2.6). More precisely, the corticospinal fibers are axons from upper motor neurons from the frontoparietal cortices. More than half of these axons originate from the primary motor cortex (primary motor cortex neurons are called Betz cells) with additional contributions from the premotor cortex, supplementary motor cortex and the somatosensory cortex. The tract descends from the cortex through the deep white matter of the cerebrum. The CST bundles then travel between the caudate nucleus and putamen of the basal nuclei, called the internal capsule, into the cerebral peduncles, followed by the brainstem. Upon reaching the pons, the bundles increasingly condense as they descend into the medulla. At this point, 75 to 90% of the fibers will decussate to the contralateral side through the pyramidal decussation and form the lateral corticospinal tract. The rest of the fibers constitute the anterior corticospinal tract. This large proportion of decussating fibers indicate that muscles on the left and right side of the body are, for the most part, controlled by the right and left motor cortex of the cerebrum respectively. After leaving the brainstem, the fibers enter the spinal cord where they synapse with lower motor neurons and interneurons allowing the conscious and voluntary movements of muscles. The lateral corticospinal tract primarily controls the movement of muscles of the limbs whereas the anterior corticospinal tract is involved with movement of the muscles of the trunk, neck and shoulders. As

the CST controls afferent inputs, spinal reflexes and motor neuron activity, damage to this tract leads to serious motor impairment. The motor homunculus visible on Figure 2.7, indicates the affected contralateral body part depending on the location of the CST lesion [75, 76, 77].

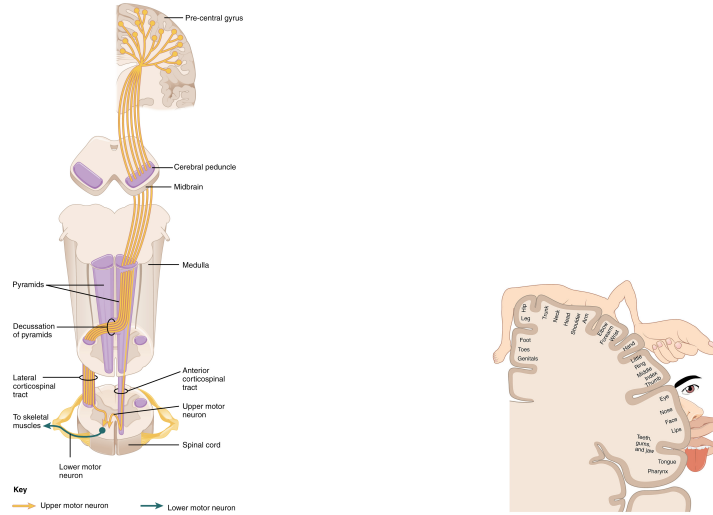


Figure 2.6: Corticospinal tract [75] Figure 2.7: Motor homunculus [77]

Knowledge related to the integrity of the corticospinal tract is thus crucial to infer on the recovery of the impacted motor function. In the case of acute ischemic stroke, studies have shown that the extent of the CST involved in the lesion directly impacts the severity and the scope of motor impairment. Therefore, the visual and microstructural analysis of the CST using tractography (see Figure 2.8) and dMRI techniques are used to assess lesion damage and recovery [76, 77].

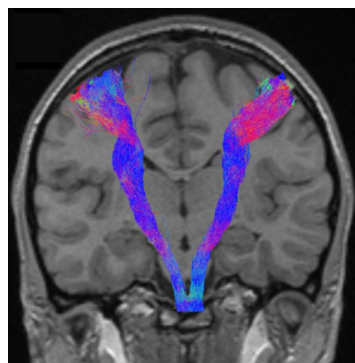


Figure 2.8: Corticospinal tract fibers isolated using tractography [77]

## 2.2.2 Corpus Callosum

The Corpus Callosum (CC) is an essential element of the functional and structural integrity of the brain WM. This large white matter structure illustrated on Figure 2.9

contains tracts connecting both hemispheres of the brain. The CC can subsequently be divided into four parts: the rostrum connecting the orbital surfaces of the frontal lobes, genu connecting the medial and lateral surfaces of the frontal lobes, body or trunk connecting the surface of the hemispheres and splenium connecting the two occipital lobes [78]. As the CC contains interhemispheric motor fibers coordinating both gross and fine motor functions, the microstructural integrity of the CC can be used to gain further insight on the assessment of motor outcome after stroke [79, 80].

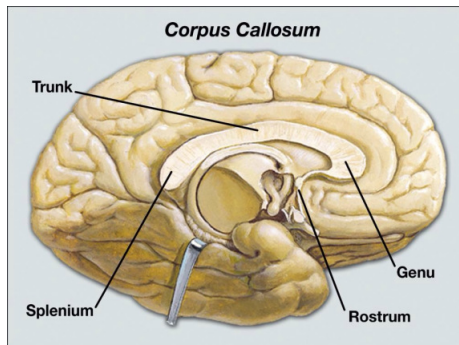


Figure 2.9: Corpus Callosum anatomy [79]

### 2.2.3 Cerebellar Peduncles

The cerebellum (see Figure 2.10) has several functions related to movement and coordination such as balance, movement coordination, vision and motor learning [81]. The WM afferent and efferent tracts of the cerebellum are contained within the corticoponto cerebellar pathway and the superior, inferior and middle cerebellar peduncles [82]. Since important WM pathways such as the fronto-cerebellar loops and the corticoreticulospinal pathway (CRP) have bilateral spinal outputs, assessment of the cerebellar peduncles integrity can be used to infer on motor recovery after stroke [80].

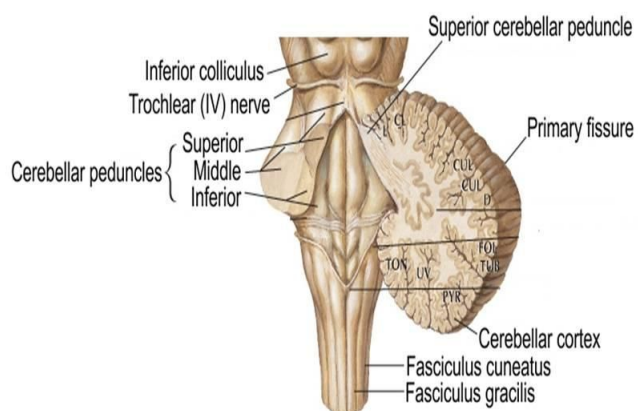


Figure 2.10: Cerebellum and Cerebellar Peduncles anatomy [81]

## 2.2.4 Superior Longitudinal Fasciculus

The Superior Longitudinal Fasciculus (SLF) (see Figure 2.11) is a long myelinated bilateral associative tract extending from the anterior to the posterior regions of the cortex and connecting the frontal, occipital, parietal and temporal lobes. This large tract is present in both hemispheres and can be separated into three distinct components: SLF I, SLF II, and SLF III. As the SLF I WM structure extends to the dorsal premotor and dorsolateral prefrontal regions, it is involved in regulating motor behavior. More precisely, it regulates conditional associative tasks involving competing motor tasks based on conditional rules. Studying the evolution of the SLF I WM integrity can thus give relevant information regarding motor recovery and its correlation with behavioral analysis [80, 83, 84].

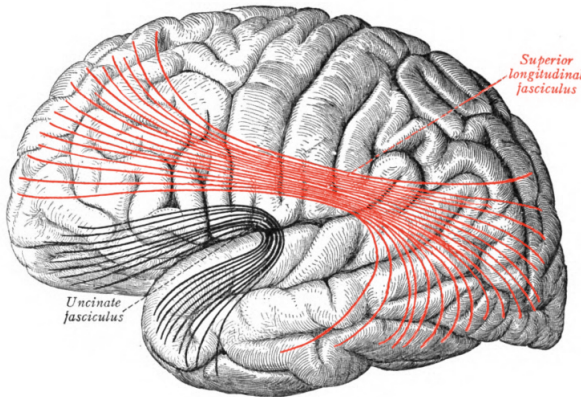


Figure 2.11: Superior Longitudinal Fasciculus anatomy

## 2.2.5 DW-MRI in Stroke studies

As previously mentioned, dMRI methods have been extensively used in the framework of longitudinal stroke studies. This section gives an overview of previous studies that investigated the correlation between dMRI metrics and post-stroke motor outcomes.

Stroke studies present different types of analysis to infer on brain white matter integrity. Whole-brain analysis are used to characterize the global WM changes without previously defining regions of interest (ROIs). This method allows the investigation of all voxels in the brain and, thus, the identification of the most impacted regions without previous spatial knowledge of the expected results. Whole-brain analysis can be conducted through histogram analysis of the metric values of voxels in the whole brain or by using the voxel-based analysis (VBA) approach, which compares the metric values in every voxel of the brain. Another method relies on the definition of ROIs and provides region-specific analysis. ROIs can be manually delineated or semi-automatically defined using registration. The use of ROI and lesion masks to perform dMRI data analysis produces finer results and allows the comparison between specific anatomical regions of the brain. Finally, tractography is also a widely used technique for the

investigation of WM tract integrity. As discussed in Section 1.2.3, deterministic and probabilistic reconstruction models allow the extraction of WM pathways in the brain, along which dMRI metrics can be analyzed. Using tractography, tract-based ROIs can also be defined and brain region connectivity analysis can be conducted to infer on the brain neuroplasticity, among other things [1].

### dMRI metrics as biomarkers

The DTI model metrics are the most widely used biomarkers for the assessment of WM tract integrity and many studies only focus on the extraction of FA values in the CST. dMRI metric values are, in the vast majority of cases, averaged across the defined ROIs which are usually defined as the part of or the whole corticospinal tract. Metric values are then usually reported as average measures from the ipsilesional or contralateral side, or as a ratio comparing both sides. The statistical significance of the correlation between dMRI metrics and motor impairment recovery varies across studies as it depends on the diffusion models used, the considered ROIs, the post-stroke phase of the patients and the research methodologies.

Although data collection and processing methods vary from one study to another, literature review of the use of DTI metrics for stroke analysis show a high degree of significance as WM integrity biomarkers. Lindenberg et al. [85] examined the correlation between FA measures from the whole corticospinal tract of 15 chronic stroke patients and the motor outcome of an experimental neurorehabilitation method. The ipsilesional side of the CST showed significantly decreased FA values and increased directional diffusivities as compared to control subjects. Subsequent increased FA values and lower directional diffusivities on the ipsilesional side following neurorehabilitation were associated with improved motor function. This study, similarly to the work of Rüber et al. [86] and of Koyama et al. [87], demonstrated that FA metric analysis in the CST can be used to predict motor outcome and to infer on the recovery potential of a neurorehabilitative method. On the other hand, Grotts et al. [88] investigated the prognostic value of FA in the corticospinal tract on motor outcome of the upper limb and did not find significant correlation between FA and motor outcomes at some post-stroke phases.

Other studies analyzed the structural integrity of the CST by measuring DTI metrics in specific ROIs such as the posterior limb of the internal capsule (PLIC) or the cerebral peduncle (CP). Jayaram et al. [89] reviewed the importance of the structural and functional integrity of the CST in determining upper limb post-stroke recovery by measuring the asymmetry in FA in the PLIC. Their results indicated that highly asymmetrical FA values, reflecting reduced microstructural integrity on the ipsilesional side, were associated with greater walking impairment. Park et al. [90] investigated the possibility of using a standardized CST template to assess FA correlation with CST integrity. They found out that the use of a template CST and tract-based ROIs in the PLIC produced similar results for the prediction of motor outcome. These results highlight the fact that registered CST templates can be used to assess the CST integrity

with a similar precision than patient's own CST thus greatly facilitating CST integrity analysis. Song et al. [91] performed a longitudinal study of the correlation between DTI measures (MD, AD, RD and FA) in the ipsilesional and contralesional PLIC, and patients' motor recovery. Their findings also indicated that higher FA measures and lower diffusivities in the ipsilesional PLIC are significantly correlated with increased upper-limb motor outcome. Hannanu et al. [80] produced an extensive study of the WM disruption in subacute stroke through the measurement of FA in 33 WM regions in order to investigate the potential source of ipsilateral hand impairment (ILH). The use of numerous ROIs allowed the identification of multiple brain WM regions affected by stroke induced microstructural changes. Their findings indicate that the corticospinal tract (CST), the genu body and splenium of the corpus callosum (CC) and the contralesional anterior corona radiata (ATR) were associated with ILH impairment, thus highlighting the importance of the use of multiple ROIs.

To summarize, DTI metrics and, more specifically, FA have been extensively used in the framework of stroke studies. Indeed, the vast majority of stroke studies investigate patients' motor outcomes based on the FA values extracted from the whole or part of the ipsilesional and contralesional CST. Although few studies do not report correlations between FA values and motor impairment recovery, FA seems to be a consistent, but quite non-specific, measure of white matter integrity. The other DTI metrics are, however, only measured in a minority of studies even though they allow a better understanding of the underlying white matter integrity. Indeed, AD allows the characterization of axonal damage and RD is related to the degree of myelination. Results across studies show consistent trends: decreased FA and increased diffusivities are observed on the ipsilesional side of the CST after stroke; mainly due to white matter degeneration. Furthermore, higher FA values and decreased diffusivities on the ipsilesional side have been shown to be related to motor recovery, thus confirming the usefulness of DTI in stroke therapeutic strategies.

### Going further

As mentioned in Section 1.2.2, even though the tensor model (DTI) allows for microstructural integrity characterization of WM, some major limitations remain. Indeed, the interpretation of the DTI metrics in case of multiple crossing fiber populations or complex fiber architecture (crossing, kissing and fanning fibers) becomes unclear. In other words, while DTI metrics are useful to infer on tissue integrity in well aligned WM regions, they should be interpreted with caution in other regions. More advanced techniques have thus been developed to better interpret the changes in WM structural properties after stroke [1, 2, 74].

In order to overcome these limitations, Alves et al. [74] and Wei et al. [92] used DTI as well as Diffusion Kurtosis Imaging (DKI) to extract diffusion and kurtosis parameters of impaired WM tracts after stroke. DKI is an extension of the DTI model as it is able to correctly quantify the non-Gaussian distribution of water molecules, thus yielding more accurate evaluation of the WM integrity. These studies indicated that

DKI presents enhanced sensitivity to detect microstructural changes as compared to DTI but this model still presents limited specificity. Furthermore, Alves et al. [74] developed a novel technique, called Correlation Tensor MRI (CTI), which allows to mitigate the specificity limitations of DKI and DTI.

Other studies relied on the use of multi-compartment models to improve the analysis of the WM microarchitecture. Models such as NODDI give access to other aspects of the microstructural integrity such as axonal and neurite density, and the fiber orientation dispersion index (ODI). Adluru et al. [93] used the NODDI multi-compartment model to compare ROIs comprising the stroke lesion with the symmetrical region in the contralateral hemisphere. Their findings indicated that the stroke lesion presented an increased ODI as well as clear changes in the intracellular and free water diffusivity compartments. The results of this study correspond with the results obtained by Wang et al. [94] and Hui et al. [95] who also concluded that NODDI allows a more sensitive and efficient evaluation of microstructural changes in brain tissues after stroke as compared to DTI and DKI.

On the other hand, recent studies decided to investigate the structural brain connectivity by including microstructural information in the process of tractography. The additional microstructural information allows for better estimates of the orientation distribution of fibers in voxels, of the absolute fiber count between two areas of interest and of the white matter integrity along the tracts. Koch et al. [96], reported that tractography is increasingly used to analyze the brain connectivity after stroke and that intra- and interhemispheric circuits between primary and secondary motor and non-motor areas at the cortical level have significantly extended the concept of interacting networks for recovery processes after motor stroke. The use of tractography coupled with the use of noninvasive stimulation techniques such as Transcranial Magnetic Stimulation (TMS) allows for novel insight on brain connectivity and plasticity after stroke. Furthermore, recent studies performed whole-brain structural and functional connectivity analysis allowing for complete assessment of the plasticity patterns of neural networks interactions. Guggisberg et al. [2] performed an impressive study of the principles of network plasticity after stroke based on the analysis of the brain structural and functional connectivity using TMS and functional MRI (fMRI) (for more details on the combined use of fMRI and DTI, see the work of Frizell et al. [97]). They concluded that the identification of brain networks in patients after stroke show promising results for the understanding of the consequences of stroke, its impact on recovery as well as for the elaboration of rehabilitation strategies. In that regard, Koch et al. [98] investigated the possibility of the future development of patient-specific neurorehabilitative treatments. More precisely, they developed whole-brain connectomes using tractography and assessed the key parameters in predicting natural motor recovery after stroke using a Support Vector Machine (SVM) classifiers approach. They reported that this approach allowed the individual prediction of natural recovery up to 2 weeks after stroke onset by means of the identification of the key underlying neuronal network parameters.

Table 2.2 regroups the multiple studies discussed here above and details the specific ROIs and metrics used as well as the reported outcomes.

Study	Patients	Technique	Software/ Metrics	ROIs	Outcome
Lindenberg et al. [85]	15 chronic stroke patients	DTI Tractography	FA	CST	Correlation between metrics and motor outcome
Rüber et al. [86]	18 stroke patients 10 control subjects	DTI	FA	CST PT	Correlation between metrics and motor outcome
Koyama et al. [87]	16 acute stroke patients	DTI TBSS	FA	CST	Correlation between metrics and motor outcome
Groisser et al. [88]	10 acute stroke patients	DTI	FA, AD, RD	CST	No correlation between metrics and motor outcome
Jayaram et al. [89]	9 chronic stroke patients	DTI TMS	FA	CST PLIC	Correlation between metrics and motor outcome
Park et al. [90]	21 stroke patients 23 control subjects	DTI	FA	CST PLIC	Correlation between metrics and motor outcome
Song et al. [91]	13 chronic stroke patients	DTI	FA, AD, MD, RD	PLIC	Correlation between metrics and motor outcome
Hannanu et al. [80]	21 subacute stroke patients	DTI	FA	33 WM regions	Correlation between metrics and motor outcome
Alves et al. [74]	Simulations	DTI DKI CTI	FA, MD DKI metrics	WM and GM regions	Correlation between metrics and motor outcome
Wei et al. [92]	60 stroke patients	DTI DKI TBSS	FA, AD, MD, RD DKI metrics	81 WM regions	Correlation between metrics and motor outcome
Adluru et al. [93]	2 stroke patients	DTI HARDI NODDI	FA, MD NODDI metrics	Stroke lesion site	Correlation between metrics and motor outcome
Wang et al. [94]	71 hyperacute/acute/subacute ischemic stroke patients	DTI DKI NODDI	FA DKI metrics NODDI metrics	Stroke lesion site	Correlation between metrics and motor outcome
Hui et al. [95]	44 acute/subacute ischemic stroke patients	DKI NODDI	DKI metrics NODDI metrics	Stroke lesion site	Correlation between metrics and motor outcome
Guggisberg et al. [2]	Literature review	DTI HARDI NODDI fMRI TMS	Literature review	Literature review	Literature review
Friznell et al. [97]	12 subjects	DTI fMRI	DTI metrics	Whole-brain connetomes	Neural networks assessment
Koch et al. [98]	92 stroke patients	Tractography SVM	DTI metrics	Whole-brain connetomes	Neural networks assessment

Table 2.2: Summary of the literature articles reviewed. DTI = Diffusion Tensor Imaging; TBSS = Tract-Based Spatial Statistics; TMS = Transcranial Magnetic Stimulation; DKI = Diffusion Kurtosis Imaging; CTI = Correlation Tensor Imaging; HARDI = High Angular Resolution Diffusion Imaging; NODDI = Neurite Orientation Dispersion and Density Imaging; SVM = Support Vector Machine; CST = corticospinal tract; PT = pyramidal tract; PLIC = posterior limb of the internal capsule; WM = white matter

## Challenges

Although the use of dMRI in the framework of stroke study has been rapidly evolving in the past decades, some key challenges still remain. First of all, the heterogeneity of the stroke severity, phase, type and lesion location results in high variance between patients which directly impacts the interpretability of the dMRI results. Indeed, as lesion sizes and locations can alter data registration and processing, the use of lesion masks can become necessary. However, lesion masks are, for the most part, hand-drawn which can be greatly time consuming and advances in automatic lesion segmentation are still to be made. Furthermore, the vast majority of studies only have access to small patient

population sizes. Small sample sizes combined with the heterogeneity of strokes result in a lack of comparability across studies. Secondly, studies present in the literature show great variations of data acquisition, preprocessing, registration and processing methods. The lack of consensus over a standardized approach is a real challenge for the replicability of stroke studies. Thirdly, and as previously mentioned, most of stroke studies do not use higher order mutlicompartment models and focus on the extraction of DTI metrics in the CST. Recent studies presented here above indicate that higher order models, tractography and functional measurement techniques are needed for the correct assessment of the stroke induced impairments on neural networks [1, 2, 74, 80].

# CHAPTER 3

## METHODS

This chapter gives information about data acquisition, the multiple data pre-processing steps used to enhance data quality, data processing and the diffusion metrics computation methodologies.

### 3.1 Data

The data was acquired in the framework of the 2019 call for *Action de Recherche Concertée* (ARC) initiated by the Fédération Wallonie-Bruxelles in Belgium. This program aims at estimating *in vivo* white matter microstructure in motor pathways for the early assessment of motor outcome in patients with brain damage (MICROMOTO), a project proposed by Louvain Bionics. The main goals of this project are the development of a multi-model approach of the microstructures from DW-MRI data, the investigation of links between the brain microstructure and motor skill recovery in subacute stroke and the longitudinal assessment of the microstructure in infants with cerebral palsy (CP) undergoing intensive rehabilitation training.

#### 3.1.1 Subjects

In 2021, a total of 140 eligible adult patients were contacted to participate in this study. Out of these 140 patients, 22 adults were included in the process. Out of these 22 patients, only 15 (12 males and 3 females) with ages ranging from 48 to 80 years old, actually completed the study as 7 patients dropped out. Detailed information about these 15 patients are regrouped in Table 3.1.

As visible on Table 3.1, 80% suffered from ischemic stroke and only 20% from hemorrhagic stroke. Moreover, the lesion location varied from one patient to another with the right and left Sylvian segments being the most impacted. The 15 patients were divided into two randomized populations: the case (8 patients) and control (7 patients) groups. The case group followed the HABIT-ILE (see Section 2.1.5) rehabilitation method in between the first and second data acquisition sessions whereas the control group only followed the HABIT-ILE method after the last data acquisition session (see Figure 3.1).

More precisely, Figure 3.1 indicates that the set of patients underwent a total of 4 acquisition sessions. The reference or baseline acquisition is referenced as T0, the second acquisition, performed three weeks after T0, corresponds to T1, the third acquisition T2 is obtained 12 weeks after T0 and, finally, the fourth acquisition T3 is obtained 16

Code	Age	Sex	Stroke occurrence	Hemiplegia	Lesion type	Lesion location	Group
20.01.01	57	M	06/03/2019	Right	Ischemic	Left Sylvian segment	Case
20.01.02	62	F	31/10/2019	Right	Ischemic	Left Sylvian segment	Control
20.02.01	80	M	01/09/2014	Right	Ischemic	Left Sylvian segment	Case
20.02.02	66	M	18/10/2011	Right	Ischemic	Left Sylvian segment	Control
20.03.01	61	M	08/08/2020	Left	Ischemic	Right internal capsule	Case
20.05.01	52	M	29/10/2019	Right	Ischemic	Left lenticular nucleus	Control
20.05.02	53	M	14/09/2020	Left	Hemorrhagic	Right capsulo-lenticular nucleus	Case
20.06.01	56	M	19/02/2019	Left	Ischemic	Right Sylvian segment	Case
20.06.02	57	F	30/11/2020	Left	Ischemic	Right Sylvian segment	Control
20.07.01	48	M	13/06/2018	Left	Ischemic	Right Sylvian segment	Case
20.08.01	73	F	19/10/2019	Left	Ischemic	Right Sylvian segment	Case
20.08.02	57	M	09/06/2018	Left	Ischemic	Right Sylvian segment	Control
20.10.01	74	M	11/08/2016	Left	Hemorrhagic	Right parietal lobe	Case
20.10.02	62	M	01/11/2016	Left	Hemorrhagic	Right ventricle	Control
20.11.02	68	M	24/01/2019	Right	Ischemic	Left paramedian pontine reticular formation	Control

Table 3.1: Patients information

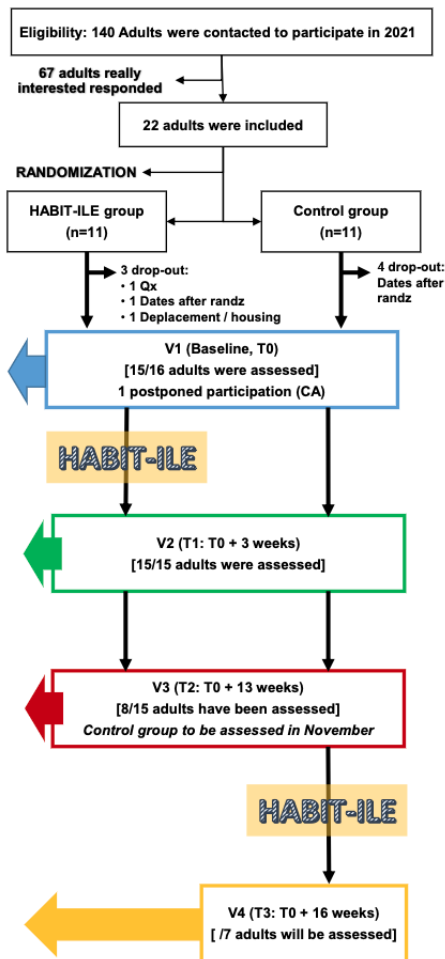


Figure 3.1: Subjects data acquisition flowchart

weeks after T0. As the objective of this study is to assess the efficacy of the HABIT-ILE rehabilitation method but also to equally support patients' recovery, the case or HABIT-ILE group follows the rehabilitation method between T0 and T1 and the control

group follows it between T2 and T3.

### 3.1.2 Data acquisition

During each acquisition session, anatomical and diffusion MR images were collected using a *3T GE SIGNA™ Premier* scanner with a RM-IR (Inversion Recovery) sequence for the anatomical images and a EP-SE sequence for the diffusion MR images. The RM-IR sequence was characterized by a TR of 2.31282 ms, a TE of 0.003516 ms, a slice thickness of 0.8 mm, an imaging frequency of 127.77 Hz and the obtained anatomical images have a  $166 \times 312 \times 312$  resolution and a  $0.8 \times 0.8205 \times 0.8205 \text{ mm}^3$  voxel size. The EP-SE sequence had a TR of 4.837 ms, a TE of 0.0786 ms, a slice thickness of 2 mm, an imaging frequency of 127.77 Hz and the obtained diffusion images have a  $110 \times 110 \times 68$  resolution and a  $0.8 \times 0.8205 \times 0.8205 \text{ mm}^3$  voxel size. The diffusion images are each composed of 170 volumes, 10 volumes acquired with a null b-value and 160 volumes with different b-values:  $700 \text{ s/mm}^2$  (64 volumes),  $2000 \text{ s/mm}^2$  (32 volumes),  $3000 \text{ s/mm}^2$  (32 volumes) and  $5000 \text{ s/mm}^2$  (32 volumes). Anatomical files are composed of a NIfTI (.nii.gz) file containing the measured signal (see Figure 3.2) and a JSON (.json) file regrouping the acquisition sequence parameters.

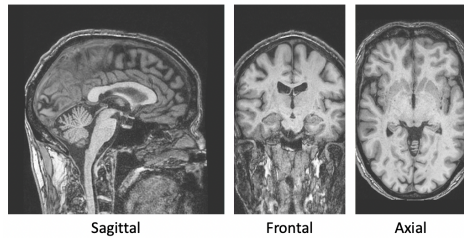


Figure 3.2: Anatomical volume slices of subject 20.03.01 at T1 in the sagittal, frontal and axial views

On the other hand, diffusion files are made up of a NIfTI (.nii.gz) file containing the measured signal (see Figure 3.3), a JSON (.json) file regrouping the acquisition sequence parameters, a text file (.bval) containing the b-values and a text file (.bvec) containing the b-vectors.

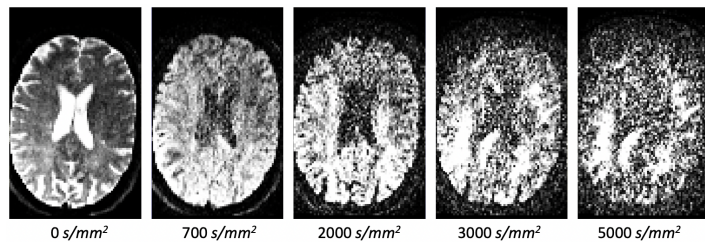


Figure 3.3: Raw diffusion volume slices of subject 20.03.01 at T1 for the different b-values

In addition to the occasional drop out of individuals, several acquisition times are missing for some patients. Moreover, a proportion of the diffusion scans were not

correctly acquired and present missing data resulting in truncated sagittal and frontal views as depicted on Figure 3.4. These acquisitions were thus discarded in order to avoid disrupting data processing.

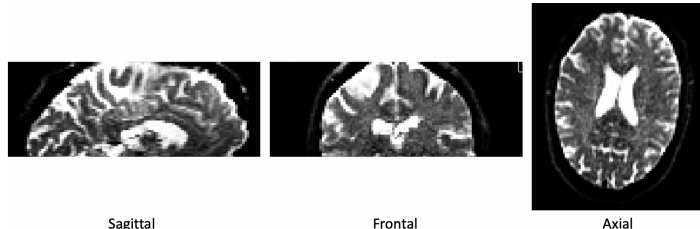


Figure 3.4: Truncated raw diffusion volume slices of subject 20.03.01 at T0

### 3.1.3 Behavioral analysis

In order to gain additional knowledge regarding the effects of the HABIT-ILE rehabilitation method on patients' aptitudes, supplementary physical, cognitive and logical tests were performed after each data acquisition session. The multiple conducted tests and questionnaires are:

- Assisting Hand Assessment for Adults (Ad-AHA): observation based assessment tool to measure the patient's spontaneous use of the stroke affected hand to perform bimanual activities [99].
- Abilhand questionnaire: measurement of the patient's perceived difficulty in performing everyday manual activities [100].
- Activlim questionnaire: Rasch-built scale measuring the perceived difficulty in performing activities without technical or human assistance [101].
- Stroke Impact Scale (SIS) questionnaire: stroke-specific outcome measurement of strength, hand function, activities of daily living, mobility, communication, emotion, memory and thinking based on the self-reported difficulty experienced by the subject [102].
- Modified Rankin Scale (mRS) questionnaire: clinician-reported measure of global disability [103].
- Canadian Occupational Performance Measure (COPM): outcome measure designed for use by occupational therapists to assess patient outcomes in the areas of self-care, productivity and leisure [104].
- Dextrain: the Dextrain Manipulandum and Homecare are tools to promote neuro-rehabilitation, to improve manual dexterity recovery, prediction and prevention, and to contribute to independence in activities of daily living and quality of life [105].
- ReaPlan: end-effector robot, developed by Axinesis, for intensive, auto-adaptative upper limb rehabilitation with inbuilt therapeutic gamification to increase motivation and optimize rehabilitation outcomes [106].
- Fugl-Meyer Assessment-Upper Extremity (FMA-UE): system for evaluation of

motor function, balance, sensation qualities and joint function in hemiplegic patients [107].

- Box and Block test (BBT): fast assessment of the unilateral gross manual dexterity [108].
- Wolf Motor Function Test (WMFT): time-based method to evaluate upper extremity performance while providing insight into joint-specific and total limb movements [109].
- 6 Minutes Walk Test (6MWT): exercise test used to assess aerobic capacity and endurance based on the distance covered over a time of 6 minutes which is used to compare changes in performance capacity [110].
- Stroop test: assessment of the executive function, including working memory, selective attention, and ability to inhibit automatic responses based on the use of a list of words that are printed in a different color than the meaning of the word [111].
- Wechsler Adult Intelligence Scale - 3<sup>rd</sup> edition (WAIS-III: measurement of general intellectual abilities based on four index scores (verbal comprehension, perceptual reasoning, working memory and processing speed) [112].
- Arithmetic (Arith) test.
- Digit Symbol Coding (DSC) test: cognitive test requiring the subject to match symbols to numbers according to a reference key [113].
- Corsi Block-Tapping Task: assessment of visuospatial short-term memory [114].
- Bell test: measurement of visual selective and focused attention, visual perception and visual motor processing speed through the cancellation of targets (bells) among distractors [115].
- Trail Making Test (TMT): assessment of executive function such as letter and number recognition, mental flexibility, visual scanning, and motor function [116].
- Montreal Cognitive Assessment (MoCA): fast paper and pencil test to assess multiple cognitive domains including memory, language, executive functions, visuospatial skills, calculation, abstraction, attention, concentration, and orientation [117].

## 3.2 Data preprocessing

The ElikoPy pipeline detailed in Section 1.4 was used to preprocess the collected data. Using this pipeline allows to enhance the quality of the raw data images and to launch the preprocessing on all the data in a single step using the `preproc` ElikoPy function. The steps performed by this function are explained in Section 1.4.1 and Figure 3.5 shows a side-by-side comparison of the raw data and the preprocessed data.

## 3.3 Data registration

Once the diffusion data is correctly preprocessed for all of patients, the `dti` ElikoPy function is used to compute the fractional anisotropy (FA) maps required to perform

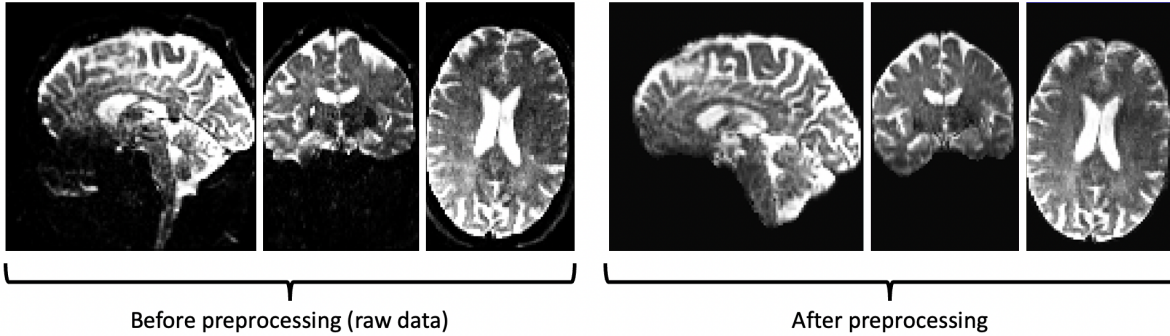


Figure 3.5: Comparison between raw and preprocessed diffusion volume slices of subject 20.03.01 at T1

data registration. Indeed, as the corticospinal tract is the main region of interest in this study, it must be correctly identified and isolated for each patient in order to analyze its microstructural changes. The extraction of the CST volume, as well as the other selected regions of interest (ROIs) for each patient, is achieved through atlas registration. Image registration is the process of transforming different sets of data into a single unified coordinate system, and can be thought of as the task of aligning images so that comparable characteristics can be related easily [118]. In this work, the two sets of data on which the registration was performed were the set of diffusion data for each patient at every acquisition times (T0, T1, T2 and T3), and the sets of standardized atlases registered in the Montreal Neurological Institute (MNI) space.

### 3.3.1 Atlas sets

In order to obtain the most complete registration and, thus, the largest number of regions of interest (ROIs) possible, 6 atlases (the majority of these atlases can be used through FSL and detailed specifications are given on the FSL website [119]) corresponding to a total of 135 brain regions were used. The first atlas used is a probabilistic atlas of the cerebellar peduncles in the space defined by the MNI152 template, created by Diedrichsen et al. [120] and included in the FSL software. The second atlas, also developed by Diedrichsen et al. [120] divides the cerebellum into 21 probabilistic atlases representing the different lobules. The third and fourth atlases are the Harvard-Oxford cortical and subcortical structural atlases [121] which are made up of 61 different regions. These atlases are provided by the Harvard Center for Morphometric Analysis and are also available on FSL. The different lobes of the brain constitute a fifth atlas which is provided by the Research Imaging Center [122] and is also usable through FSL. The last atlas is the XTRACT HCP Probabilistic Tract Atlas created by Warrington et al. [123] and made up of 42 probabilistic WM tracts. Since the XTRACT atlas allows the identification of major WM fiber bundles, a standardized atlas of the corticospinal tract is directly available. The latter will be extensively used in the registration process as well as in the analysis of the dMRI metrics. The XTRACT atlas is also directly available on FSL.

### 3.3.2 Registration process

Concretely, data registration is an iterative multi-step process based on the use of the DiPy registration method [124]. As each patient's brain presents its own microstructural damage and alterations caused by the stroke occurrence, the registration process was conducted from the standardized MNI152 space towards each patient's native space. This allows the determination of regions of interest in the patient's native space which shows better registration outcomes as compared to the standard registration into the MNI152 space.

The registration process relies on the use of the FA diffusion data from the *HCP1065* standard-space DTI templates registered in the MNI152 space [119], patients' FA maps and the atlases described here above. The first step consists in the computation of the deformation field to be applied to the images to be registered. This is achieved by defining the `getTransform` Python function which takes a 3D array of static volume, patients' FA maps in this case, and a 3D array of moving volume corresponding to the *HCP1065* FA template. This function then returns the mapping transform allowing the registration of the moving volume onto the static volume. First, an affine registration (see Figure 3.6) consisting of image translation based on the center of mass of the images, image rotation, image scaling and shearing is performed. The optimization process of the affine registration is based on the maximization of the Mutual Information (MI) of the images which represents the mutual dependence between the images. The affine registration is followed by a diffeomorphic registration (see Figure 3.6) step based on the Symmetric Normalization (SyN) algorithm proposed by Avants et al. [125]. The optimization of the diffeomorphic transformation is based on the Cross-Correlation (CC) metric which is a measure of similarity between the two images.

Once the deformation field is correctly computed, a second Python function named `applyTransform` is used to register the atlas maps in the native space of each patient.

## 3.4 Microstructural analysis

The registration process allows the isolation of the left and right WM fibers of the corticospinal tract which is the spotlight of research in this work. Using directly the ROIs obtained after the registration process is, however, not ideal as some corrections should be made. Indeed, the obtained registered brain regions have to be multiplied by the brain mask of each patient obtained during the preprocessing step. As depicted on Figure 3.7, this masking step avoids registration outside of the brain limits. Furthermore, the obtained registered regions are represented as probabilistic maps which is not ideal for further processing. A threshold is thus applied on these probabilistic maps in order to obtain binary masks of the ROIs as visible on Figure 3.7.

The binary CST mask, illustrated for one patient on Figure 3.8, can then be used to determine the different dMRI metrics and to analyze their longitudinal evolution.

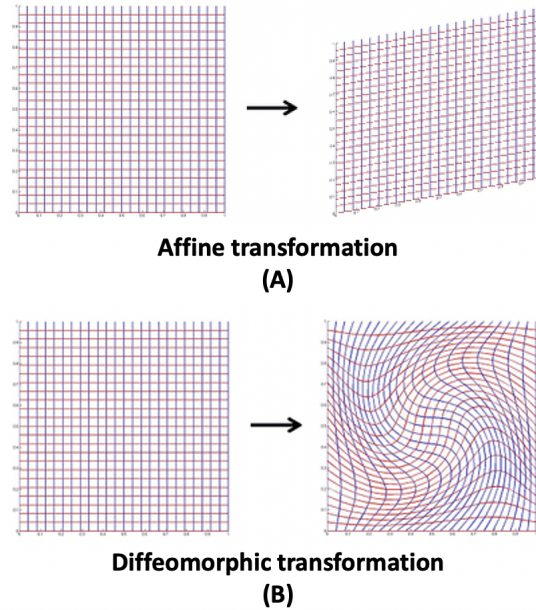


Figure 3.6: Illustration of (A) affine transformations; (B) diffeomorphic transformations, adapted from [126]

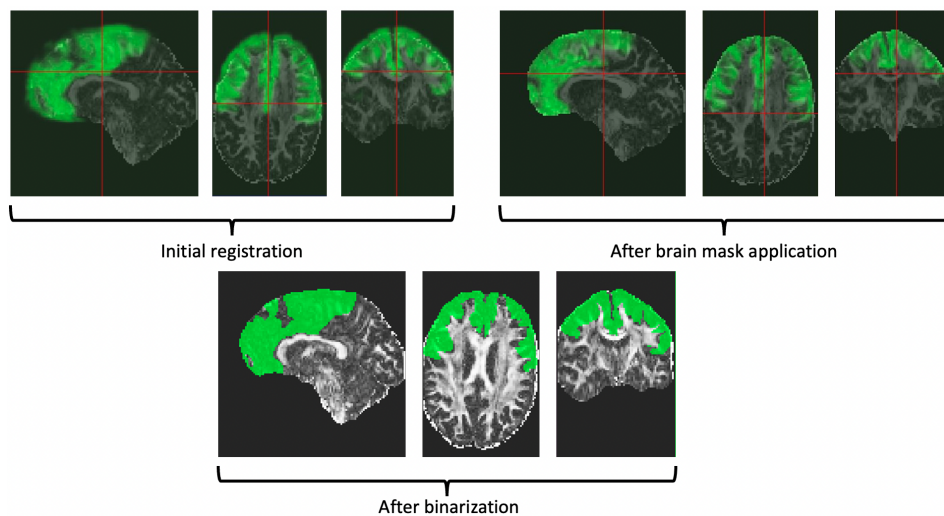


Figure 3.7: Illustration of the registration corrections on the frontal lobe of patient 20.03.01 at T1

Moreover, as the patients in this study present sizable lesions in the right or left brain hemisphere, the metric results will be calculated as mean values from the ipsilesional and contralesional sides, as ratios between the ipsilesional and contralesional hemispheres ( $rM$ ), and as ratios of asymmetry between the ipsilesional and contralesional hemispheres ( $aM$ ):

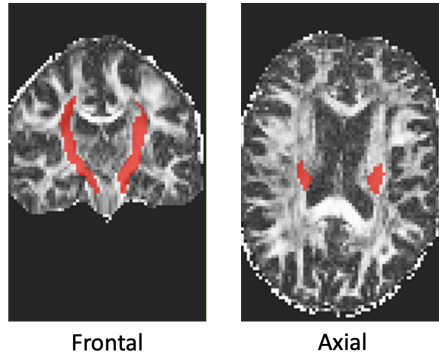


Figure 3.8: Registered corticospinal tract ROI for patient 20.03.01 at T1

$$rM = \frac{M_{ipsilesional}}{M_{contralesional}}, aM = \frac{M_{ipsilesional} - M_{contralesional}}{M_{contralesional} + M_{contralesional}} \quad (3.1)$$

where  $M$  stands for metric.

### 3.4.1 DTI metric maps

As previously mentioned, the Diffusion Tensor Imaging model metrics are directly computed using the `dti_ElikoPy` function. This function outputs different metric maps used to characterize the microstructural integrity of the ROIs:

- MD: Mean Diffusivity map
- AD: Axial Diffusivity map
- RD: Radial Diffusivity map
- FA: Fractional Anisotropy map
- FA RGB: Fractional Anisotropy RGB map

The DTI metric maps are illustrated on Figure 3.9 and detailed information about the interpretation of these metrics is regrouped in Section 1.2.2.

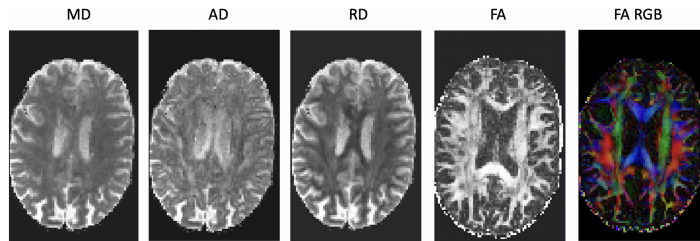


Figure 3.9: Diffusion Tensor Imaging (DTI) metric maps of patient 20.03.01 at T1

### 3.4.2 NODDI metric maps

Computation of the Neurite Orientation Dispersion and Density Imaging (NODDI) model using the `noddi` ElikoPy function outputs the following metric maps:

- `ODI`: Fiber Orientation Dispersion Index map
- `fextra`: Extra cellular volume fraction map
- `fintra`: Intra cellular volume fraction map
- `fiso`: Free water volume fraction map

Figure 3.10 shows the maps of the metrics mentioned here above. Detailed explanation about the NODDI model can be found in Section 1.3.1.

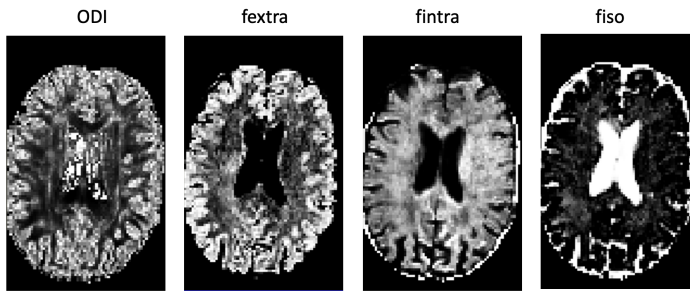


Figure 3.10: NODDI metric maps of patient 20.03.01 at T1

### 3.4.3 DIAMOND metric maps

The ElikoPy pipeline was used to obtain multiple metric maps from the DIistribution of 3D Anisotropic MicrOstructural eNvironments in Diffusion-compartment (DIAMOND) imaging model via the `diamond` ElikoPy function:

- `fractions`: Fraction of volume for each compartment (`frac_f0`: First fiber population; `frac_f1`: Second fiber population; `frac_csf`: CSF compartment)
- `t0`: First fiber population tensors
- `t1`: Second fiber population tensors

The major interest in using the DIAMOND multi-compartment model in this study is the fact that it allows the extraction of the DTI metrics using the output metric maps listed here above. As discussed in Section 1.3.2, the DIAMOND model offers the possibility of considering two different fiber populations thus overcoming the main limitation DTI (i.e. characterization of the diffusion in voxels with crossing fibers). The improved DTI metrics computed using the DIAMOND outputs are noted wMD, wAD, wRD and wFA which are computed using the following formula:

$$wM = \frac{frac_{f0} \times cM(frac_{f0}) + frac_{f1} \times cM(frac_{f1})}{frac_{f0} + frac_{f1}}, \quad (3.2)$$

where  $wM$  represents the resulting weighted DTI metric maps computed using the DIAMOND outputs and  $cM$  the DTI metric maps for each fiber population. As visible in Equation 3.2, the two fiber populations fractions are used as weights to determine the new metric maps. Figure 3.11 shows the relevant DIAMOND metric maps:

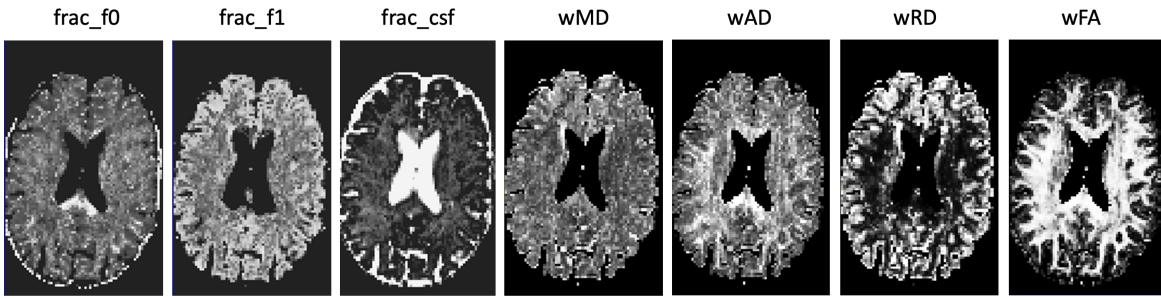


Figure 3.11: DIAMOND metrics maps of patient 20.03.01 at T1

### 3.4.4 MF metric maps

Finally, the Microstructure Fingerprinting (MF) model (see Section 1.3.3) is computed using the `fingerprinting` ElikoPy function. The outputs of the MF model are:

- `frac_f0`: First fiber population
- `frac_f1`: Second fiber population
- `fvf_f0`: First fiber population volume fraction
- `fvf_f1`: Second fiber population volume fraction
- `fvf_tot`: Total fiber volume fraction

As the interpretation of these metric maps is not straightforward, a new metric is computed as a combination of the outputs of the MF model. This metric is noted  $wfvf$  and is determined as follows:

$$wfvf = \frac{frac_{f0} \times fvf_{f0} + frac_{f1} \times fvf_{f1}}{frac_{f0} + frac_{f1}}. \quad (3.3)$$

This weighted total fiber volume fraction metric gives better interpretation of the proportion of both fiber populations within each voxel. The MF model metric maps are shown on Figure 3.12.

## 3.5 Statistical analysis

Since the main purpose of this study is to assess the efficacy of the HABIT-ILE rehabilitation treatment on stroke recovery, the statistical significance of the longitudinal

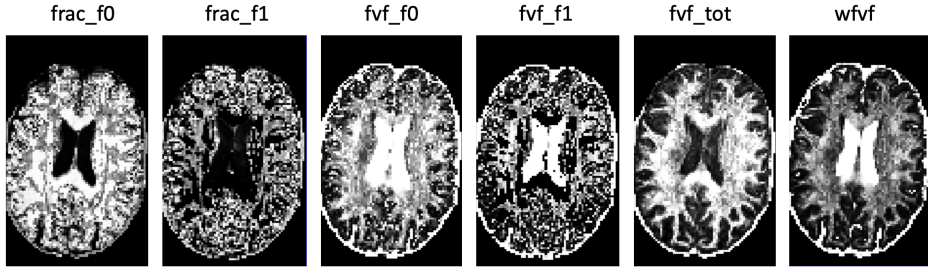


Figure 3.12: MF metrics maps of patient 20.03.01 at T1

evolution of dMRI metrics characterizing brain microstructural changes must be determined. The statistical significance of the evolution of metrics across the control and case populations and across the different acquisition times is evaluated using two sample independent t-tests. Two sample independent t-tests allow the comparison of the mean measurement between two populations in order to determine if the means of the two populations are statistically different. The comparison is quantified through a t-score and a p-value computed using the following formula [127]:

$$t = \frac{\bar{X}_{diff}}{s_{diff}/\sqrt{n}}; p-value = P(T \leq (or \geq) t | H_0), \quad (3.4)$$

where  $\bar{X}_{diff}$  is the sample mean of the differences,  $s_{diff}$  is the sample standard deviation of the differences,  $n$  is the sample size,  $T$  is the reference value of the test statistic,  $H_0$  is the null hypothesis that the two population means are equal. The comparison between the obtained p-value and the significance level set by the user ( $\alpha = 0.05$  in this case) allows to infer on the significance of the difference between the mean of metrics originating from different populations. The evolution of the different metrics from the various dMRI models can thus be correctly assessed as the statistically significant changes are highlighted. The independent t-tests were computed using the `scipy.stats` Python package.

# CHAPTER 4

## RESULTS

This chapter reports the results for the different regions of interest (ROIs) obtained by following the preprocessing methodology and by applying the multiple DW-MRI models detailed in Section 3.4. Results are reported on boxplots showing the longitudinal evolution of metrics across populations. Statistical significance is assessed through the use of t-tests which are directly added on the plots using the following notation:

- ns: Not significant,  $0.05 < p \leq 1$
- \*:  $0.01 < p \leq 0.05$
- \*\*:  $0.001 < p \leq 0.01$
- \*\*\*:  $0.0001 < p \leq 0.001$

As the corticospinal tract (CST) is the spotlight of this study, only the boxplots obtained using the DW-MRI models for the CST are included in this section. The boxplots for the Superior Cerebellar Pedunculus (sCP), Inferior Cerebellar Pedunculus (iCP), Middle Cerebellar Pedunculus (mCP), Cortico Ponto Cerebellum (CPC) and Superior Longitudinal Fasciculus I (SLF I) can be found in the Appendices A (DTI results), B (NODDI results), C (DIAMOND results) and D (MF results).

### 4.1 DTI results

Firstly, Mean Diffusivity (MD), Axial Diffusivity (AD, expressed in  $mm^2/s$ ), Radial Diffusivity (RD, expressed in  $mm^2/s$ ) and Fractional Anisotropy (FA) results are detailed for the corticospinal tract (CST), Superior Cerebellar Pedunculus (sCP), Middle Cerebellar Pedunculus (mCP), Inferior Cerebellar Pedunculus (iCP), Cortico Ponto Cerebellum (CPC) and Superior Longitudinal Fasciculus I (SLF I).

#### 4.1.1 Fractional Anisotropy

Fractional Anisotropy (FA) values in CST (see Figure 4.1) indicate a slight decrease on the ipsilesional and contralesional sides for both populations. Moreover, no significant changes occurred in the case population after the HABIT-ILE rehabilitation session (between T0 and T1 for the case population) on either side of the brain. However, the control population experienced a significant decrease in FA on the contralesional side after the rehabilitation process. Regarding the cerebellar WM pathways (see Figures

A.1 and A.2), similar trends of FA values can be observed. Indeed, the four ROIs indicate a slight FA decrease on both sides with no significant changes induced by the rehabilitation method for the case population. The control population shows significant decrease in FA between T2 and T3 on the ipsi- and contralesional sides. On the other hand, the Superior Longitudinal Fasciculus I (SLF I) (see Figure A.3) did not show significant FA variations.

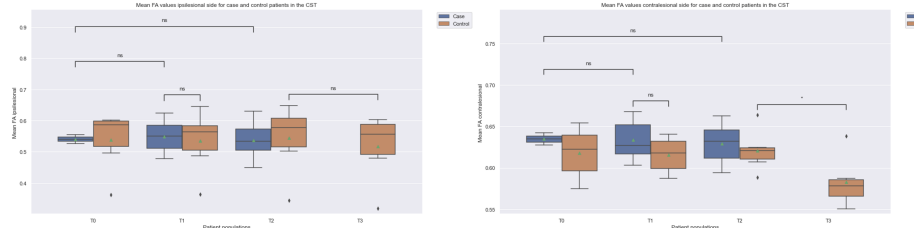


Figure 4.1: Fractional Anisotropy (FA) boxplots in the Corticospinal Tract (CST) on the ipsi- and contralesional sides for both patient populations

#### 4.1.2 Mean Diffusivity

Mean diffusivity (MD) values in the CST (see Figure 4.2) show a significant increase on the contralesional side after the HABIT-ILE treatment for the case population (between T0 and T1) but indicate a decrease for the control population (between T2 and T3). Similar MD trends are observable on Figures A.4 and A.5 on both ipsi- and contralesional sides. The SLF I reported significantly increased MD values on the contralesional side after the rehabilitation process for the case population, as visible on Figure A.6.

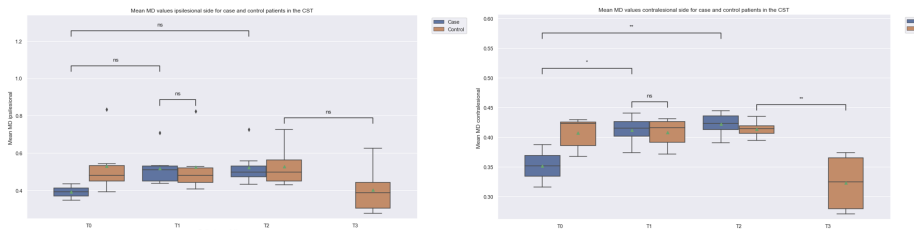


Figure 4.2: Mean Diffusivity (MD) boxplots in the Corticospinal Tract (CST) on the ipsi- and contralesional sides for both patient populations

#### 4.1.3 Axial Diffusivity

On both ipsilesional and contralesional sides, the mean Axial Diffusivity (AD) values in the CST (see Figure 4.3), CP (see Figures A.7 and A.8) and SLF I (see Figure A.9) significantly increase after the HABIT-ILE method in the case population and an opposite trend is observable for the control population in all regions except from the SLF I.

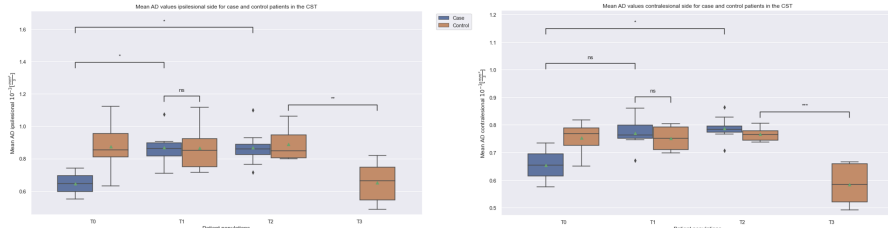


Figure 4.3: Axial Diffusivity (AD) boxplots in the Corticospinal Tract (CST) on the ipsi- and contralesional sides for both patient populations

#### 4.1.4 Radial Diffusivity

Similarly to the AD variations, the Radial Diffusivity (RD) mean values show significant increases in the CST (see Figure 4.4) and the CP (see Figures A.10 and A.11), on both sides of the brain after the rehabilitation process in the case population. The control population, however, follows an opposite trend as the RD mean values decrease in those regions. Although no significant changes occur in the SLF I (see Figure A.12), mean RD values show a slight increase on the ipsilesional and contralesional sides.

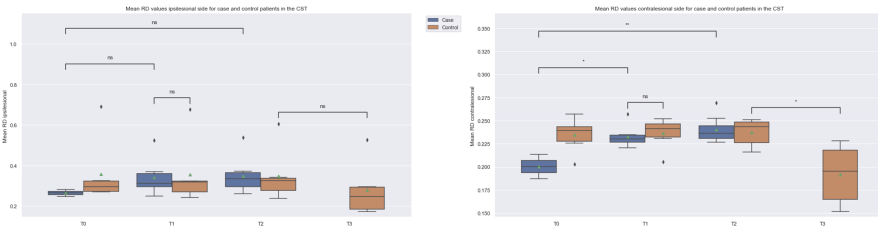


Figure 4.4: Radial Diffusivity (RD) boxplots in the Corticospinal Tract (CST) on the ipsi- and contralesional sides for both patient populations

## 4.2 NODDI results

This second section regroups and details the results of the WM analysis obtained using the NODDI model in the corticospinal tract (CST), Superior Cerebellar Pedunculus (sCP), Middle Cerebellar Pedunculus (mCP), Inferior Cerebellar Pedunculus (iCP), Cortico Ponto Cerebellum (CPC) and Superior Longitudinal Fasciculus I (SLF I). The metrics analyzed are the intracellular volume fraction ( $f_{\text{intra}}$ ), extracellular volume fraction ( $f_{\text{extra}}$ ), free water volume fraction ( $f_{\text{iso}}$ ) and fiber orientation dispersion index (ODI).

### 4.2.1 Fiber Orientation Dispersion Index

Figure 4.5 shows the fiber Orientation Dispersion Index (ODI) results in the CST. A slight decrease in ODI can be observed on Figure 4.5 on the contralesional and ipsilesional sides between T0 and T1 for the case population. In comparison, the control

population indicates a significant increase in ODI on both sides after undergoing the HABIT-ILE rehabilitation. The cerebellar peduncles WM pathways show similar tendencies with statistically significant reduction in ODI before and after rehabilitation on the contralateral and ipsilesional sides for the case population in the inferior, middle and superior cerebellar peduncles (see Figures B.1 and B.2). The control population displays a significant increase in ODI after the rehabilitation process. Although no significant changes can be observed in the SLF I, reduction in ODI mean values on both sides and for both population are observable on Figure B.3.

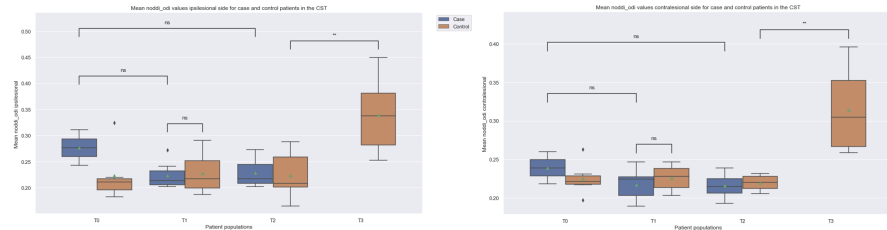


Figure 4.5: Fiber Orientation Dispersion Index (ODI) boxplots in the Corticospinal Tract (CST) on the ipsi- and contralateral sides for both patient populations

#### 4.2.2 Extracellular Volume Fraction

The case population presents significant increases in mean  $f_{\text{extra}}$  values on both hemispheres post rehabilitation and in all ROIs except from the iCP and the SLF I, as visible on Figures 4.6, B.4, B.5 and B.6. On the other hand, the case population is characterized by significant decreases in  $f_{\text{extra}}$  on both sides and in all ROIs except from the SLF I.

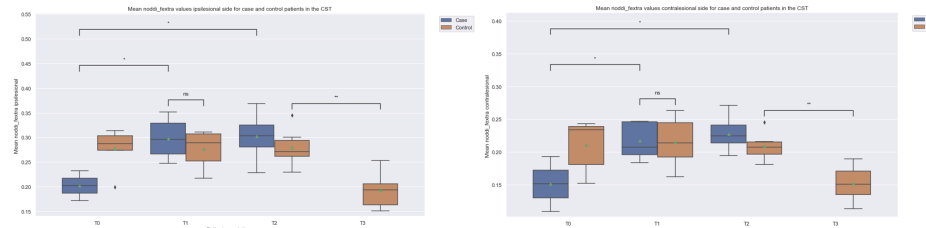


Figure 4.6: Extracellular volume fraction ( $f_{\text{extra}}$ ) boxplots in the Corticospinal Tract (CST) on the ipsi- and contralateral sides for both patient populations

#### 4.2.3 Intracellular Volume Fraction

The Intracellular Volume Fraction ( $f_{\text{intra}}$ ) is characterized by globally decreasing mean values on both sides for the case population. In the CST (see Figure 4.7), the contralateral side is more impacted by this decrease as it is indicated as more significant by the statistical tests. The other ROIs, except from the SLF I, indicate significant decreased mean values after rehabilitation on both sides for the case population. In contrast, the

control population shows increasing  $f_{\text{intra}}$  mean values which are reported as significant on the contralesional side in the CST and the CPC, on both sides in the iCP, mCP and sCP (see Figure B.7, B.8) and as not significant in the SLF I (see Figure B.9).

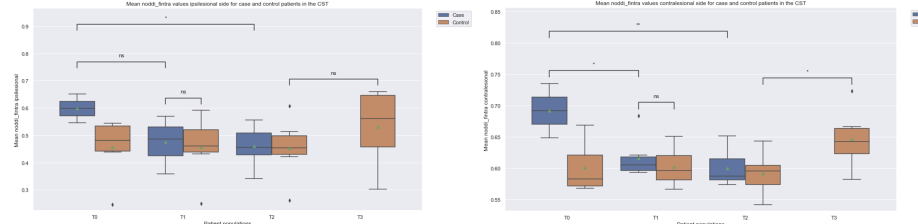


Figure 4.7: Intracellular volume fraction ( $f_{\text{intra}}$ ) boxplots in the Corticospinal Tract (CST) on the ipsi- and contralesional sides for both patient populations

#### 4.2.4 Free Water Volume Fraction

The free water volume fraction ( $f_{\text{iso}}$ ) did not present a lot of variation across acquisition times and ROIs. Indeed, no significant changes were reported on either side of the corticospinal tract (see Figure 4.8), the superior longitudinal fasciculus I (see Figure B.12) and the cortico ponto cerebellum pathway. The iCP and sCP presented significant results on the ipsilesional side as ( $f_{\text{iso}}$ ) increased after the HABIT-ILE treatment for the case population in both ROIs and decreased in the sCP and mCP for the control population (see Figures B.10 and B.11).

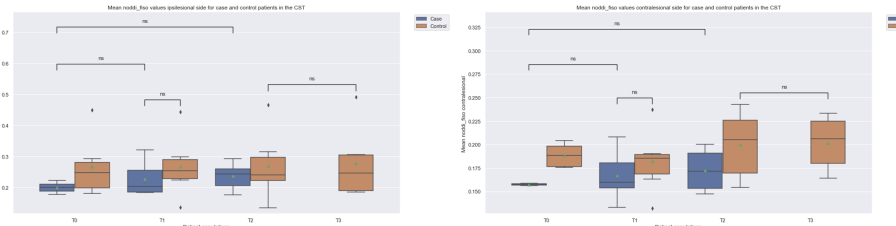


Figure 4.8: Free water volume fraction ( $f_{\text{iso}}$ ) boxplots in the Corticospinal Tract (CST) on the ipsi- and contralesional sides for both patient populations

### 4.3 DIAMOND results

As explained in Section 3.4.3, the DTI metrics (MD, AD, RD and FA) can be recomputed using the tensors of the two fiber populations modeled using DIAMOND. These adjusted or weighted DTI metrics are noted wMD, wAD, wRD and wFA and their changes are reported in the corticospinal tract (CST), Superior Cerebellar Pedunculus (sCP), Middle Cerebellar Pedunculus (mCP), Inferior Cerebellar Pedunculus (iCP), Cortico Ponto Cerebellum (CPC) and Superior Longitudinal Fasciculus I (SLF I).

### 4.3.1 Weighted Fractional Anisotropy

The weighted Fractional Anisotropy (wFA), as illustrated on Figures 4.9, C.1, C.2 and C.3, did not present many significant results. The control population showed significant decreases in wFA mean values on the contralesional side of the CST and iCP as well as in the mCP (see Figure C.2). The mCP also shows some increased mean wFA values after the rehabilitation method.

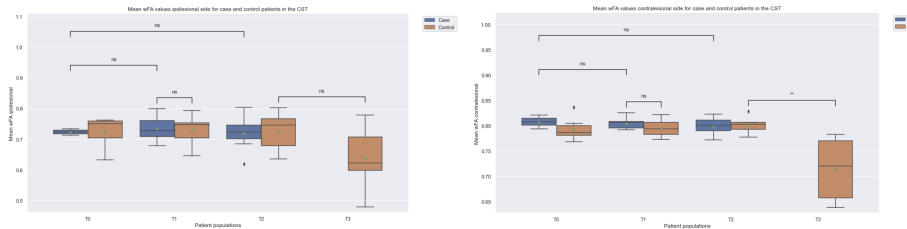


Figure 4.9: Weighted Fractional Anisotropy (wFA) boxplots in the Corticospinal Tract (CST) on the ipsi- and contralesional sides for both patient populations

### 4.3.2 Weighted Mean Diffusivity

Weighted Mean Diffusivity (wMD) mean values show a significant decrease on the ipsilesional and contralesional sides of the CST for the control population after rehabilitation whereas no significant changes were observed for the case population (see Figure 4.10). In contrast, the CPC shows increasing wMD values on the contralesional side for the case population and decreasing wMD values on the ipsilesional side for the control population. As visible on Figures C.4 and C.5, the iCP, mCP and sCP present a similar evolution as the mean wMD values increase on both sides for the case population but decrease on the contralesional side for the control population. The SLF I does not show any significant change.

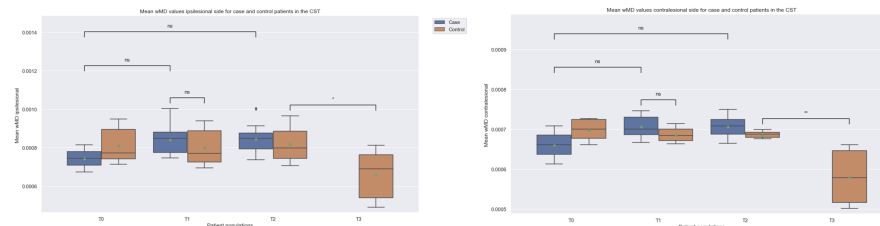


Figure 4.10: Weighted Mean Diffusivity (wMD) boxplots in the Corticospinal Tract (CST) on the ipsi- and contralesional sides for both patient populations

### 4.3.3 Weighted Axial Diffusivity

Figure 4.11, C.7 and C.8 indicate a significant decrease in weighted Axial Diffusivity (wAD) between T2 and T3 on both sides of the brain for the control population, in all regions except from the SLF I. Furthermore, the mean wAD values for the case

population presents an increase on the ipsilesional and contralesional sides of the iCP, mCP and sCP after rehabilitation.

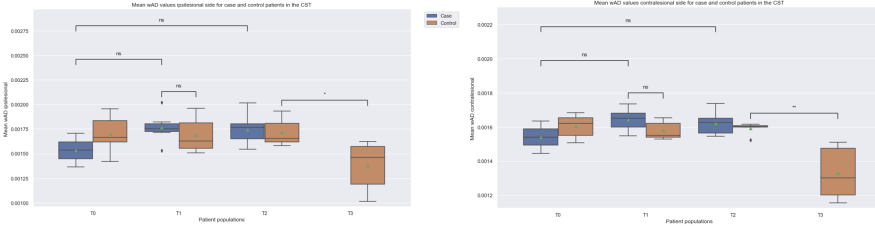


Figure 4.11: Weighted Axial Diffusivity (wAD) boxplots in the Corticospinal Tract (CST) on the ipsi- and contralesional sides for both patient populations

#### 4.3.4 Weighted Radial Diffusivity

Finally, boxplots of the weighted Radial Diffusivity (wRD) do not present large variations with the exception of an increase in wRD on the contralesional side of the iCP between T0 and T2 and on the ipsilesional side of the sCP between T0 and T1 for the case population (see Figures 4.12, C.10, C.12). The mCP also shows some changes in wRD as depicted on Figure C.11, it similarly increases between T0 and T1 for the case population and decreases between T2 and T3 for the control population.

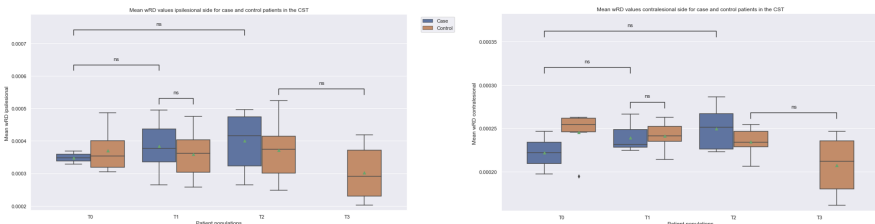


Figure 4.12: Weighted Radial Diffusivity (wRD) boxplots in the Corticospinal Tract (CST) on the ipsi- and contralesional sides for both patient populations

### 4.4 Microstructure Fingerprinting results

Lastly, the MF model is used to characterize the composition of each voxel. More precisely, MF metrics detail the fraction of occupancy of the voxel by the first (frac\_f0) and second (frac\_f1) fascicle populations as well as the CSF (frac\_csf), the total fiber volume fraction (fvf\_tot) and the weighted total fiber volume fraction (wfvf) which does not take the CSF compartment into consideration. As for the other microstructural models, the case and control populations show different results after rehabilitation. Moreover, less variations were observed using the MF model as no significant changes were reported for frac\_f0 in any of the ROIs and for any metrics in the SLF I.

#### 4.4.1 First Population Fraction

As visible on Figure 4.13, no significant changes on either sides of the brain occurred in the CSF. Furthermore, no significant variations were reported in the CP and SLF I as shown on Figures D.1, D.2 and D.3.

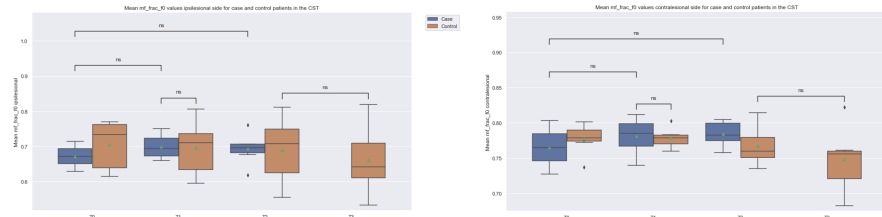


Figure 4.13: Fraction of occupancy of the first fascicle population (frac\_f0) boxplots in the Corticospinal Tract (CST) on the ipsi- and contralateral sides for both patient populations

#### 4.4.2 Second Population Fraction

Variations in frac\_f1 are visible on Figure 4.14 which shows decreased and increased mean values on the contralateral side of the CST for the case and control populations respectively. In the CPC, iCP, mCP and sCP, these two populations experienced similar evolution on the contra- and ipsilesional sides of the brain (see Figures D.4, D.5 and D.6)

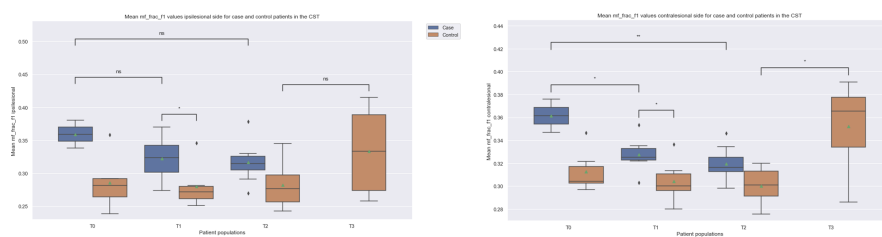


Figure 4.14: Fraction of occupancy of the second fascicle population (frac\_f1) boxplots in the Corticospinal Tract (CST) on the ipsi- and contralateral sides for both patient populations

#### 4.4.3 Free Water Fraction

The free water compartment did not undergo large variations across populations and regions. Indeed, as depicted on Figure 4.15 and D.9, no significant changes occurred in the CST or the SLF I. Some variations are visible in the sCP as decreases on the ipsilesional and contralateral sides were recorded for the control population between T2 and T3 (see Figures D.7 and D.8).

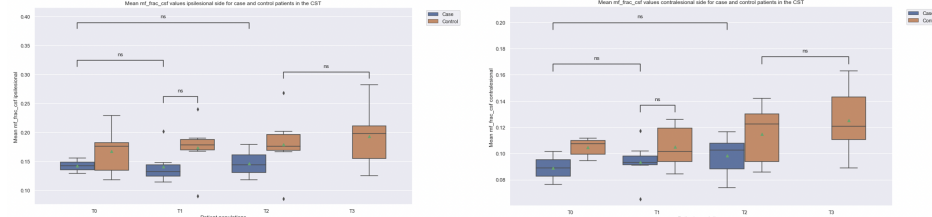


Figure 4.15: Fraction of occupancy of the CSF (frac\_csf) boxplots in the Corticospinal Tract (CST) on the ipsi- and contralateral sides for both patient populations

#### 4.4.4 Total Fiber Volume Fraction

The total fiber volume fraction (fvf\_tot) shows decreased mean values on the contralateral side of the CST after rehabilitation, for the case population (see Figure 4.16). The CPC, iCP, mCP and sCP show decreased mean fvf\_tot values on both sides of the brain between T0 and T1 for the case population and increased mean values between T2 and T3 for the control population, as visible on Figures D.10 and D.11.

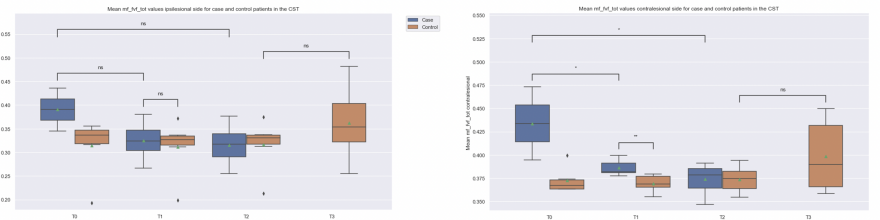


Figure 4.16: Total fiber volume fraction (fvf\_tot) boxplots in the Corticospinal Tract (CST) on the ipsi- and contralateral sides for both patient populations

#### 4.4.5 Weighted Total Fiber Volume Fraction

The weighted total fiber volume fraction (wfvf) metric shows less marked variations than the other metrics as only the case population displayed some significant changes in the CST and the CP pathways. Indeed, Figure 4.17 reports decreased wfvf mean values on the contralateral side of the CST, Figure D.13 similarly shows decreased mean values on both sides of the brain between T0 and T1 in the CPC, sCP and iCP, and Figure D.14 shows decreased values between T0 and T1 for the case population and increased value between T2 and T3 for the control population in the mCP.

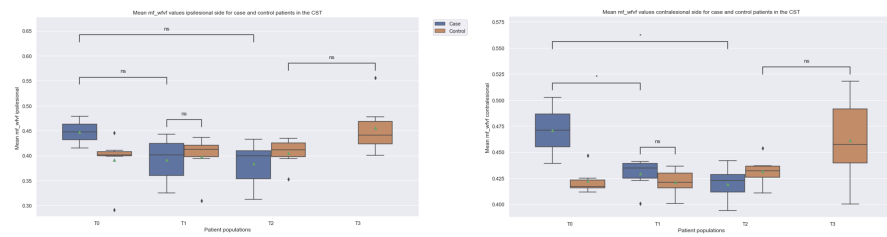


Figure 4.17: Weighted total fiber volume fraction (wfvf) boxplots in the Corticospinal Tract (CST) on the ipsi- and contralateral sides for both patient populations

# CHAPTER 5

## DISCUSSION

As the results presented in Chapter 4 indicate variations in the effect of the rehabilitation process on the various metrics extracted from the multiple DW-MRI models, a detailed review must be made in order to investigate the consistency of the reported results. Indeed, multiple metrics report opposite trends for the case and control population upon comparison of the results before and after rehabilitation. On this basis, two hypotheses can be formulated: either all of the reported results are accurate and some patient simply show different responses to the HABIT-ILE treatment, or one of the populations contains some inconsistencies which directly impact the processing of the data and, consequently, lead to erroneous interpretation of the results. This section aims at offering a detailed interpretation of the biological meaning of the results, providing insights on the hypotheses made, discussing the limitations of the conducted study and proposing a developed discussion about possible future perspectives.

### 5.1 DTI analysis

The evolution of the Diffusion Tensor Imaging metrics is used to infer on the microstructural integrity of the brain white matter. As previously mentioned, Fractional Anisotropy (FA) and Mean Diffusivity (MD) metrics are sensitive to the orientation and the degree of density of both axonal and myelin characteristics of WM tracts. FA is generally interpreted as a measure of WM axonal integrity and organization, and also reflects the distribution of Axial Diffusivity (AD) and Radial Diffusivity (RD) changes. AD represents the overall axon integrity and decreased AD values are often associated with axonal damage and degeneration. RD, on the other hand, is more specific to the myelin sheath integrity and to the degree of myelination. The more general MD metric can then be seen as an indicator of cell membrane deterioration since it is sensitive to inflammation, edema, and necrosis. The comparison of the patients' DTI results before and after undergoing the HABIT-ILE rehabilitation method indicate opposite tendencies when comparing the case and control populations across the different regions of interest. These differences in DTI metrics evolution can thus be interpreted as two distinct scenarios in which different biological phenomena take place.

The CPC and the SLF I pathways show less variation than the CST, iCP, mCP and sCP regions. On the one hand, the case population show increased RD and MD on the contralesional side, increased AD on both sides and no significant changes in FA.

These changes can be interpreted as myelin sheath impairment on the contralesional side coupled with axonal regeneration on both sides of the brain. On the other hand, the control population is characterized by significant reductions in all of the DTI metrics mainly on the contralesional side of the brain. Biologically, this illustrates a loss of axonal integrity combined with a higher degree of fiber density.

Even though both populations show contrasted results, these results stay consistent throughout the different regions of interest investigated. Depending on the population, these regions thus seem to experience similar biological changes due to the rehabilitation method. Moreover, the fact that the CPC and SLF I pathways are less impacted indicates that primary motor WM tract such as the CST, iCP, mCP and sCP experience more changes due to the rehabilitation process. However, as discussed in Section 1.2.2, the Diffusion Tensor Imaging models comprises some major limitations directly impacting the biological interpretability of its metrics. Indeed, inaccuracies in the modeling of complex fiber orientation and architecture may lead to misinterpretations of the actual anatomical microstructure. These limitations are especially impactful in the study of altered WM integrity after stroke as WM pathways experience heterogeneous and complex degeneration (and regeneration) mechanisms. Furthermore, although DTI metrics can be used to correctly assess the impact of the lesion on the CST after stroke up to a certain extent, its capability to accurately characterize complex microstructural rearrangement after stroke still needs further investigation.

## 5.2 NODDI analysis

The NODDI model yields information about the fiber orientation through the ODI and about the volume fraction of fibers ( $f_{\text{intra}}$ ), microglial cells ( $f_{\text{extra}}$ ) and CSF ( $f_{\text{iso}}$ ) in every voxel. Similarly to the obtained DTI results, the two patient populations reported diverging trends across the ROIs with the exception of the SLF I in which no significant changes were reported for either population. Moreover, changes in one of the three volume fractions were consistently accompanied by an opposite change in another volume fraction. This indicates sound and logical variations in the neurite populations within each voxel. As explained in Section 1.3.1,  $f_{\text{intra}}$  represents the intraneurite compartment and increases in the volume fraction associated to this compartment can thus be assimilated to axonal regeneration. Secondly,  $f_{\text{extra}}$  changes are related to variations in the proportion of microglial cells which, in turn, impacts the integrity of the myelin sheath. Thirdly, changes to the free water compartment, assimilated to the CSF, are represented through  $f_{\text{iso}}$  which balances the changes in intra- and extracellular compartments.

The case population is characterized by decreased  $f_{\text{intra}}$  mean values in the CST, CPC, iCP, mCP and sCP regions, translating decreased proportions of WM fibers on both sides of the brain. These same regions show increased  $f_{\text{intra}}$  and  $f_{\text{iso}}$  values indicating increasing proportions of microglial cells and free water. In contrast, the control popu-

lation shows axonal regrowth in the same regions as  $f_{\text{intra}}$  increases significantly after the rehabilitation process. Moreover, this change in  $f_{\text{intra}}$  is followed by a decrease in  $f_{\text{extra}}$  thus indicating altered myelin integrity. This observed evolution might be explained by axonal swelling, causing a reduction in extracellular water component due to anomalous transmembrane diffusion, which has already been reported in other studies [128]. Finally, the ODI decreased for most of the regions in the case population but significantly increased for the control population. Increased ODI values may indicate loss of tissue structural integrity.

As for the DTI model, the NODDI multi-compartment models involves some limitations. Indeed, this model relies on strict assumptions on the diffusivities of the compartments based on normal brain tissues. The adaptability of this model to the characterization of WM integrity in the case of severe stroke infarct is thus not guaranteed as the complex organization of brain tissues might not be accurately modeled leading to altered interpretation of the underlying biological phenomena.

### 5.3 DIAMOND analysis

The metrics obtained using the DIAMOND model were, as explained in Section 3.4.3, used to compute the adjusted DTI metrics: wMD, wAD, wRD and wFA. Upon comparison with the associated DTI metrics, DIAMOND metrics show similar but fewer variations in the ROIs and no variation in the SLF I. Moreover, the weighted DTI metrics obtained using DIAMOND share a similar biological interpretation with the regular DTI metrics.

The case population shows increases in wAD, wMD and wRD with no change in wFA thus indicating axonal regeneration and loss of myelin sheath integrity in all ROIs except from the SLF I. On the other hand, the control population indicates reduced wAD and wMD on both hemispheres of the brain accompanied with wFA reduction and wRD decrease on the contralateral side of the iCP as well as in the mCP. These results indicate a loss of fiber microstructural integrity combined with a higher myelin sheath integrity on the contralateral side of the iCP and in the mCP.

Despite the fact that the DIAMOND model does not rely on assumptions regarding the underlying diffusivity in each voxel which allows for the modeling of more complex microstructural architecture, the number of compartment still has to be defined by the user. In this case, the number of compartments was set to 3 (isotropic, hindered and restricted diffusion) and this might constitute a limitation to the capture of the complex mechanisms of WM fibers rearrangement after stroke.

## 5.4 MF analysis

The last model used to obtain results is the Microstructure Fingerprinting model which represents the fascicles as a hexagonal packing of cylinders. Using this model, the volume fractions of the fascicle populations ( $\text{frac\_f0}$  and  $\text{frac\_f1}$ ) and the CSF ( $\text{frac\_csf}$ ) can be extracted and their evolution can be compared after the HABIT-ILE rehabilitation method. In addition, the total volume fraction of fibers ( $\text{fvf\_tot}$ ) as well as the weighted total fiber volum fraction ( $\text{wfvf}$ ) are used to characterize the WM evolution in each voxel.

In comparison to the other microstructural models, the MF model reports less significant changes for both population. First of all, the case population is characterized by overall decreasing metrics after rehabilitation. Biologically, this indicates smaller compartments dedicated to fibers in voxels along with a decrease in the concentration of fibers. On the opposite, the control population indicates increasing fiber volume fractions in the CST, CPC, sCP, mCP and iCP after rehabilitation as well as globally increased wfvf mean values. These changes seem to translate the fact that axonal regeneration took place in the fiber population compartments.

The MF model is based on the use of a dictionary build through the use of Monte Carlo simulations of the random walk of water molecules. This technique allows the modeling of the underlying microarchitecture without the need of *a priori* knowledge regarding the structure of the tissue and the diffusion properties of water molecules. However, although the mean values of the results obtained using the MF model were similar across populations, the presence of outliers for multiple acquisition times impacted the results. The latter must thus be interpreted with caution.

## 5.5 Summary

As demonstrated by the results, the effects of the HABIT-ILE rehabilitation method on the WM microstructure of the ROIs are not straightforward to interpret. Indeed, various metrics from different models show diverging trends of evolution after rehabilitation. Moreover, the microstructural DW-MRI models show varying sensitivity in the characterization of the underlying tissue architecture as DIAMOND and MF presented less significant results than other models, for example. Moreover, some metrics follow similar trends across all of the considered regions of interest (e.g. MD from the DTI model) whereas other metrics do not show any significant changes in the ROIs (e.g.  $\text{frac\_f0}$  from the MF model). Metrics generally describing similar biological concepts also show some contradiction upon comparison between models (e.g. RD from the DTI model and  $f_{\text{extra}}$  from the NODDI model). These inconsistencies illustrate the fact the models used in this study give complementary information regarding the underlying microstructure of the studied tissues.

Both populations displayed the majority of their changes in the corticospinal tract

(CST) and cerebellar peduncles (CP). This highlights the fact that the brain WM regions directly responsible for the transmission of motor information experienced more microstructural changes. Indeed, the CST is the main neuronal pathway responsible for the transfer of voluntary motor outcome from the cortex into the spinal cord and the CP, although each peduncle has its own function, form the collection of afferent and efferent tracts of the cerebellum which plays a key role in the transmission of motor information. In contrast, the cortico-ponto cerebellar (CPC) pathway and the superior longitudinal fasciculus I (SFL I), two areas carrying information related to motor spatial information, balance, regulation of motor control, perception and cognition reported less pronounced changes.

The analysis of the overall biological changes after the HABIT-ILE rehabilitation treatment reported by the case population indicate loss of density in WM fibers, loss of myelin sheath integrity and mixing results regarding axonal degeneration. These results seem to translate an overall negative evolution in motor recovery. The control population, on the other hand, shows signs of axonal regrowth, increased fiber density as well as improved myelin sheath integrity indicating better information transfer through the WM pathways. Revisiting the hypotheses set at the beginning of this section, some possible explanatory tracks can be developed in order to conclude this study. A first possible explanation would be that the results of the case or control population are erroneous thus implying that the rehabilitation treatment may have overall positive or neutral effects on the brain microstructure. Secondly, the results could be explained by the fact that patients may react differently to the rehabilitation method which could be helpful for some patients but ineffective for other patients which would still experience WM degeneration induced by stroke. Finally, a third explanation would be that the methods used in this study do not enable a complete and accurate assessment of the effects of the HABIT-ILE treatment on the expected motor outcomes of the patients.

## 5.6 Limitations

Although the limitations of each model have already been detailed in the previous sections, limitations inherent to the data and methods used in this study still remain. An overview of the limitations of this study may give further insight on the contrasted results obtained.

Firstly, as mentioned in Section 2.2.5, some limitations are specific to the framework of stroke study. Similarly to other studies in this field, the present work is directly impacted by the heterogeneity of the stroke patients as well as the lesions presented by these patients. Indeed, the patients studied in this work suffer from hemorrhagic and ischemic strokes in different regions of the brain and present differences in age and in duration from the stroke onset. Furthermore, due to the multiple drop outs that occurred prior to the first acquisition sequence (T0) as well as in between subsequent acquisition sequences (T1, T2 and T3), this study only has access to a relatively small

sample size. This small sample size considerably limits the statistical interpretability of the obtained results and, as some scans are missing for multiple patients, the accuracy of the longitudinal study is limited. Indeed, patients constituting the case and control populations vary from one acquisition time to the other which then limits the accuracy of the statistical tests performed.

Secondly, other limitations are proper to the raw data used in this study. A first visual quality check of the raw MRI data indicated that some significant imperfections were detected for the first acquisition session of multiple patients. As shown in Figure 3.4, an important number of slices were missing from the scans in multiple patients (*20.01.01.E0, 20.02.01.E0, 20.03.01.E0, 20.05.02.E0, 20.07.01.E0*) from the case population. Since these incomplete scans were removed from this study, only two patients remained in the case population at time T0 which considerably diminishes the analysis of the efficacy of the HABIT-ILE treatment for the case population. Other defects were noticed at time T0 as illustrated on Figure 5.1. The latter shows that the resolution of the different views varied from the first acquisition time (T0) to the other acquisition times. Furthermore, the base of these scans show the presence of some noise and artifacts affecting the extraction of the data at the base of the brainstem.

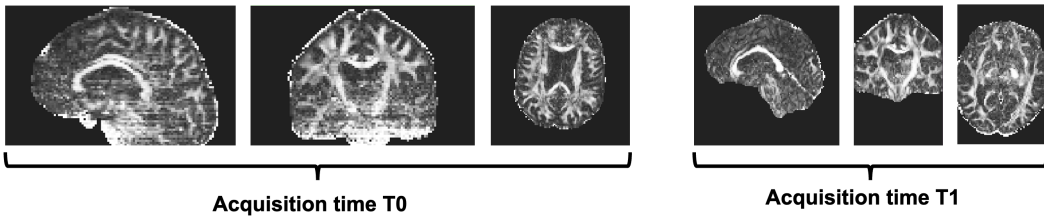


Figure 5.1: Imperfections of the first acquisition session illustrated for patient *20.06.01* at times T0 and T1

These imperfections recorded during the acquisition of the data combined with the artifacts generally affecting MR images (see Section 1.1.9) might have some impact on the preprocessing, registration and processing of the data.

In that regard, the preprocessing performed using the ElikoPy pipeline also showed some imperfections as the brain masks and WM masks used in this work did not perfectly correspond to the biological truth in some cases. Moreover, the quality report obtained after performing the preprocessing indicate substantial translational and rotational patient movements during the acquisition scans. The correction of these motion artifacts may not be perfect thus impacting the following processing steps.

Another key aspect of this study was the registration of the atlas maps from the MNI space towards the patients' native space. As previously mentioned, the imperfections related to data acquisition and preprocessing have a direct impact on the quality of the registration step. Furthermore, due to the number of registered regions, visual quality checks were not performed at every step of the registration process. Consequently, the

parameters set to perform the automatic registration of the ROIs may have a significant impact on some of the registered regions. First, the atlas maps used are probabilistic maps which were then binarized according to an arbitrary threshold introducing a certain degree of uncertainty into the obtained registered regions. Secondly, the brains of the patients in this study present some severe alteration due to the impairments caused by stroke and the automatic registration of healthy reference brain regions on a brain presenting microstructural and macrostructural damage is still to be improved. Moreover, no hand-drawn or semi-automatically generated lesion masks were available for this study. The use of lesions masks has been reported to improve the accuracy of the registration of brain regions directly impacted and surrounding the stroke lesions. To overcome this limitation, the registration process was composed of an affine and a diffeomorphic step. The latter allowed the identification of the "most probable region" corresponding to the reference atlas map. On the one hand, this method allowed for the identification of ROIs even in brain regions presenting substantial alteration but, on the other hand, the identification of these regions is only probabilistic and may not correctly represent the underlying tissue architecture. Figure 5.2 illustrates this with a concrete example: the purely affine registration of the CST is compared to the affine and diffeomorphic registration of the CST for the same patient. As depicted by this example, the diffeomorphic step allows the definition of a ROI that circumvents the lesioned area of the brain whereas the purely affine registration tends to pass through the lesion. Although this allows for the identification of less affected ROIs, it may not correspond to the biological truth. The definition of ROIs containing patients' lesions may have lead to different results and interpretations. At last, the registered regions compared between the different acquisition times (T0, T1, T2 and T3) are not exactly identical. The averages of the different metrics are thus computed and compared on slightly varying brain regions.

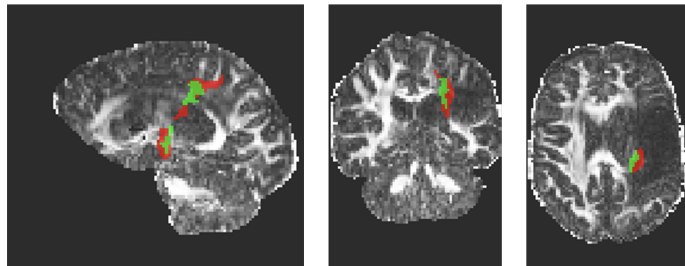


Figure 5.2: Purely affine registration (red) compared to affine and diffeomorphic registration (green), illustrated for patient 20.02.02 at times T0

On the latter point, the regions studied were selected based on the reported results found in the literature (see Section 2.2) and regarding the availability in online reference atlas maps corresponding to these regions. Some regions for which significant microstructural changes were reported in other studies were not used to perform the analysis conducted in the present work. For example, the corpus callosum (CC) which plays a key role in the execution of bi-manual motor tasks could provide additional

information on the effects of the rehabilitation process. Unfortunately, the atlas maps of the CC available online were not initially set in the MNI space and the registration process of these maps towards patients' native space did not yield satisfying results as illustrated in Appendix E. Other suggested improvements regarding the selection of regions of interest are discussed in the following section.

Finally, one could discuss the fact that only one rehabilitation method was assessed in this study. Indeed, as the HABIT-ILE rehabilitation method was originally developed for the reeducation of children with cerebral palsy (CP), comparing the present results with results obtained using another rehabilitation method could give further insight on the advantages and disadvantages of the HABIT-ILE method and on its efficacy for adult stroke patients. Furthermore, the results of the multiple behavioral tests discussed in Section 3.1.3 were not available. The correlation between the evolution of the multiple DW-MRI models metrics and the behavioral scores was thus not investigated. This additional analysis may assist in the confirmation or the rebuttal of the obtained findings and their interpretation.

## 5.7 Future Perspectives

In accordance to the limitations stated in the previous section, various improvement perspectives are discussed for further DW-MRI research opportunities in the framework of stroke characterization.

Naturally, increasing the number of patients available for this study, ensuring non varying patient populations for the different acquisition sessions and reducing the heterogeneity of the patients studied would allow for an increased statistical accuracy in this longitudinal study. Furthermore, the acquisition sequence used in this study was initially designed for the measurement of DW-MRI data in young infants. As the brains of neonates and young infants present higher water contents, a second b-value of  $700\text{ s/mm}^2$  is chosen over the more generally used  $1000\text{ s/mm}^2$  b-value. However, this study focuses on adult patients and the use of an additional b-value of  $1000\text{ s/mm}^2$  may help in obtaining a better characterization of the brain microstructure and in reducing the risk of systematic errors due to patient motion.

Furthermore, as the heterogeneity of lesions is one of the key limitations in the study of stroke, the accuracy of the registration process and the selection of the regions of interest is of the upmost importance. Although very time consuming, hand-drawn ROIs still present the most reliable results as compared to fully automatic registered ROIs such as the ones used in this study. However, the definition of the regions of interest can be improved using different techniques. Firstly, the ROIs obtained through automatic registration can be subdivided into multiple segments studied separately in order to improve the sensitivity of DW-MRI models to microstructural changes. For example, the CST can be divided into superior, middle and inferior segments on which

independent microstructural analysis is performed, thus allowing for finer analysis possibilities. Secondly, Constrained Spherical Deconvolution tracking algorithms can be used to identify tract-based ROIs semi-automatically (see Appendix F for more information). Using correctly placed seeds, targets, inclusion and exclusion regions, WM streamlines of interest can be identified. The obtained tractograms can then be used to determine the quantitative nature of brain streamlines using methods such as Spherical-deconvolution Informed Filtering of Tractograms (SIFT) [129] or White Matter Query Language (WMQL) [130], and to define WM tract-based ROIs. In addition, other techniques such as Tract-Based Spatial Statistics (TBSS) can be used to perform voxel-based analysis (VBA) of DTI data by analyzing DTI metrics along WM tracts on a voxel-wise basis [131]. Thirdly, the FreeSurfer software [132] can be used in combination with the FSL software [133] to perform a complete brain segmentation (see Appendix G) using brain reference atlases (the Desikan-Killiany atlas and the Destrieux atlas). Although computationally demanding, the use of the FreeSurfer software package allows the preprocessing of the raw dMRI data and outputs labeled maps of the major brain regions which can then be used to define precise regions of interest.

Moreover, the combination of whole-brain tractograms and segmented brain maps can be used to investigate the impact of stroke on the entire brain and its network properties. Indeed, the development of whole-brain structural connectomes (see Appendix G for a practical example) gives the opportunity to investigate the underlying network mechanisms of neural interactions after stroke in the whole brain. Inspiring studies such as the work performed by Koch et al. [98] and Guggisberg et al. [2] pave the way towards novel structural and functional assessment of stroke rehabilitation. Concretely, whole-brain structural connectomes can be used in combination with statistical classifiers, such as the support vector classifier machine classifier, to determine the key characteristics of the recovery process after stroke. In addition, the use of such statistical classification allows to identify the patients' response rate to the rehabilitation treatment used and this might then be generalized to determine personalized treatment for each patient. In the present study, this could be used to assess the efficacy of the HAIT-ILE rehabilitation method for each patient through the identification of neuroplasticity mechanisms. Furthermore, the functional network plasticity after stroke can also be studied and related to the structural changes. Indeed, functional MRI can be used to gain addition information on the sensorimotor pathways of the brain. A complete functional and structural analysis of the impact of stroke on neural networks would constitute a great improvement to this study.

Along those lines, the acquisition of additional data, such as fMRI data, may be of great assistance in predicting motor outcome after stroke. For example, motor tracts excitability can be investigated by using Transcranial Magnetic Stimulation (TMS). Other microstructural models such as Diffusion Kurtosis Imaging and Correlation Tensor MRI [74] could also be a great addition to this study.

Finally, the development of a reference pipeline in the framework of predicting motor

outcome using DW-MRI in stroke would greatly improve the comparability of studies in this field.

## CONCLUSION

The quantification of microstructural brain changes provoked by stroke is a fast developing field of research that has its share of limitations. However, recent developments in diffusion Magnetic Resonance Imaging modeling techniques and advances towards the standardization of methods employed in the characterization of stroke induced microstructural changes allow the achievement of promising advances in the assistance of stroke recovery.

This Master's thesis studies the microstructural evolution of 15 patients recovering from ischemic or hemorrhagic chronic stroke and following the HABIT-ILE motor rehabilitation method. In this regard, this study begins with a detailed summation of the theoretical principles of diffusion MRI techniques used throughout this work and provides a narrative review of the recent advances in this field of research. In the aim of providing a solid basis to future similar studies, the complete data processing pipeline methods are illustrated using concrete examples. The detailed methods include explanations regarding the preprocessing of the data performed using the ElikoPy pipeline, an overview of the registration process and the identification of regions of interest (ROIs) using standardized atlas maps, and a description of the models used to characterize the brain microstructural changes and their associated metrics. The obtained results are then reported for every DW-MRI model (DTI, NODDI, DIAMOND, MF) in all the selected ROIs (corticospinal tract, cortico-ponto cerebellar pathway, superior cerebellar peduncle, inferior cerebellar peduncle, middle cerebellar peduncle, and superior longitudinal fascicle I).

The interpretation and discussion of the results is based on the subdivision of patients into two distinct populations which followed the rehabilitation treatment at different times. The results of this longitudinal study report contrasted tendencies among the two populations. Indeed, the first population indicated loss of density in WM fibers, loss of myelin sheath integrity and mixing results regarding axonal degeneration whereas the second population showed signs of axonal regrowth, increased fiber density as well as improved myelin sheath integrity. Both populations displayed the majority of their changes in brain WM regions associated with primary motor functions but also showed some variations in secondary motor pathways. However, the comparison and interpretation of the multiple metrics obtained using the different microstructural models still present some limitations in their capacity to assess and characterize biological changes and should thus be interpreted with caution. Nevertheless, the findings of this study highlight the fact that significant WM changes occurred in the investigated ROIs. These changes indicate an overall degenerative evolution for the first population but present

a globally positive evolution for the second one.

In light of the obtained results, the present study displays some limitations inherent to the data used and related to the methods employed for the data processing. The discussion of these limitations is completed with suggestions for improvement and for novel research possibilities allowing the complete assessment of the impact of stroke on the structural and functional integrity of neural networks.

Notwithstanding the experienced difficulties, this study describes a complete procedure for the analysis of microstructural changes in brain regions affected by stroke and associated with motor functions. It also reports the obtained results and attempts to accurately interpret these results. This Master's thesis paves the way for future researches using DW-MRI techniques to study motor disability from stroke.



## BIBLIOGRAPHY

- [1] Luciana M. Moura et al. “Diffusion Tensor Imaging Biomarkers to Predict Motor Outcomes in Stroke: A Narrative Review”. en. In: *Frontiers in Neurology* 10 (May 2019), p. 445. ISSN: 1664-2295. DOI: 10.3389/fneur.2019.00445. URL: <https://www.frontiersin.org/article/10.3389/fneur.2019.00445/full> (visited on 07/29/2022).
- [2] Adrian G. Guggisberg et al. “Brain networks and their relevance for stroke rehabilitation”. en. In: *Clinical Neurophysiology* 130.7 (July 2019), pp. 1098–1124. ISSN: 13882457. DOI: 10.1016/j.clinph.2019.04.004. URL: <https://linkinghub.elsevier.com/retrieve/pii/S1388245719301270> (visited on 08/07/2022).
- [3] Daniel C. Alexander et al. “Imaging brain microstructure with diffusion MRI: practicality and applications”. en. In: *NMR in Biomedicine* 32.4 (Apr. 2019). ISSN: 0952-3480, 1099-1492. DOI: 10.1002/nbm.3841. URL: <https://onlinelibrary.wiley.com/doi/10.1002/nbm.3841> (visited on 02/24/2022).
- [4] B Kastler et al. *Comprendre l'IRM*. fr. OCLC: 1026755244. Elsevier Masson, 2011.
- [5] F Peeters. *LGBIO2050 : Medical Imaging, Chapter 4 : Magnetic Resonance Imaging*. en. Ecole Polytechnique de Louvain, 2017.
- [6] Vijay P.B. Grover et al. “Magnetic Resonance Imaging: Principles and Techniques: Lessons for Clinicians”. In: *Journal of Clinical and Experimental Hepatology* 5.3 (Sept. 2015), pp. 246–255. ISSN: 0973-6883. DOI: 10.1016/j.jceh.2015.08.001. URL: <https://www.ncbi.nlm.nih.gov/pmc/articles/PMC4632105/> (visited on 07/07/2022).
- [7] *T1 et T2 et phase de relaxation du phénomène de résonance magnétique nucléaire en IRM*. fr. URL: <https://www.imaios.com/fr/e-Cours/e-MRI/RMN/relaxation-rmn> (visited on 07/07/2022).
- [8] Zach Drew. *Magnetic field homogeneity / Radiology Reference Article / Radiopaedia.org*. en-US. DOI: 10.53347/rID-60855. URL: <https://radiopaedia.org/articles/magnetic-field-homogeneity> (visited on 07/07/2022).
- [9] *MR signal*. en. URL: <http://mriquestions.com/origin-of-mr-signal.html> (visited on 07/07/2022).
- [10] J. Ray Ballinger. *Spin echo sequences / Radiology Reference Article / Radiopaedia.org*. en-US. DOI: 10.53347/rID-22136. URL: <https://radiopaedia.org/articles/spin-echo-sequences?lang=us> (visited on 07/07/2022).
- [11] Jeremy Jones. *T1 weighted image / Radiology Reference Article / Radiopaedia.org*. en-US. DOI: 10.53347/rID-5852. URL: <https://radiopaedia.org/articles/t1-weighted-image?lang=us> (visited on 07/08/2022).

- [12] Jeremy Jones. *T2 weighted image* / Radiology Reference Article / Radiopaedia.org. en-US. DOI: 10.53347/rID-6345. URL: <https://radiopaedia.org/articles/t2-weighted-image?lang=us> (visited on 07/08/2022).
- [13] Zach Drew. *Proton density weighted spin-echo images* / Radiology Reference Article / Radiopaedia.org. en-US. DOI: 10.53347/rID-60744. URL: <https://radiopaedia.org/articles/proton-density-weighted-spin-echo-images-1?lang=us> (visited on 07/08/2022).
- [14] *MRI Basics*. URL: <https://case.edu/med/neurology/NR/MRI%20Basics.htm> (visited on 07/08/2022).
- [15] Yuranga Weerakkody. *MRI artifacts* / Radiology Reference Article / Radiopaedia.org. en-US. DOI: 10.53347/rID-16585. URL: <https://radiopaedia.org/articles/mri-artifacts-1> (visited on 07/24/2022).
- [16] Katarzyna Krupa and Monika Bekiesinska-Figatowska. "Artifacts in Magnetic Resonance Imaging". In: *Polish Journal of Radiology* 80 (Feb. 2015), pp. 93–106. ISSN: 1733-134X. DOI: 10.12659/PJR.892628. URL: <https://www.ncbi.nlm.nih.gov/pmc/articles/PMC4340093/> (visited on 07/24/2022).
- [17] M. Poustchi-Amin et al. "Principles and applications of echo-planar imaging: a review for the general radiologist". eng. In: *Radiographics: A Review Publication of the Radiological Society of North America, Inc* 21.3 (June 2001), pp. 767–779. ISSN: 0271-5333. DOI: 10.1148/radiographics.21.3.g01ma23767.
- [18] Frank Gaillard. *Phase-encoded motion artifact* / Radiology Reference Article / Radiopaedia.org. en-US. DOI: 10.53347/rID-1868. URL: <https://radiopaedia.org/articles/phase-encoded-motion-artifact-3?lang=us> (visited on 07/24/2022).
- [19] *MRI Artifacts* / Oncology Medical Physics. URL: <https://oncologymedicalphysics.com/mri-artifacts/> (visited on 07/24/2022).
- [20] Frank Gaillard. *Chemical shift artifact* / Radiology Reference Article / Radiopaedia.org. en-US. DOI: 10.53347/rID-1103. URL: <https://radiopaedia.org/articles/chemical-shift-artifact-1?lang=us> (visited on 07/24/2022).
- [21] Usman Bashir. *Magnetic susceptibility artifact* / Radiology Reference Article / Radiopaedia.org. en-US. DOI: 10.53347/rID-18971. URL: <https://radiopaedia.org/articles/magnetic-susceptibility-artifact?lang=us> (visited on 07/24/2022).
- [22] Usman Bashir. *Gibbs and truncation artifacts* / Radiology Reference Article / Radiopaedia.org. en-US. DOI: 10.53347/rID-16567. URL: <https://radiopaedia.org/articles/gibbs-and-truncation-artifacts?lang=us> (visited on 07/24/2022).
- [23] J. Yeung. *Aliasing on MRI* / Radiology Reference Article / Radiopaedia.org. en-US. DOI: 10.53347/rID-15691. URL: <https://radiopaedia.org/articles/aliasing-on-mri?lang=us> (visited on 07/24/2022).
- [24] J. Ray Ballinger. *Moiré fringes* / Radiology Reference Article / Radiopaedia.org. en-US. DOI: 10.53347/rID-22003. URL: <https://radiopaedia.org/articles/moire-fringes-2?lang=us> (visited on 07/24/2022).

- [25] Usman Bashir. *Zipper artifact / Radiology Reference Article / Radiopaedia.org*. en-US. DOI: 10.53347/rID-16558. URL: <https://radiopaedia.org/articles/zipper-artifact?lang=us> (visited on 07/24/2022).
- [26] Usman Bashir. *Diffusion-weighted imaging / Radiology Reference Article / Radiopaedia.org*. en-US. DOI: 10.53347/rID-16718. URL: <https://radiopaedia.org/articles/diffusion-weighted-imaging-2?lang=us> (visited on 07/24/2022).
- [27] T.A.G.M. Huisman. "Diffusion-weighted and diffusion tensor imaging of the brain, made easy". In: *Cancer Imaging* 10.1A (Oct. 2010), S163–S171. ISSN: 1740-5025. DOI: 10.1102/1470-7330.2010.9023. URL: <https://www.ncbi.nlm.nih.gov/pmc/articles/PMC2967146/> (visited on 07/24/2022).
- [28] Donald W McRobbie. *MRI from picture to proton*. en. OCLC: 181655274. Cambridge, UK; New York: Cambridge University Press, 2006. ISBN: 978-0-511-34944-7 978-0-511-34849-5 978-0-511-54540-5. URL: <https://doi.org/10.1017/CBO9780511545405> (visited on 07/25/2022).
- [29] Mohammadkazem Tarzamni, Ali Kiani Nazarlou, and Jamil Abdolmohammadi. "MRI IMAGING AND PANCREATIC DISEASES". In: *Acta healthmedica* 1 (Mar. 2016), pp. 8–22. DOI: 10.19082/ah8.
- [30] Ahmed Abdrabou. *Diffusion tensor imaging and fiber tractography / Radiology Reference Article / Radiopaedia.org*. en-US. DOI: 10.53347/rID-22702. URL: <https://radiopaedia.org/articles/diffusion-tensor-imaging-and-fibre-tractography?lang=us> (visited on 07/28/2022).
- [31] Wim Van Hecke, Louise Emsell, and Stefan Sunaert, eds. *Diffusion Tensor Imaging*. en. New York, NY: Springer New York, 2016. ISBN: 978-1-4939-3117-0 978-1-4939-3118-7. DOI: 10.1007/978-1-4939-3118-7. URL: <http://link.springer.com/10.1007/978-1-4939-3118-7> (visited on 07/25/2022).
- [32] *DTI Scalars (FA, MD, AD, RD) - How do they relate to brain structure?* URL: <http://www.diffusion-imaging.com/2013/01/relation-between-neural-microstructure.html> (visited on 07/25/2022).
- [33] Hui Zhang et al. "NODDI: Practical in vivo neurite orientation dispersion and density imaging of the human brain". en. In: *NeuroImage* 61.4 (July 2012), pp. 1000–1016. ISSN: 10538119. DOI: 10.1016/j.neuroimage.2012.03.072. URL: <https://linkinghub.elsevier.com/retrieve/pii/S1053811912003539> (visited on 07/26/2022).
- [34] Maxime Descoteaux. "High Angular Resolution Diffusion Imaging (HARDI)". In: June 2015. DOI: 10.1002/047134608X.W8258.
- [35] Eleftherios Garyfallidis. "Eleftherios Garyfallidis, "Towards an accurate brain tractography", PhD thesis, University of Cambridge, 2012". PhD thesis. May 2012.
- [36] *Hypergeometric function*. en. Page Version ID: 1098981490. July 2022. URL: [https://en.wikipedia.org/w/index.php?title=Hypergeometric\\_function&oldid=1098981490](https://en.wikipedia.org/w/index.php?title=Hypergeometric_function&oldid=1098981490) (visited on 07/26/2022).
- [37] Arash Nazeri et al. "In Vivo Imaging of Gray Matter Microstructure in Major Psychiatric Disorders: Opportunities for Clinical Translation". en. In: *Biological Psychiatry: Cognitive Neuroscience and Neuroimaging* 5.9 (Sept. 2020), pp. 855–

864. ISSN: 2451-9022. DOI: 10.1016/j.bpsc.2020.03.003. URL: <https://www.sciencedirect.com/science/article/pii/S2451902220300720> (visited on 07/26/2022).
- [38] Benoit Scherrer et al. “Characterizing brain tissue by assessment of the distribution of anisotropic microstructural environments in diffusion-compartment imaging (DIAMOND): Characterizing Brain Tissue with DIAMOND”. en. In: *Magnetic Resonance in Medicine* 76.3 (Sept. 2016), pp. 963–977. ISSN: 07403194. DOI: 10.1002/mrm.25912. URL: <https://onlinelibrary.wiley.com/doi/10.1002/mrm.25912> (visited on 07/27/2022).
- [39] Gaëtan Rensonnet et al. “Towards microstructure fingerprinting: Estimation of tissue properties from a dictionary of Monte Carlo diffusion MRI simulations”. en. In: *NeuroImage* 184 (Jan. 2019), pp. 964–980. ISSN: 1053-8119. DOI: 10.1016/j.neuroimage.2018.09.076. URL: <https://www.sciencedirect.com/science/article/pii/S1053811918319487> (visited on 07/29/2022).
- [40] Gaetan Rensonnet. *Generation of a dictionary of DW-MRI signals from arbitrary brain microstructure configurations.* fr. Prom. : Macq, Benoît and Taquet, Maxime. Université catholique de Louvain, 2015.
- [41] Quentin Dessain and Mathieu Simon. *Development of an image processing pipeline for large-scale in vivo population studies of the brain microstructure.* fr. Prom. : Macq, Benoît. Université catholique de Louvain, 2021.
- [42] *Introduction to ElikoPy — ElikoPy documentation.* URL: <https://elikopy.readthedocs.io/en/latest/introduction.html> (visited on 07/28/2022).
- [43] *BIDS.* en-US. June 2022. URL: <https://bids.neuroimaging.io/index> (visited on 07/28/2022).
- [44] Kashif Iqbal. *DICOM - Digital Imaging and Communications File Format.* en-us. Oct. 2019. URL: <https://docs.fileformat.com/image/dicom/> (visited on 07/28/2022).
- [45] dfwg. *NIfTI: — Neuroimaging Informatics Technology Initiative.* en. Document. URL: <https://nifti.nimh.nih.gov/> (visited on 07/28/2022).
- [46] *DIPY - Diffusion Imaging In Python.* URL: <https://dipy.org/> (visited on 07/28/2022).
- [47] *Dmipy: Diffusion Microstructure Imaging in Python.* original-date: 2017-03-22T06:54:40Z. July 2022. URL: <https://github.com/AthenaEPI/dmipy> (visited on 07/28/2022).
- [48] *FSL - FslWiki.* URL: <https://fsl.fmrib.ox.ac.uk/fsl/fslwiki> (visited on 07/28/2022).
- [49] *FreeSurfer.* en. URL: <https://surfer.nmr.mgh.harvard.edu> (visited on 07/28/2022).
- [50] Brian Avants, Nick Tustison, and Gang Song. “Advanced normalization tools (ANTS)”. In: *Insight J* 1–35 (Nov. 2008). DOI: 10.54294/uvnhin.
- [51] *ITK Tools.* original-date: 2011-04-14T13:06:50Z. June 2022. URL: <https://github.com/ITKTools/ITKTools> (visited on 07/28/2022).
- [52] J-Donald Tournier et al. “MRtrix3: A fast, flexible and open software framework for medical image processing and visualisation”. en. In: *NeuroImage* 202 (Nov. 2019), p. 116137. ISSN: 1053-8119. DOI: 10.1016/j.neuroimage.2019.

116137. URL: <https://www.sciencedirect.com/science/article/pii/S1053811919307281> (visited on 07/29/2022).
- [53] Diji Kuriakose and Zhicheng Xiao. "Pathophysiology and Treatment of Stroke: Present Status and Future Perspectives". In: *International Journal of Molecular Sciences* 21.20 (Oct. 2020), p. 7609. ISSN: 1422-0067. DOI: 10.3390/ijms21207609. URL: <https://www.ncbi.nlm.nih.gov/pmc/articles/PMC7589849/> (visited on 07/29/2022).
- [54] Meaghan Roy-O'Reilly and Louise D. McCullough. "Age and Sex Are Critical Factors in Ischemic Stroke Pathology". eng. In: *Endocrinology* 159.8 (Aug. 2018), pp. 3120–3131. ISSN: 1945-7170. DOI: 10.1210/en.2018-00465.
- [55] Graeme J Hankey. "Stroke". en. In: *The Lancet* 389.10069 (Feb. 2017), pp. 641–654. ISSN: 01406736. DOI: 10.1016/S0140-6736(16)30962-X. URL: <https://linkinghub.elsevier.com/retrieve/pii/S014067361630962X> (visited on 07/29/2022).
- [56] James C. Grotta et al. *Stroke: Pathophysiology, Diagnosis, and Management*. English (US). Elsevier Inc., Jan. 2015. ISBN: 9780323295444.
- [57] *Arteriosclerosis / atherosclerosis - Symptoms and causes*. en. URL: <https://www.mayoclinic.org/diseases-conditions/arteriosclerosis-atherosclerosis/symptoms-causes/syc-20350569> (visited on 07/30/2022).
- [58] *Cerebral Aneurysm – Symptoms, Diagnosis and Treatments*. en. URL: <https://www.aans.org/> (visited on 07/30/2022).
- [59] *Symptoms of stroke*. en. Dec. 2014. URL: <https://www.stroke.org.uk/what-is-stroke/what-are-the-symptoms-of-stroke> (visited on 07/30/2022).
- [60] Azlisham Mohd Nor et al. "The Recognition of Stroke in the Emergency Room (ROSIER) scale: development and validation of a stroke recognition instrument". eng. In: *The Lancet. Neurology* 4.11 (Nov. 2005), pp. 727–734. ISSN: 1474-4422. DOI: 10.1016/S1474-4422(05)70201-5.
- [61] Martin J. O'Donnell et al. "Risk factors for ischaemic and intracerebral haemorrhagic stroke in 22 countries (the INTERSTROKE study): a case-control study". eng. In: *Lancet (London, England)* 376.9735 (July 2010), pp. 112–123. ISSN: 1474-547X. DOI: 10.1016/S0140-6736(10)60834-3.
- [62] R. Collins et al. "Blood pressure, stroke, and coronary heart disease. Part 2, Short-term reductions in blood pressure: overview of randomised drug trials in their epidemiological context". eng. In: *Lancet (London, England)* 335.8693 (Apr. 1990), pp. 827–838. ISSN: 0140-6736. DOI: 10.1016/0140-6736(90)90944-z.
- [63] Chirantan Banerjee et al. "Duration of Diabetes and Risk of Ischemic Stroke: The Northern Manhattan Study". In: *Stroke; a Journal of Cerebral Circulation* 43.5 (May 2012), pp. 1212–1217. ISSN: 0039-2499. DOI: 10.1161/STROKEAHA.111.641381. URL: <https://www.ncbi.nlm.nih.gov/pmc/articles/PMC3336044/> (visited on 07/30/2022).
- [64] P. A. Wolf, R. D. Abbott, and W. B. Kannel. "Atrial fibrillation as an independent risk factor for stroke: the Framingham Study". eng. In: *Stroke* 22.8 (Aug. 1991), pp. 983–988. ISSN: 0039-2499. DOI: 10.1161/01.str.22.8.983.

- [65] Licia Denti et al. "The role of lipid profile in determining the risk of ischemic stroke in the elderly: a case-control study". eng. In: *Archives of Gerontology and Geriatrics* 37.1 (Aug. 2003), pp. 51–62. ISSN: 0167-4943. DOI: 10.1016/s0167-4943(03)00020-7.
- [66] A. L. Klatsky et al. "Alcohol drinking and risk of hospitalization for ischemic stroke". eng. In: *The American Journal of Cardiology* 88.6 (Sept. 2001), pp. 703–706. ISSN: 0002-9149. DOI: 10.1016/s0002-9149(01)01824-0.
- [67] Katherine Esse et al. "Epidemic of illicit drug use, mechanisms of action/addiction and stroke as a health hazard". In: *Brain and Behavior* 1.1 (Sept. 2011), pp. 44–54. ISSN: 2162-3279. DOI: 10.1002/brb3.7. URL: <https://www.ncbi.nlm.nih.gov/pmc/articles/PMC3217673/> (visited on 07/30/2022).
- [68] Viveca M. Bhat et al. "Dose-Response Relationship Between Cigarette Smoking and Risk of Ischemic Stroke in Young Women". In: *Stroke; a journal of cerebral circulation* 39.9 (Sept. 2008), pp. 2439–2443. ISSN: 0039-2499. DOI: 10.1161/STROKEAHA.107.510073. URL: <https://www.ncbi.nlm.nih.gov/pmc/articles/PMC3564048/> (visited on 07/30/2022).
- [69] Meng-Liang Zhou et al. "The inflammation in the gut after experimental subarachnoid hemorrhage". eng. In: *The Journal of Surgical Research* 137.1 (Jan. 2007), pp. 103–108. ISSN: 0022-4804. DOI: 10.1016/j.jss.2006.06.023.
- [70] *Stroke rehabilitation / Elsevier Enhanced Reader*. en. DOI: 10.1016/S0140-6736(11)60325-5. URL: <https://reader.elsevier.com/reader/sd/pii> (visited on 07/30/2022).
- [71] *HABIT-ILE*. fr. URL: <https://www.leneurogroupe.org/bimanuelle-intensive-habitive> (visited on 07/31/2022).
- [72] Yannick Bleyenheuft and Andrew M. Gordon. "Hand-Arm Bimanual Intensive Therapy Including Lower Extremities (HABIT-ILE) for Children with Cerebral Palsy". en. In: *Physical & Occupational Therapy In Pediatrics* 34.4 (Nov. 2014), pp. 390–403. ISSN: 0194-2638, 1541-3144. DOI: 10.3109/01942638.2014.932884. URL: <http://www.tandfonline.com/doi/full/10.3109/01942638.2014.932884> (visited on 07/31/2022).
- [73] Geoffroy Saussez et al. "Including a Lower-Extremity Component during Hand-Arm Bimanual Intensive Training does not Attenuate Improvements of the Upper Extremities: A Retrospective Study of Randomized Trials". In: *Frontiers in Neurology* 8 (2017).
- [74] Rita Alves et al. "Correlation Tensor MRI deciphers underlying kurtosis sources in stroke". In: *NeuroImage* 247 (2022), p. 118833. ISSN: 1053-8119. DOI: <https://doi.org/10.1016/j.neuroimage.2021.118833>. URL: <https://www.sciencedirect.com/science/article/pii/S1053811921011046>.
- [75] *14.3 Motor Responses - Anatomy and Physiology / OpenStax*. URL: <https://openstax.org/books/anatomy-and-physiology/pages/14-3-motor-responses?query=corticospinal&target=%5C%7B> (visited on 07/31/2022).
- [76] Adriana L. Natali, Vamsi Reddy, and Bruno Bordoni. "Neuroanatomy, Corticospinal Cord Tract". eng. In: *StatPearls*. Treasure Island (FL): StatPearls Pub-

- lishing, 2022. URL: <http://www.ncbi.nlm.nih.gov/books/NBK535423/> (visited on 07/31/2022).
- [77] *Corticospinal Tract*. en. URL: [https://www.physio-pedia.com/Corticospinal\\_Tract](https://www.physio-pedia.com/Corticospinal_Tract) (visited on 07/31/2022).
- [78] *Corpus callosum*. en. URL: <https://www.kenhub.com/en/library/anatomy/corpus-callosum> (visited on 08/09/2022).
- [79] Melody N. Grohs et al. “Corpus callosum microstructure is associated with motor function in preschool children”. en. In: *NeuroImage* 183 (Dec. 2018), pp. 828–835. ISSN: 1053-8119. DOI: 10.1016/j.neuroimage.2018.09.004. URL: <https://www.sciencedirect.com/science/article/pii/S1053811918307778> (visited on 08/09/2022).
- [80] Firdaus Fabrice Hannanu et al. “White matter tract disruption is associated with ipsilateral hand impairment in subacute stroke: a diffusion MRI study”. en. In: *Neuroradiology* 64.8 (Aug. 2022), pp. 1605–1615. ISSN: 0028-3940, 1432-1920. DOI: 10.1007/s00234-022-02927-8. URL: <https://link.springer.com/10.1007/s00234-022-02927-8> (visited on 08/07/2022).
- [81] *Cerebellum: Anatomy, function, and disorders*. en. Aug. 2018. URL: <https://www.medicalnewstoday.com/articles/313265> (visited on 08/09/2022).
- [82] Anne Lingford-Hughes and Nicola Kalk. “2 - Clinical neuroanatomy”. en. In: *Core Psychiatry (Third Edition)*. Ed. by Pádraig Wright, Julian Stern, and Michael Phelan. Oxford: W.B. Saunders, Jan. 2012, pp. 13–34. ISBN: 978-0-7020-3397-1. DOI: 10.1016/B978-0-7020-3397-1.00002-1. URL: <https://www.sciencedirect.com/science/article/pii/B9780702033971000021> (visited on 08/09/2022).
- [83] Byron Bernal and Nolan Altman. “The connectivity of the superior longitudinal fasciculus: a tractography DTI study”. en. In: *Magnetic Resonance Imaging* 28.2 (Feb. 2010), pp. 217–225. ISSN: 0730-725X. DOI: 10.1016/j.mri.2009.07.008. URL: <https://www.sciencedirect.com/science/article/pii/S0730725X09001672> (visited on 08/09/2022).
- [84] Nikos Makris et al. “Segmentation of Subcomponents within the Superior Longitudinal Fascicle in Humans: A Quantitative, In Vivo, DT-MRI Study”. In: *Cerebral Cortex* 15.6 (June 2005), pp. 854–869. ISSN: 1047-3211. DOI: 10.1093/cercor/bhh186. URL: <https://doi.org/10.1093/cercor/bhh186> (visited on 08/09/2022).
- [85] Robert Lindenberg et al. “Predicting functional motor potential in chronic stroke patients using diffusion tensor imaging”. In: *Human Brain Mapping* 33.5 (2012). \_eprint: <https://onlinelibrary.wiley.com/doi/pdf/10.1002/hbm.21266>, pp. 1040–1051. DOI: <https://doi.org/10.1002/hbm.21266>. URL: <https://onlinelibrary.wiley.com/doi/abs/10.1002/hbm.21266>.
- [86] T. Rüber, G. Schlaug, and R. Lindenberg. “Compensatory role of the cortico-rubro-spinal tract in motor recovery after stroke”. English. In: *Neurology* 79.6 (2012), pp. 515–522. ISSN: 0028-3878. DOI: 10.1212/WNL.0b013e31826356e8.
- [87] Tetsuo Koyama et al. “Relationship between diffusion tensor fractional anisotropy and long-term motor outcome in patients with hemiparesis after middle cerebral

- artery infarction". eng. In: *Journal of Stroke and Cerebrovascular Diseases: The Official Journal of National Stroke Association* 23.9 (Oct. 2014), pp. 2397–2404. ISSN: 1532-8511. DOI: 10.1016/j.jstrokecerebrovasdis.2014.05.017.
- [88] Benjamin N. Groisser et al. "Corticospinal Tract Diffusion Abnormalities Early after Stroke Predict Motor Outcome". In: *Neurorehabilitation and neural repair* 28.8 (Oct. 2014), pp. 751–760. ISSN: 1545-9683. DOI: 10.1177/1545968314521896. URL: <https://www.ncbi.nlm.nih.gov/pmc/articles/PMC4128905/> (visited on 08/06/2022).
- [89] Gowri Jayaram et al. "Relationships between functional and structural corticospinal tract integrity and walking post stroke". eng. In: *Clinical Neurophysiology: Official Journal of the International Federation of Clinical Neurophysiology* 123.12 (Dec. 2012), pp. 2422–2428. ISSN: 1872-8952. DOI: 10.1016/j.clinph.2012.04.026.
- [90] Chang-Hyun Park et al. "Assessing a standardised approach to measuring corticospinal integrity after stroke with DTI". In: *NeuroImage : clinical* 2 (Apr. 2013), pp. 521–33. DOI: 10.1016/j.nicl.2013.04.002.
- [91] Jie Song et al. "DTI measures track and predict motor function outcomes in stroke rehabilitation utilizing BCI technology". In: *Frontiers in Human Neuroscience* 9 (Apr. 2015), p. 195. ISSN: 1662-5161. DOI: 10.3389/fnhum.2015.00195. URL: <https://www.ncbi.nlm.nih.gov/pmc/articles/PMC4410488/> (visited on 08/06/2022).
- [92] Ying Wei et al. "Widespread White Matter Microstructure Alterations Based on Diffusion Tensor Imaging and Diffusion Kurtosis Imaging in Patients With Pontine Infarction". en. In: *Frontiers in Aging Neuroscience* 13 (Dec. 2021), p. 758236. ISSN: 1663-4365. DOI: 10.3389/fnagi.2021.758236. URL: <https://www.frontiersin.org/articles/10.3389/fnagi.2021.758236/full> (visited on 08/07/2022).
- [93] Ganesh Adluru et al. "Assessment of white matter microstructure in stroke patients using NODDI". In: *2014 36th Annual International Conference of the IEEE Engineering in Medicine and Biology Society*. Chicago, IL: IEEE, Aug. 2014, pp. 742–745. ISBN: 978-1-4244-7929-0. DOI: 10.1109/EMBC.2014.6943697. URL: <http://ieeexplore.ieee.org/document/6943697/> (visited on 08/07/2022).
- [94] Zhenxiong Wang et al. "A study of neurite orientation dispersion and density imaging in ischemic stroke". eng. In: *Magnetic Resonance Imaging* 57 (Apr. 2019), pp. 28–33. ISSN: 1873-5894. DOI: 10.1016/j.mri.2018.10.018.
- [95] Edward S. Hui et al. "Stroke Assessment With Diffusional Kurtosis Imaging". In: *Stroke* 43.11 (Nov. 2012). Publisher: American Heart Association, pp. 2968–2973. DOI: 10.1161/STROKEAHA.112.657742. URL: <https://www.ahajournals.org/doi/10.1161/STROKEAHA.112.657742> (visited on 08/07/2022).
- [96] Philipp Koch, Robert Schulz, and Friedhelm C. Hummel. "Structural connectivity analyses in motor recovery research after stroke". In: *Annals of Clinical and Translational Neurology* 3.3 (Jan. 2016), pp. 233–244. ISSN: 2328-9503. DOI: 10.1002/acn3.278. URL: <https://www.ncbi.nlm.nih.gov/pmc/articles/PMC4774263/> (visited on 08/08/2022).

- [97] Tory O. Frizzell et al. "Imaging functional neuroplasticity in human white matter tracts". en. In: *Brain Structure and Function* 227.1 (Jan. 2022), pp. 381–392. ISSN: 1863-2653, 1863-2661. DOI: 10.1007/s00429-021-02407-4. URL: <https://link.springer.com/10.1007/s00429-021-02407-4> (visited on 08/08/2022).
- [98] Philipp J Koch et al. "The structural connectome and motor recovery after stroke: predicting natural recovery". en. In: *Brain* 144.7 (Aug. 2021), pp. 2107–2119. ISSN: 0006-8950, 1460-2156. DOI: 10.1093/brain/awab082. URL: <https://academic.oup.com/brain/article/144/7/2107/6316639> (visited on 08/08/2022).
- [99] Annick Van Gils et al. "The Adult Assisting Hand Assessment Stroke: Psychometric Properties of an Observation-Based Bimanual Upper Limb Performance Measurement". en. In: *Archives of Physical Medicine and Rehabilitation* 99.12 (Dec. 2018), pp. 2513–2522. ISSN: 00039993. DOI: 10.1016/j.apmr.2018.04.025. URL: <https://linkinghub.elsevier.com/retrieve/pii/S0003999318303125> (visited on 08/05/2022).
- [100] Massimo Penta et al. "The ABILHAND Questionnaire as a Measure of Manual Ability in Chronic Stroke Patients". In: *Stroke* 32.7 (July 2001). Publisher: American Heart Association, pp. 1627–1634. DOI: 10.1161/01.STR.32.7.1627. URL: <https://www.ahajournals.org/doi/full/10.1161/01.STR.32.7.1627> (visited on 08/05/2022).
- [101] Charles Sébiyo Batcho, Alan Tennant, and Jean-Louis Thonnard. "ACTIVLIM-Stroke: A Crosscultural Rasch-Built Scale of Activity Limitations in Patients With Stroke". In: *Stroke* 43.3 (Mar. 2012). Publisher: American Heart Association, pp. 815–823. DOI: 10.1161/STROKEAHA.111.638965. URL: <https://www.ahajournals.org/doi/10.1161/STROKEAHA.111.638965> (visited on 08/05/2022).
- [102] Pamela W Duncan et al. "Rasch analysis of a new stroke-specific outcome scale: the stroke impact scale11No commercial party having a direct financial interest in the results of the research supporting this article has or will confer a benefit upon the author(s) or upon any organization with which the author(s) is/are associated." en. In: *Archives of Physical Medicine and Rehabilitation* 84.7 (July 2003), pp. 950–963. ISSN: 0003-9993. DOI: 10.1016/S0003-9993(03)00035-2. URL: <https://www.sciencedirect.com/science/article/pii/S0003999303000352> (visited on 08/05/2022).
- [103] Jamie L. Banks and Charles A. Marotta. "Outcomes Validity and Reliability of the Modified Rankin Scale: Implications for Stroke Clinical Trials". In: *Stroke* 38.3 (Mar. 2007). Publisher: American Heart Association, pp. 1091–1096. DOI: 10.1161/01.STR.0000258355.23810.c6. URL: <https://www.ahajournals.org/doi/full/10.1161/01.STR.0000258355.23810.c6> (visited on 08/05/2022).
- [104] Mary Law et al. "The Canadian Occupational Performance Measure: An Outcome Measure for Occupational Therapy". en. In: *Canadian Journal of Occupational Therapy* 57.2 (Apr. 1990). Publisher: SAGE Publications Inc, pp. 82–87.

- ISSN: 0008-4174. DOI: 10.1177/000841749005700207. URL: <https://doi.org/10.1177/000841749005700207> (visited on 08/05/2022).
- [105] *Dextrain*. en. URL: <https://www.dextrain.com/> (visited on 08/05/2022).
- [106] *REApalan®*. en-US. URL: <https://www.axinesis.com/en/our-solutions/reaplan/> (visited on 08/05/2022).
- [107] A. R. Fugl-Meyer et al. “The post-stroke hemiplegic patient. 1. a method for evaluation of physical performance”. eng. In: *Scandinavian Journal of Rehabilitation Medicine* 7.1 (1975), pp. 13–31. ISSN: 0036-5505.
- [108] *Box and Block Test*. en. URL: [https://www.physio-pedia.com/Box\\_and\\_Block\\_Test](https://www.physio-pedia.com/Box_and_Block_Test) (visited on 08/05/2022).
- [109] S. L. Wolf et al. “Assessing Wolf motor function test as outcome measure for research in patients after stroke”. eng. In: *Stroke* 32.7 (July 2001), pp. 1635–1639. ISSN: 1524-4628. DOI: 10.1161/01.str.32.7.1635.
- [110] *Six Minute Walk Test / 6 Minute Walk Test*. en. URL: [https://www.physio-pedia.com/Six\\_Minute\\_Walk\\_Test/\\_/6\\_Minute\\_Walk\\_Test](https://www.physio-pedia.com/Six_Minute_Walk_Test/_/6_Minute_Walk_Test) (visited on 08/05/2022).
- [111] Arne Gramstad, Dag Aarsland, and Halvor Naess. “Cognitive Profile of Elderly Patients with Mild Stroke”. In: *Dementia and Geriatric Cognitive Disorders EX-TRA* 1.1 (Nov. 2011), pp. 409–417. ISSN: 1664-5464. DOI: 10.1159/000331675. URL: <https://www.ncbi.nlm.nih.gov/pmc/articles/PMC3243639/> (visited on 08/05/2022).
- [112] Emma A. Climie and Kristin Rostad. “Test Review: Wechsler Adult Intelligence Scale”. In: *Journal of Psychoeducational Assessment* 29.6 (2011), pp. 581–586. DOI: 10.1177/0734282911408707. URL: <https://doi.org/10.1177/0734282911408707>.
- [113] Judith Jaeger. “Digit Symbol Substitution Test”. In: *Journal of Clinical Psychopharmacology* 38.5 (Oct. 2018), pp. 513–519. DOI: 10.1097/JCP.0000000000000941. URL: <https://www.ncbi.nlm.nih.gov/pmc/articles/PMC6291255/> (visited on 08/05/2022).
- [114] Roy P. C. Kessels et al. “The Corsi Block-Tapping Task: Standardization and Normative Data”. en. In: *Applied Neuropsychology* 7.4 (Dec. 2000), pp. 252–258. ISSN: 0908-4282, 1532-4826. DOI: 10.1207/S15324826AN0704\_8. URL: [http://www.tandfonline.com/doi/abs/10.1207/S15324826AN0704\\_8](http://www.tandfonline.com/doi/abs/10.1207/S15324826AN0704_8) (visited on 08/05/2022).
- [115] Silvio Cesar Escovar Paiva et al. “Bells Test: Are there differences in performance between adult groups aged 40-59 and 60-75?” In: *Dementia & Neuropsychologia* 11.1 (2017), pp. 40–47. ISSN: 1980-5764. DOI: 10.1590/1980-57642016dn11-010007. URL: <https://www.ncbi.nlm.nih.gov/pmc/articles/PMC5619213/> (visited on 08/05/2022).
- [116] *Trail Making Test (TMT) – Strokengine*. en-US. URL: <https://strokengine.ca/en/assessments/trail-making-test-tmt/> (visited on 08/05/2022).
- [117] Parunyou Julayanont and Ziad S. Nasreddine. “Montreal Cognitive Assessment (MoCA): Concept and Clinical Review”. en. In: *Cognitive Screening Instruments: A Practical Approach*. Ed. by A. J. Larner. Cham: Springer International Pub-

- lishing, 2017, pp. 139–195. ISBN: 978-3-319-44775-9. DOI: 10.1007/978-3-319-44775-9\_7. URL: [https://doi.org/10.1007/978-3-319-44775-9\\_7](https://doi.org/10.1007/978-3-319-44775-9_7) (visited on 08/05/2022).
- [118] Fahd R. Khan and Jaimie M. Henderson. “Chapter 3 - Deep brain stimulation surgical techniques”. In: *Brain Stimulation*. Ed. by Andres M. Lozano and Mark Hallett. Vol. 116. Handbook of Clinical Neurology. ISSN: 0072-9752. Elsevier, 2013, pp. 27–37. DOI: <https://doi.org/10.1016/B978-0-444-53497-2.00003-6>. URL: <https://www.sciencedirect.com/science/article/pii/B9780444534972000036>.
- [119] *Templates and Atlases included with FSL*. URL: <https://fsl.fmrib.ox.ac.uk/fsl/fslwiki/Atlases> (visited on 08/02/2022).
- [120] J. Diedrichsen et al. “Imaging the deep cerebellar nuclei: a probabilistic atlas and normalization procedure”. eng. In: *NeuroImage* 54.3 (Feb. 2011), pp. 1786–1794. ISSN: 1095-9572. DOI: 10.1016/j.neuroimage.2010.10.035.
- [121] Rahul S. Desikan et al. “An automated labeling system for subdividing the human cerebral cortex on MRI scans into gyral based regions of interest”. eng. In: *NeuroImage* 31.3 (July 2006), pp. 968–980. ISSN: 1053-8119. DOI: 10.1016/j.neuroimage.2006.01.021.
- [122] *Home - Research Imaging Institute*. URL: <https://wp.uthscsa.edu/rii/> (visited on 08/02/2022).
- [123] Shaun Warrington et al. “XTRACT - Standardised protocols for automated tractography in the human and macaque brain”. In: *NeuroImage* 217 (2020), p. 116923. ISSN: 1053-8119. DOI: <https://doi.org/10.1016/j.neuroimage.2020.116923>. URL: <https://www.sciencedirect.com/science/article/pii/S1053811920304092>.
- [124] *DIPY - Tutorials*. URL: <https://dipy.org/> (visited on 08/02/2022).
- [125] B. B. Avants et al. “Symmetric diffeomorphic image registration with cross-correlation: evaluating automated labeling of elderly and neurodegenerative brain”. eng. In: *Medical Image Analysis* 12.1 (Feb. 2008), pp. 26–41. ISSN: 1361-8423. DOI: 10.1016/j.media.2007.06.004.
- [126] Ka Chun Lam and Lok Ming Lui. “Landmark and Intensity Based Registration with Large Deformations via Quasi-conformal Maps”. In: *SIAM Journal on Imaging Sciences* 7 (Oct. 2013). DOI: 10.1137/130943406.
- [127] Ajitesh Kumar. *Two independent samples t-tests: Formula & Examples*. en-US. Jan. 2022. URL: <https://vitalflux.com/two-sample-t-test-formula-examples/> (visited on 08/07/2022).
- [128] Alfonso Mastropietro et al. “Microstructural characterization of corticospinal tract in subacute and chronic stroke patients with distal lesions by means of advanced diffusion MRI”. In: *Neuroradiology* 61.9 (2019), pp. 1033–1045. ISSN: 0028-3940. DOI: 10.1007/s00234-019-02249-2. URL: <https://www.ncbi.nlm.nih.gov/pmc/articles/PMC6689031/> (visited on 08/12/2022).
- [129] *Spherical-deconvolution Informed Filtering of Tractograms (SIFT) — MRtrix 3.0 documentation*. URL: [https://mrtrix.readthedocs.io/en/dev/quantitative\\_structural\\_connectivity/sift.html](https://mrtrix.readthedocs.io/en/dev/quantitative_structural_connectivity/sift.html) (visited on 08/15/2022).

- [130] Demian Wassermann et al. “The white matter query language: a novel approach for describing human white matter anatomy”. en. In: *Brain Structure and Function* 221.9 (Dec. 2016), pp. 4705–4721. ISSN: 1863-2661. DOI: 10.1007/s00429-015-1179-4. URL: <https://doi.org/10.1007/s00429-015-1179-4> (visited on 08/17/2022).
- [131] Michael Bach et al. “Methodological considerations on tract-based spatial statistics (TBSS)”. en. In: *NeuroImage* 100 (Oct. 2014), pp. 358–369. ISSN: 1053-8119. DOI: 10.1016/j.neuroimage.2014.06.021. URL: <https://www.sciencedirect.com/science/article/pii/S1053811914004984> (visited on 08/16/2022).
- [132] *FreeSurferWiki - Free Surfer Wiki*. URL: <https://surfer.nmr.mgh.harvard.edu/fswiki/FreeSurferWiki> (visited on 08/17/2022).
- [133] *FSL - FslWiki*. URL: <https://fsl.fmrib.ox.ac.uk/fsl/fslwiki> (visited on 08/15/2022).
- [134] *ATLAS MAPS*. en. URL: <https://www.natbrainlab.co.uk/atlas-maps> (visited on 08/16/2022).
- [135] *Relaxation time, T<sub>1</sub>, T<sub>2</sub>*. en. URL: <http://mriquestions.com/why-is-t1--t2.html> (visited on 07/07/2022).

# APPENDIX A

## DTI ADDITIONAL RESULTS

This appendix contains the boxplots of the DTI metrics in the Cortico Ponto Cerebellum (CPC), Inferior Cerebellar Pedunculus (iCP), Superior Cerebellar Pedunculus (sCP), Middle Cerebellar Pendunculus (mCP) and Superior Longitudinal Fasciculus I (SLF I).

### A.1 Fractional Anisotropy

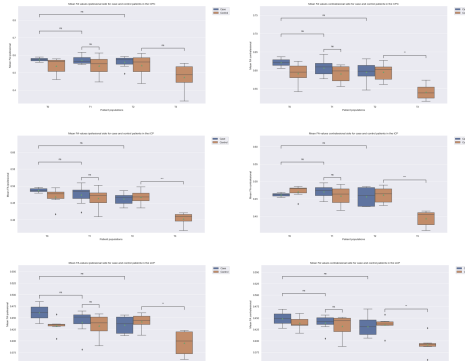


Figure A.1: Fractional Anisotropy (FA) boxplots in the Cortico Ponto Cerebellum (CPC), Inferior Cerebellar Pedunculus (iCP) and Superior Cerebellar Pedunculus (sCP) for both patient populations

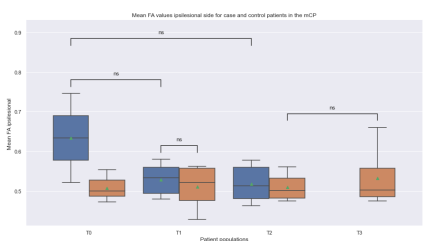


Figure A.2: Fractional Anisotropy (FA) boxplots in the Middle Cerebellar Pedunculus (mCP) on the ipsi- and contralesional sides for both patient populations

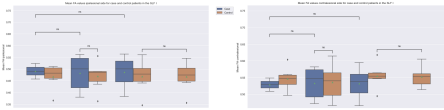


Figure A.3: Fractional Anisotropy (FA) boxplots in the Superior Longitudinal Fasciculus I (SLF I) on the ipsi- and contralesional sides for both patient populations

## A.2 Mean Diffusivity

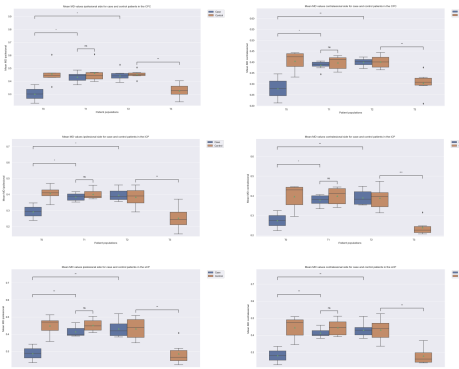


Figure A.4: Mean Diffusivity (MD) boxplots in the Cortico Ponto Cerebellum (CPC), Inferior Cerebellar Pedunculus (iCP) and Superior Cerebellar Pedunculus (sCP) on the ipsi- and contralesional sides for both patient populations

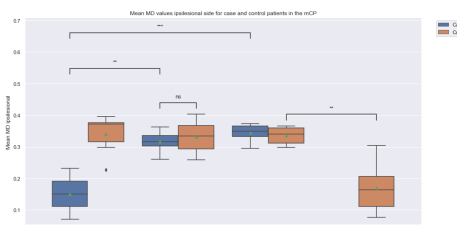


Figure A.5: Mean Diffusivity (MD) boxplots in the Middle Cerebellar Pedunculus (mCP) for both patient populations

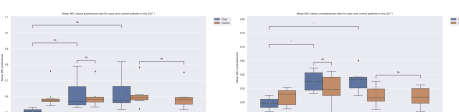


Figure A.6: Mean Diffusivity (MD) boxplots in the Superior Longitudinal Fasciculus I (SLF I) on the ipsi- and contralesional sides for both patient populations

### A.3 Axial Diffusivity

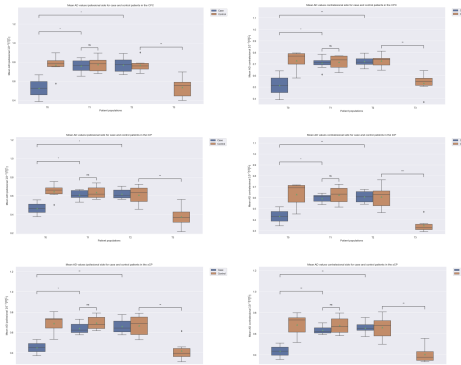


Figure A.7: Axial Diffusivity (AD) boxplots in the Cortico Ponto Cerebellum (CPC), Inferior Cerebellar Pedunculus (iCP) and Superior Cerebellar Pedunculus (sCP) on the ipsi- and contralesional sides for both patient populations

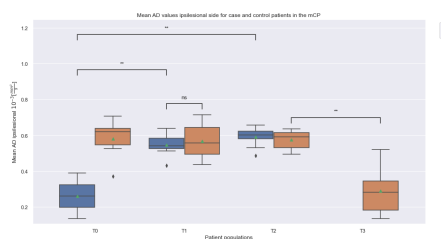


Figure A.8: Axial Diffusivity (AD) boxplots in the Middle Cerebellar Pedunculus (mCP) for both patient populations

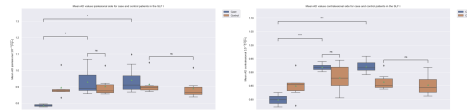


Figure A.9: Axial Diffusivity (AD) boxplots in the Superior Longitudinal Fasciculus I (SLF I) on the ipsi- and contralesional sides for both patient populations

## A.4 Radial Diffusivity

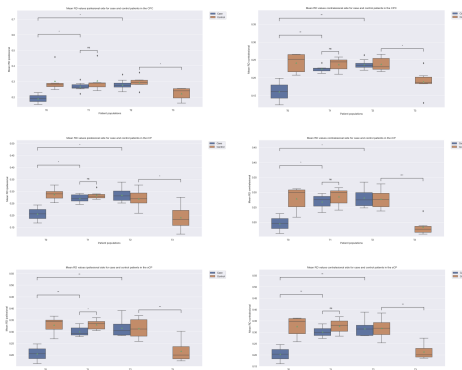


Figure A.10: Radial Diffusivity (RD) boxplots in the Cortico Ponto Cerebellum (CPC), Inferior Cerebellar Pedunculus (iCP) and Superior Cerebellar Pedunculus (sCP) on the ipsi- and contralesional sides for both patient populations

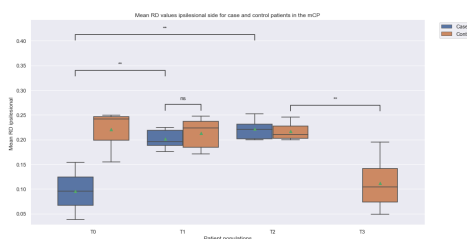


Figure A.11: Radial Diffusivity (RD) boxplots in the Middle Cerebellar Pedunculus (mCP) for both patient populations

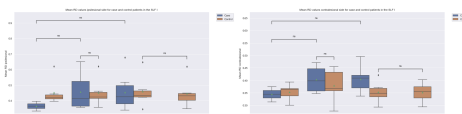


Figure A.12: Radial Diffusivity (RD) boxplots in the Superior Longitudinal Fasciculus I (SLF I) on the ipsi- and contralesional sides for both patient populations

## APPENDIX B

### NODDI ADDITIONAL RESULTS

This appendix contains the boxplots of the NODDI metrics in the Cortico Ponto Cerebellum (CPC), Inferior Cerebellar Pedunculus (iCP), Superior Cerebellar Pedunculus (sCP), Middle Cerebellar Pendunculus (mCP) and Superior Longitudinal Fasciculus I (SLF I).

#### B.1 Fiber Orientation Dispersion Index

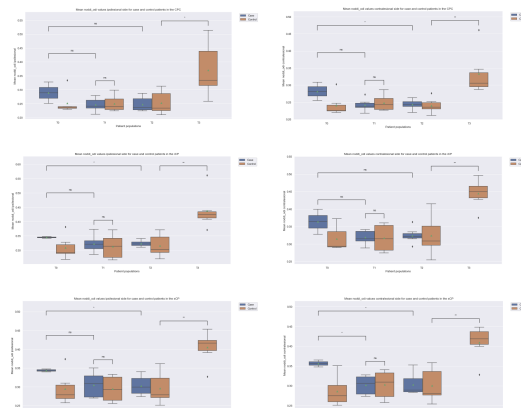


Figure B.1: Fiber Orientation Dispersion Index (ODI) boxplots in the Cortico Ponto Cerebellum (CPC), Inferior Cerebellar Pedunculus (iCP) and Superior Cerebellar Pedunculus (sCP) on the ipsi- and contralesional sides for both patient populations

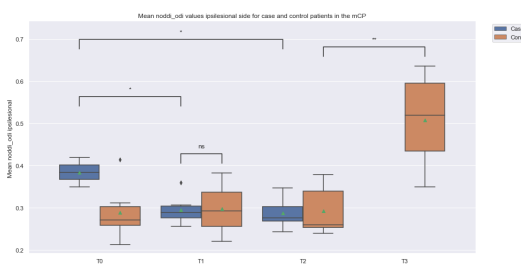


Figure B.2: Fiber Orientation Dispersion Index (ODI) boxplots in the Middle Cerebellar Pedunculus (mCP) on the ipsi- and contralesional sides for both patient populations

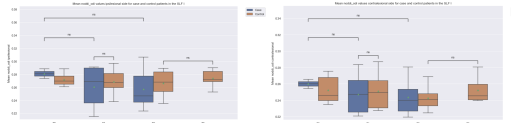


Figure B.3: Fiber Orientation Dispersion Index (ODI) boxplots in the Superior Longitudinal Fasciculus I (SLF I) on the ipsi- and contralesional sides for both patient populations

## B.2 Extracellular Volume Fraction

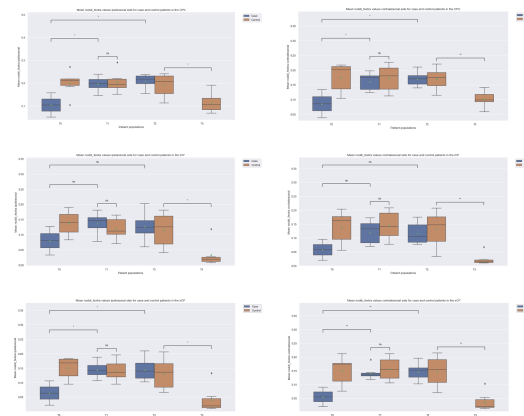


Figure B.4: Extracellular volume fraction ( $f_{extra}$ ) boxplots in the Cortico Ponto Cerebellum (CPC), Inferior Cerebellar Pedunculus (iCP) and Superior Cerebellar Pedunculus (sCP) on the ipsi- and contralesional sides for both patient populations

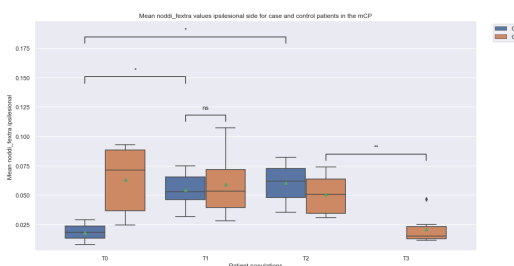


Figure B.5: Extracellular volume fraction ( $f_{extra}$ ) boxplots in the Middle Cerebellar Pedunculus (mCP) for both patient populations

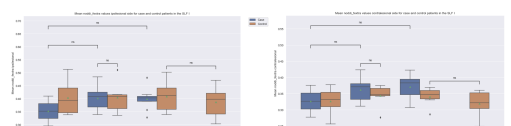


Figure B.6: Extracellular volume fraction ( $f_{extra}$ ) boxplots in the Superior Longitudinal Fasciculus I (SLF I) on the ipsi- and contralesional sides for both patient populations

### B.3 Intracellular Volume Fraction

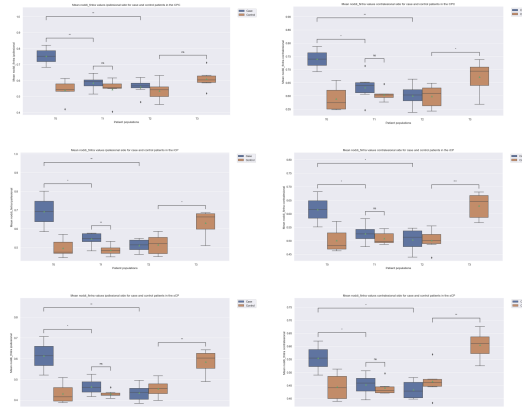


Figure B.7: Intracelullar volume fraction ( $f_{intra}$ ) boxplots in the Cortico Ponto Cerebellum (CPC), Inferior Cerebellar Pedunculus (iCP) and Superior Cerebellar Pedunculus (sCP) on the ipsi- and contralesional sides for both patient populations

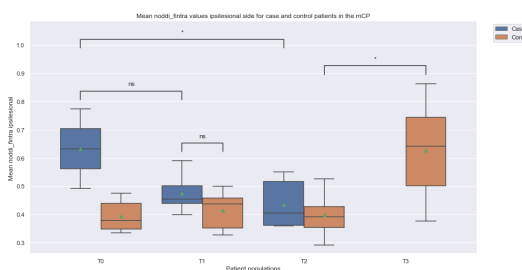


Figure B.8: Intracelullar volume fraction ( $f_{intra}$ ) boxplots in the Middle Cerebellar Pedunculus (mCP) for both patient populations

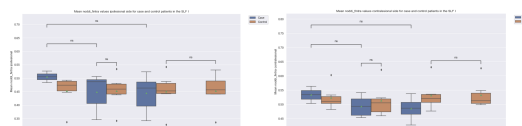


Figure B.9: Intracelullar volume fraction ( $f_{intra}$ ) boxplots in the Superior Longitudinal Fasiculus I (SLF I) on the ipsi- and contralesional sides for both patient populations

## B.4 Free Water Volume Fraction

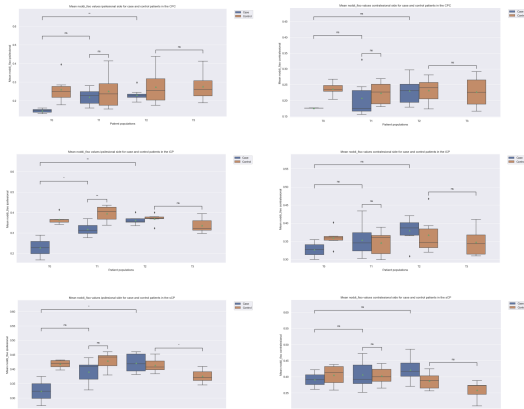


Figure B.10: Free water volume fraction ( $f_{\text{iso}}$ ) boxplots in the Cortico Ponto Cerebellum (CPC), Inferior Cerebellar Pedunculus (iCP) and Superior Cerebellar Pedunculus (sCP) on the ipsi- and contralesional sides for both patient populations

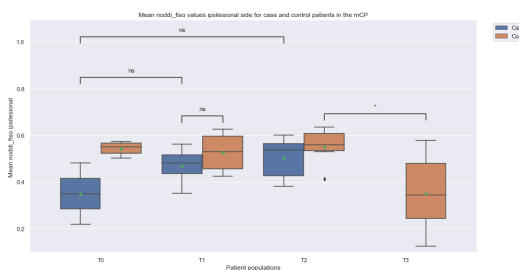


Figure B.11: Free water volume fraction ( $f_{\text{iso}}$ ) boxplots in the Middle Cerebellar Pedunculus (mCP) for both patient populations

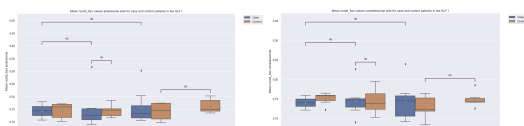


Figure B.12: Free Water Volume Fraction ( $f_{\text{iso}}$ ) boxplots in the Superior Longitudinal Fas-ciculus I (SLF I) on the ipsi- and contralesional sides for both patient populations

# APPENDIX C

## DIAMOND ADDITIONAL RESULTS

This appendix contains the boxplots of the DIAMOND metrics in the Cortico Ponto Cerebellum (CPC), Inferior Cerebellar Pedunculus (iCP), Superior Cerebellar Pedunculus (sCP), Middle Cerebellar Pendunculus (mCP) and Superior Longitudinal Fasciculus I (SLF I).

### C.1 Weighted Fractional Anisotropy

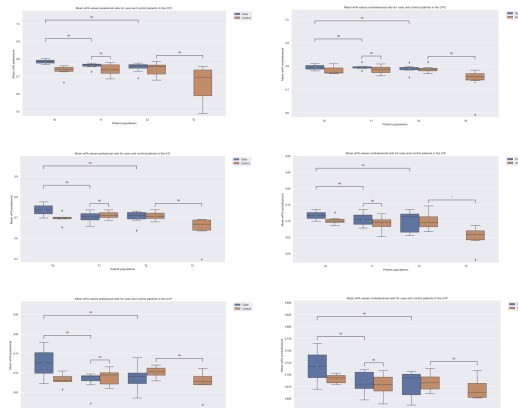


Figure C.1: Weighted Fractional Anisotropy (wFA) boxplots in the Cortico Ponto Cerebellum (CPC), Inferior Cerebellar Pedunculus (iCP) and Superior Cerebellar Pedunculus (sCP) on the ipsi- and contralesional sides for both patient populations

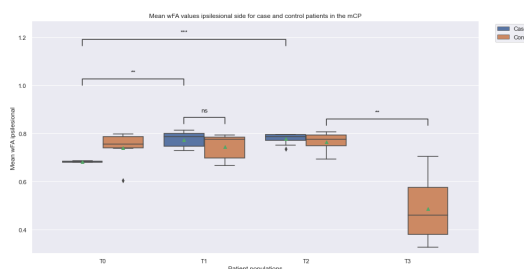


Figure C.2: Weighted Fractional Anisotropy (wFA) boxplots in Middle Cerebellar Pedunculus (mCP) for both patient populations

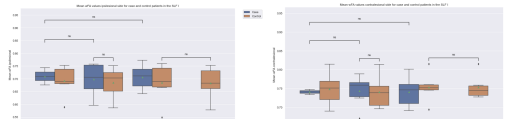


Figure C.3: Weighted Fractional Anisotropy (wFA) boxplots in the Superior Longitudinal Fasciculus I (SLF I) on the ipsi- and contralesional sides for both patient populations

## C.2 Weighted Mean Diffusivity

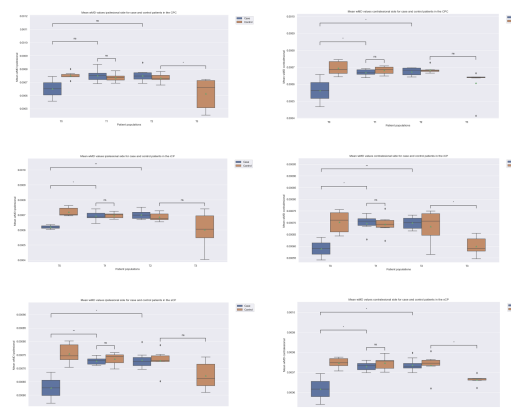


Figure C.4: Weighted Mean Diffusivity (wMD) boxplots in the Cortico Ponto Cerebellum (CPC), Inferior Cerebellar Pedunculus (iCP) and Superior Cerebellar Pedunculus (sCP) on the ipsi- and contralesional sides for both patient populations

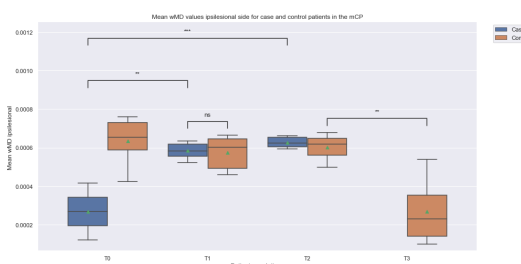


Figure C.5: Weighted Mean Diffusivity (wMD) boxplots in the Middle Cerebellar Pedunculus (mCP) for both patient populations

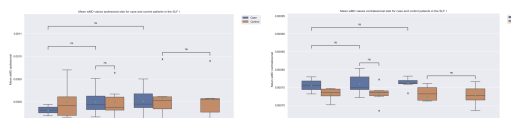


Figure C.6: Weighted Mean Diffusivity (MD) boxplots in the Superior Longitudinal Fasciculus I (SLF I) on the ipsi- and contralesional sides for both patient populations

### C.3 Weighted Axial Diffusivity

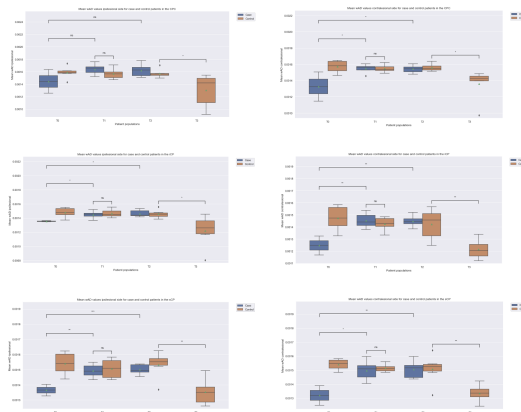


Figure C.7: Weighted Axial Diffusivity (wAD) boxplots in the Cortico Ponto Cerebellum (CPC), Inferior Cerebellar Pedunculus (iCP) and Superior Cerebellar Pedunculus (sCP) on the ipsi- and contralesional sides for both patient populations

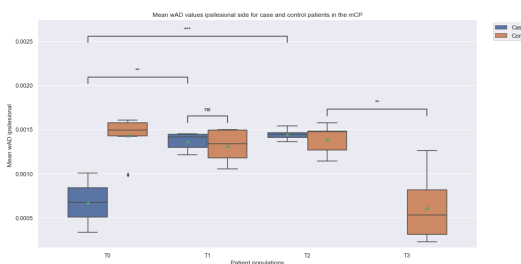


Figure C.8: Weighted Axial Diffusivity (wAD) boxplots in the Middle Cerebellar Pedunculus (mCP) for both patient populations

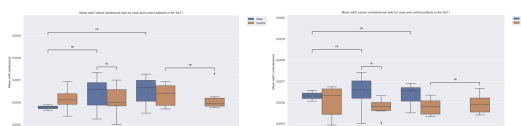


Figure C.9: Weighted Axial Diffusivity (AD) boxplots in the Superior Longitudinal Fasciculus I (SLF I) on the ipsi- and contralesional sides for both patient populations

## C.4 Weighted Radial Diffusivity

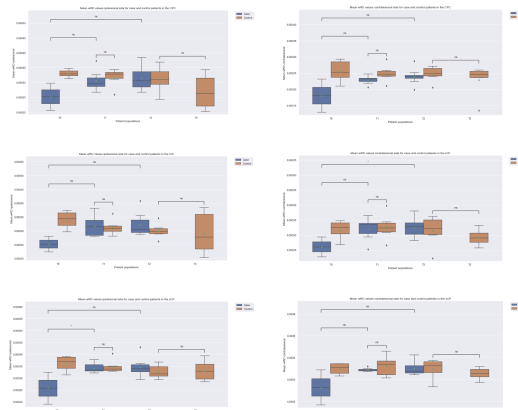


Figure C.10: Weighted Radial Diffusivity (RD) boxplots in the Cortico Ponto Cerebellum (CPC), Inferior Cerebellar Pedunculus (iCP) and Superior Cerebellar Pedunculus (sCP) on the ipsi- and contralesional sides for both patient populations

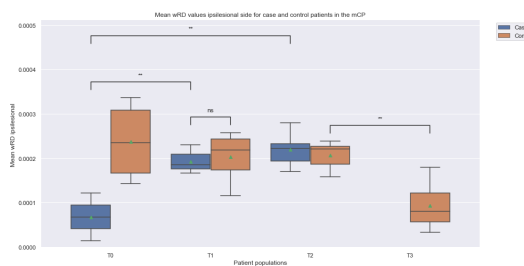


Figure C.11: Weighted Radial Diffusivity (RD) boxplots in the Middle Cerebellar Pedunculus (mCP) for both patient populations

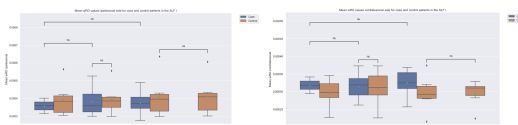


Figure C.12: Weighted Radial Diffusivity (RD) boxplots in the Superior Longitudinal Fasciculus I (SLF I) on the ipsi- and contralesional sides for both patient populations

# APPENDIX D

## MF ADDITIONAL RESULTS

This appendix contains the boxplots of the MF metrics in the Cortico Ponto Cerebellum (CPC), Inferior Cerebellar Pedunculus (iCP), Superior Cerebellar Pedunculus (sCP), Middle Cerebellar Pendunculus (mCP) and Superior Longitudinal Fasciculus I (SLF I).

### D.1 First Population Fraction

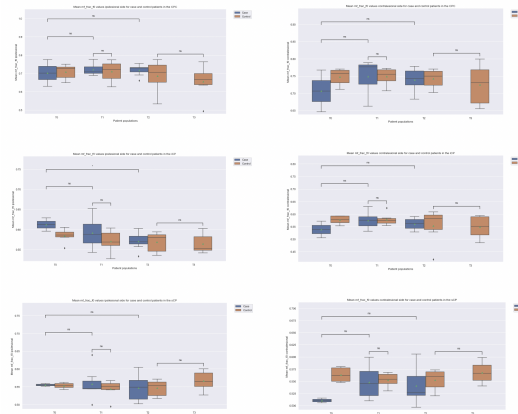


Figure D.1: First population fraction (frac\_f0) boxplots in the Cortico Ponto Cerebellum (CPC), Inferior Cerebellar Pedunculus (iCP) and Superior Cerebellar Pedunculus (sCP) on the ipsi- and contralesional sides for both patient populations

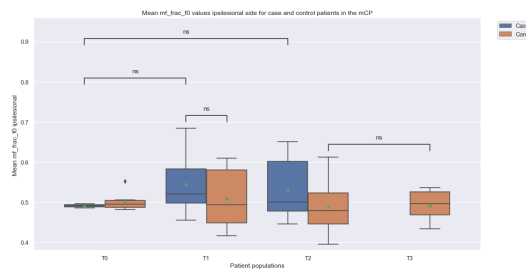


Figure D.2: First population fraction (frac\_f0) boxplots in the Middle Cerebellar Pedunculus (mCP) for both patient populations

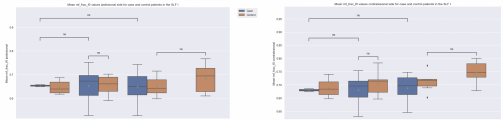


Figure D.3: First population fraction (frac\_f0) boxplots in the Superior Longitudinal Fasciculus I (SLF I) on the ipsi- and contralesional sides for both patient populations

## D.2 Second Population Fraction

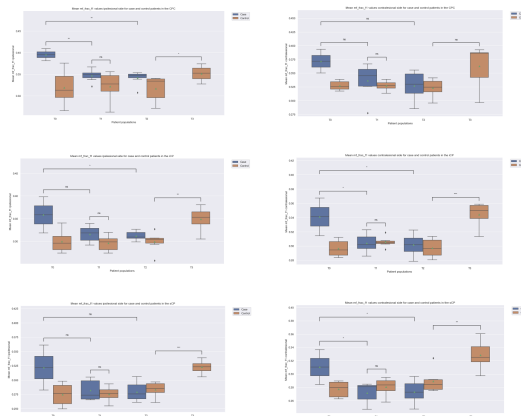


Figure D.4: Second population fraction (frac\_f1) boxplots in the Cortico Ponto Cerebellum (CPC), Inferior Cerebellar Pedunculus (iCP) and Superior Cerebellar Pedunculus (sCP) on the ipsi- and contralesional sides for both patient populations

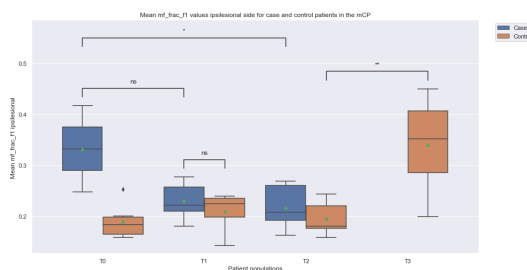


Figure D.5: Second population fraction (frac\_f1) boxplots in Middle Cerebellar Pedunculus (mCP) for both patient populations

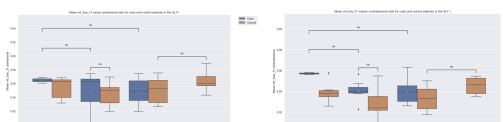


Figure D.6: Second population fraction (frac\_f1) boxplots in the Superior Longitudinal Fasciculus I (SLF I) on the ipsi- and contralesional sides for both patient populations

### D.3 Free Water Fraction

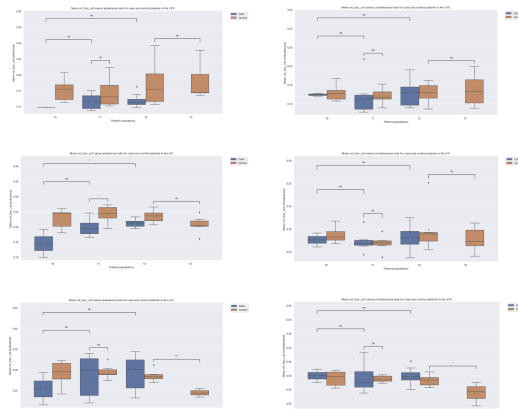


Figure D.7: Free water fraction (frac\_csf) boxplots in the Cortico Ponto Cerebellum (CPC), Inferior Cerebellar Pedunculus (iCP) and Superior Cerebellar Pedunculus (sCP) on the ipsi- and contralesional sides for both patient populations

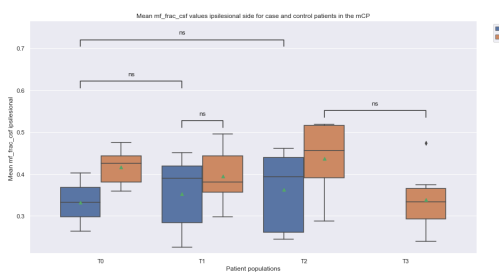


Figure D.8: Free water fraction (frac\_csf) boxplots in the Middle Cerebellar Pedunculus (mCP) for both patient populations

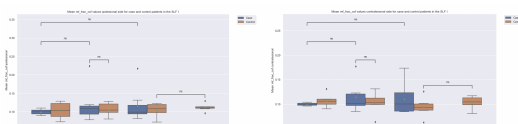


Figure D.9: Free water fraction (frac\_csf) boxplots in the Superior Longitudinal Fasciculus I (SLF I) on the ipsi- and contralesional sides for both patient populations

## D.4 Total Fiber Volume Fraction

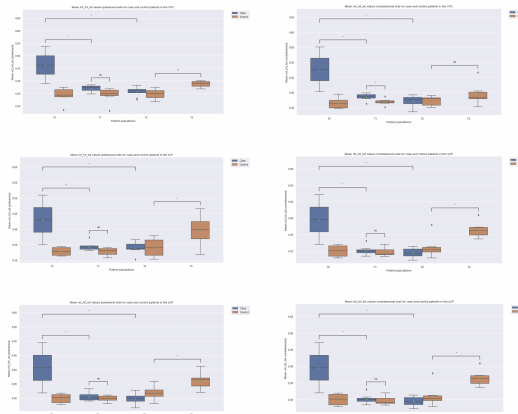


Figure D.10: Total fiber volume fraction (fvf\_tot) boxplots in the Cortico Ponto Cerebellum (CPC), Inferior Cerebellar Pedunculus (iCP) and Superior Cerebellar Pedunculus (sCP) on the ipsi- and contralesional sides for both patient populations

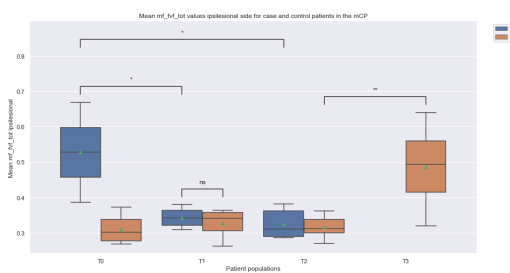


Figure D.11: Total fiber volume fraction (fvf\_tot) boxplots in the Middle Cerebellar Pedunculus (mCP) for both patient populations

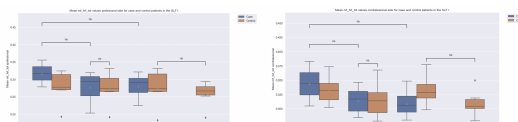


Figure D.12: Total fiber volume fraction (fvf\_tot) boxplots in the Superior Longitudinal Fasciculus I (SLF I) on the ipsi- and contralesional sides for both patient populations

## D.5 Weighted Total Fiber Volume Fraction

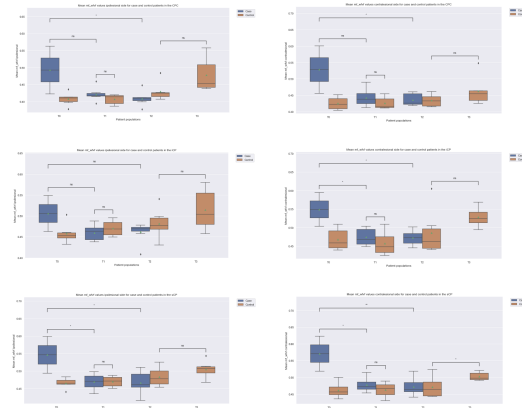


Figure D.13: Weighted total fiber volume fraction (wfvf) boxplots in the Cortico Ponto Cerebellum (CPC), Inferior Cerebellar Pedunculus (iCP) and Superior Cerebellar Pedunculus (sCP) on the ipsi- and contralesional sides for both patient populations

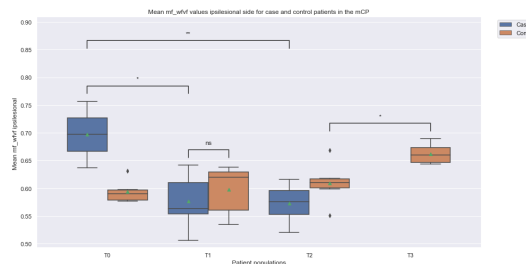


Figure D.14: Weighted total fiber volume fraction (wfvf) boxplots in the Middle Cerebellar Pedunculus (mCP) for both patient populations

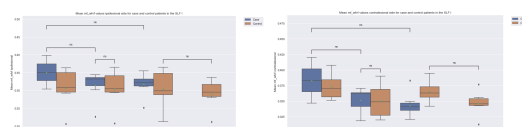


Figure D.15: Weighted total fiber volume fraction (wfvf) boxplots in the Superior Longitudinal Fasciculus I (SLF I) on the ipsi- and contralesional sides for both patient populations

## APPENDIX E

### CORPUS CALLOSUM REGISTRATION

As for the other atlas sets described in Section 3.3, registration of the Corpus Callosum (CC) was attempted using a reference atlas map from the Neuroanatomy and Tractography Laboratory (NatbrainLab) [134]. However, this CC atlas map is set in its own native space in contrast to the other atlas maps which were all set in the MNI space. As the CC atlas set contained a standardized reference brain, registration based on the use of this reference brain towards patients' native space was attempted. As visible on Figure E.1, the resulting location of the registered CC does not accurately correspond to the biological location of patients' CC. The CC atlas maps were thus not further used for the definition of a ROI corresponding to the CC.

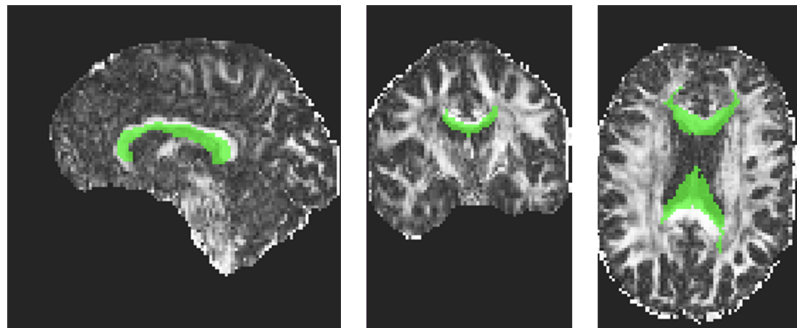


Figure E.1: Inaccurate registration of the corpus callosum illustrated for patient 20.03.03 at time T1

## APPENDIX F

### TRACT-BASED ROI

This appendix describes the key steps necessary to the identification of tract-based ROI through a concrete example. Fiber tractography is a technique allowing the identification of the trajectories of white matter tracts. Using probabilistic algorithms such as the Constrained Spherical Deconvolution (CSD) algorithm, the observed diffusion data in every voxel of MR images can be used to determine WM streamlines in the whole brain. The measured WM pathways constitute whole-brain tractograms which can be computed using the tracking DiPy Python package. Figure F.1 shows the whole-brain tractogram of patient *20.03.03* at time T1, generated with the CSD model.

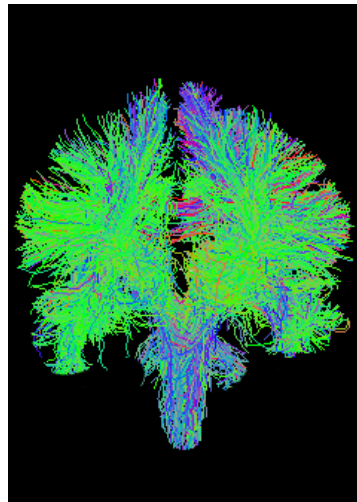


Figure F.1: Whole-brain tractogram of patient *20.03.03* at time T1

The results of whole-brain tractography can be improved for each patient through the fine tuning of the CSD model parameters (FA threshold, step size, fiber density, etc.). Moreover, tract-based regions of interest can now be defined through the combination of seed regions, target regions and exclusion masks. Figure F.2 illustrates this procedure, used to define a region of interest corresponding to the right and left corticospinal tracts.

The definition of a tract-based ROI corresponding to the CST was attempted for patient *20.03.03* at time T1. Figure F.3 shows the hand-drawn seed and target regions and Figure F.4 displays the obtained CST ROI on one side of the brain.

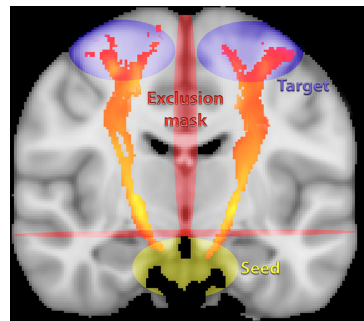


Figure F.2: Definition of the seed regions, target regions and exclusion masks for CST tractography, adapted from [1]

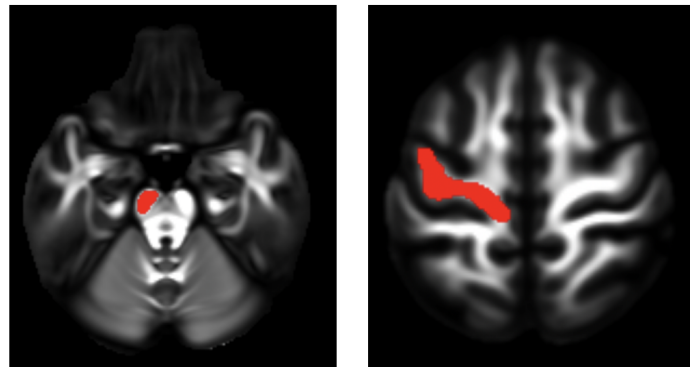


Figure F.3: Illustration of the seed region in the CST and of the target region in the motor cortex

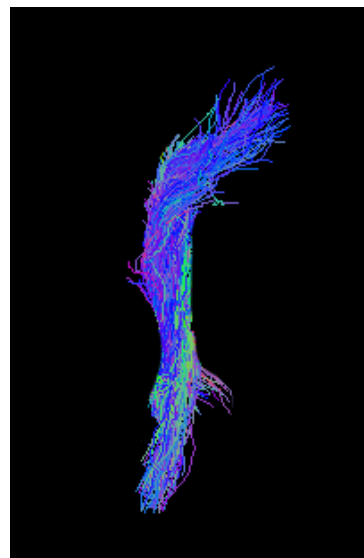


Figure F.4: Resulting CST ROI for patient 20.03.03 at time T1

## APPENDIX G

### CONNECTIVITY ANALYSIS

As explained in Section 5.7, the FreeSurfer software can be used to perform the pre-processing of the raw data. More precisely, this software provides the `recon-all` command which successively performs data preprocessing (skull stripping, B1 bias field correction, grey-white matter segmentation), reconstruction of cortical surface models and the labeling of regions on the cortical surface (parcellation), as well as subcortical brain structures (segmentation) [49]. The outputs of this command regroup labeled maps of cortical and subcortical anatomically distinct regions such as illustrated on Figure G.1 which can then be used to perform further analysis. Although the resulting maps obtained by using FreeSurfer seem accurate, the use of `recon-all` is very time consuming as the processing of a single patient can take from several hours up to a day.

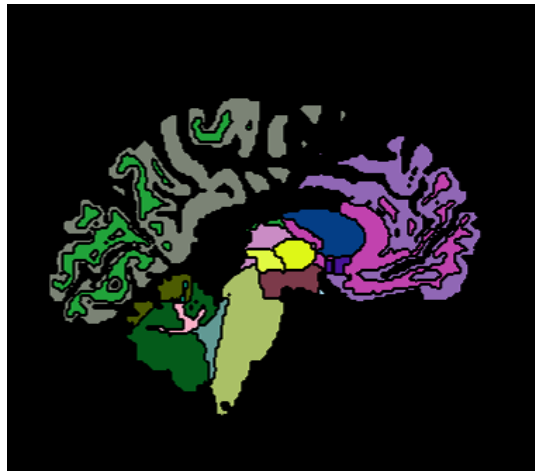


Figure G.1: Segmentation and parcellation obtained using the FreeSurfer software on patient 20.03.03 at time T1

Once labeled maps of the brain regions are obtained, it becomes possible to perform connectivity analysis based on the use of whole-brain connectomes. Connectivity analysis have the potential to identify and characterize the plasticity of neural networks during the recovery process after stroke. Concretely, using a patient's labeled brain map obtained via FreeSurfer and whole-brain tractogram generated by the probabilistic Constrained Spherical Deconvolution (CSD) model (discussed in Section 1.2.3 and illustrated with a concrete example in Appendix F on Figure F.1) the WM pathways connectivity can be analyzed. Using the tracking DiPy Python package, connectivity matrices for a specific brain region, and showing the degree of connectivity of this

regions to other brain regions, can be obtained. The evolution of the representation of these connectivity matrices enables the longitudinal study of the brain connectivity and thus of the brain plasticity after stroke.

Furthermore, the White Matter Query Language (WMQL) [130] can be used to automatically extract a set of white matter tract bundles and analyze their connectivity using a whole-brain tractogram and a labeled map of the brain regions. The WMQL can thus be used to analyze the structural variation of specific WM tracts and to characterize their connectivity to brain regions.

**UNIVERSITÉ CATHOLIQUE DE LOUVAIN**  
**École polytechnique de Louvain**

Rue Archimède, 1 bte L6.11.01, 1348 Louvain-la-Neuve, Belgique | [www.uclouvain.be/epl](http://www.uclouvain.be/epl)